

AD_____

Award Number: DAMD17-03-1-0405

TITLE: Three Dimensional Reconstruction Algorithm for Imaging Pathophysiological Signals within Breast Tissue using Near Infrared Light

PRINCIPAL INVESTIGATOR: Hamid Dehghani, Ph.D.

CONTRACTING ORGANIZATION: Dartmouth College
Hanover, NH 03755

REPORT DATE: July 2005

TYPE OF REPORT: Annual Summary

PREPARED FOR: U.S. Army Medical Research and Materiel Command
Fort Detrick, Maryland 21702-5012

DISTRIBUTION STATEMENT: Approved for Public Release;
Distribution Unlimited

The views, opinions and/or findings contained in this report are those of the author(s) and should not be construed as an official Department of the Army position, policy or decision unless so designated by other documentation.

| REPORT DOCUMENTATION PAGE | | | | Form Approved OMB No. 0704-0188 | |
|--|------------------|----------------------------------|--------------------------------------|---|--|
| Public reporting burden for this collection of information is estimated to average 1 hour per response, including the time for reviewing instructions, searching existing data sources, gathering and maintaining the data needed, and completing and reviewing this collection of information. Send comments regarding this burden estimate or any other aspect of this collection of information, including suggestions for reducing this burden to Department of Defense, Washington Headquarters Services, Directorate for Information Operations and Reports (0704-0188), 1215 Jefferson Davis Highway, Suite 1204, Arlington, VA 22202-4302. Respondents should be aware that notwithstanding any other provision of law, no person shall be subject to any penalty for failing to comply with a collection of information if it does not display a currently valid OMB control number. PLEASE DO NOT RETURN YOUR FORM TO THE ABOVE ADDRESS. | | | | | |
| 1. REPORT DATE (DD-MM-YYYY) 01-07-2005 | | 2. REPORT TYPE Annual Summary | | 3. DATES COVERED (From - To) 30 DEC 2004 - 29 DEC 2005 | |
| 4. TITLE AND SUBTITLE Three Dimensional Reconstruction Algorithm for Imaging Pathophysiological Signals within Breast Tissue using Near Infrared Light | | | | 5a. CONTRACT NUMBER | |
| | | | | 5b. GRANT NUMBER DAMD17-03-1-0405 | |
| | | | | 5c. PROGRAM ELEMENT NUMBER | |
| 6. AUTHOR(S) Hamid Dehghani, Ph.D. E-mail: hamid.dehghani@dartmouth.edu | | | | 5d. PROJECT NUMBER | |
| | | | | 5e. TASK NUMBER | |
| | | | | 5f. WORK UNIT NUMBER | |
| 7. PERFORMING ORGANIZATION NAME(S) AND ADDRESS(ES) Dartmouth College Hanover, NH 03755 | | | | 8. PERFORMING ORGANIZATION REPORT NUMBER | |
| 9. SPONSORING / MONITORING AGENCY NAME(S) AND ADDRESS(ES) U.S. Army Medical Research and Materiel Command Fort Detrick, Maryland 21702-5012 | | | | 10. SPONSOR/MONITOR'S ACRONYM(S) | |
| | | | | 11. SPONSOR/MONITOR'S REPORT NUMBER(S) | |
| 12. DISTRIBUTION / AVAILABILITY STATEMENT Approved for Public Release; Distribution Unlimited | | | | | |
| 13. SUPPLEMENTARY NOTES | | | | | |
| 14. ABSTRACT Optical tomography is a non-invasive imaging technique that can image properties of biological tissue using Near Infrared light. Under this program, this technique has been used to characterize breast tissue in healthy volunteers as well as detecting tumor in patients. Image reconstruction models and algorithms have been developed, under this program, which incorporates inherent wavelength dependant a-priori information (spectral) as well as concurrently measured MRI structural information (spatial) to show that the quantitative and qualitative accuracy can be dramatically improved. Three dimensional models have been developed that will allow the use of correct size and shape of the breast being imaged showing that image artifacts can be eliminated by the correct assumptions about the model of the breast. Novel models have also been developed that will account for otherwise ignored Refractive Index (RI) distribution of breast tissue, and the results indicate that providing the RI distribution of breast tissue is not extremely heterogeneous, the impact on reconstructed artifacts is minimal. | | | | | |
| 15. SUBJECT TERMS OPTICAL TOMOGRAPHY; NEAR INFRARED IMAGING; BREAST CANCER CHARACTERIZATION | | | | | |
| 16. SECURITY CLASSIFICATION OF: | | | 17. LIMITATION OF ABSTRACT UU | 18. NUMBER OF PAGES 54 | 19a. NAME OF RESPONSIBLE PERSON USAMRMC |
| a. REPORT U | b. ABSTRACT U | c. THIS PAGE U | | | 19b. TELEPHONE NUMBER (include area code) |

Table of Contents

| | |
|-----------------------------------|---|
| Cover..... | 1 |
| SF 298..... | 2 |
| Introduction..... | 4 |
| Body..... | 4 |
| Key Research Accomplishments..... | 7 |
| Reportable Outcomes..... | 7 |
| Conclusions..... | 7 |
| References..... | 7 |
| Appendices..... | 9 |

Introduction

In this work, a novel imaging technique is explored that uses non-harmful application of near infrared light to determine the pathophysiological properties of breast tissue. Using this technique, known as near infrared (NIR) tomography, an optical fiber placed on the surface of the region of interest, the breast, delivers an input signal while other optical fibers placed at different locations on the same surface detect the out-coming photons, which have propagated through the volume under investigation. The intensity and path-length distributions of the exiting light provide information about the optical properties of the transilluminated tissue using a model-based interpretation where photon propagation is simulated by the diffusion theory. Through iterative solution to match the theory to the real measurements, images of internal absorption and scattering coefficient distribution can be reconstructed. Tissue optical properties have shown to be a function of their structure and more importantly, their physiological state. It is these qualities that provide an alternative method for the detection and characterization of tumor within breast tissue. An important aspect for the success and accuracy of this method is the use of adequate modeling of light within breast tissue. In this work, we have used a Finite Element Model of the Diffusion Approximation, to calculate and predict light transport. Using such technique, we are able to determine, to some accuracy, the distribution of internal optical properties of the tissue under investigation. A major limitation in the development of near infrared imaging so far has been the lack of accurate and fast model-based reconstruction algorithm for this modality, which is a direct aim of the project being funded.

Since the award of this project, the aims have not changed. In brief these are:

- (1) Validate, improve and accelerate a three-dimensional finite element model of light propagation within the breast tissue as well as the image reconstruction algorithm for simultaneously calculating the internal absorption and scattering coefficients.
- (2) Investigate the benefits and limits of using a-priori information from dual modality images, for example, MRI and Near Infrared data.
- (3) Explore the benefits and limits of using Fluorescent contrast-agents, which will target specific molecular markers of the tumor, giving rise to a-priori information regarding tumor location as well as physiological function of the tissue.
- (4) Test the developed algorithm on patient data and compare results with available mammograms and biopsy results to evaluate algorithm accuracy

During the second year of the funding period, several advances and improvements to the modeling and image reconstruction algorithms have been implemented. The three dimensional image reconstruction algorithms have been further modified to improve computational speed and overhead allowing a more realistic time frame for image reconstruction. Additional improvements in the modeling capabilities have been incorporated, namely in terms of allowing for internal tissue Refractive Index (RI) distribution as well as tissue deformation, both of which are discussed below. The use of a-priori information within the image reconstruction algorithm have been investigated, namely through the use of structural (MRI) information and spectral (Wavelength dependant) information. Finally some image analysis has been used to date, utilizing the developed code to seek the pathophysiological properties of breast tissue and cancer. Each of the area of research developed during this second of funding will be addressed below together with the main findings and their implications of optical tomography of breast tissue in-vivo, specifically for the detection and characterization of breast cancer.

Body

Effect of Refractive Index variation

Previous studies [1] reported results in modeling the effect of Refractive Index (RI) on the forward model. In the results obtained during this funding period, the initiative was advanced to investigating the effect of RI variation on NIR image reconstruction, by assuming either correct knowledge of the RI of each tissue or applying a homogenous value throughout the model. The study showed that providing the RI of the glandular tissue is not far from the value of adipose tissue, it has little effect on the qualitative and quantitative accuracy of the results, as demonstrated in Figure 1. Assuming the RI of the whole breast is similar, for example, the RI is 1.455 for adipose and 1.4 for glandular tissue, reconstructed images of absorption and scatter can be obtained which ignore the effect of RI with modest degradation in the recovery of information about an abnormality. However, it is also important to note that this analysis was completed under the assumption that the abnormality (i.e. tumor) has the same RI as its background tissue and is most typically located in the fibroglandular tissue. Further studies are required to establish the RI variation for different types of tumors and to investigate how such variations might alter NIR tomography. The absolute values of RI for breast tissue types are still a subject under investigation. Estimates are difficult to obtain accurately in-vivo, but some data has been reported for various tissue types [2, 3]. Although adipose tissue (fatty layer) has been measured to be 1.455, no results exist for fibro-glandular tissue. Nonetheless the RI of glandular tissue is believed to be lower than that of adipose (e.g. values of 1.4 have been assumed in [2, 4]). The rationale for a lower value is sound in that estimates of the composition of fibroglandular tissue place its water (typically over 60%) and

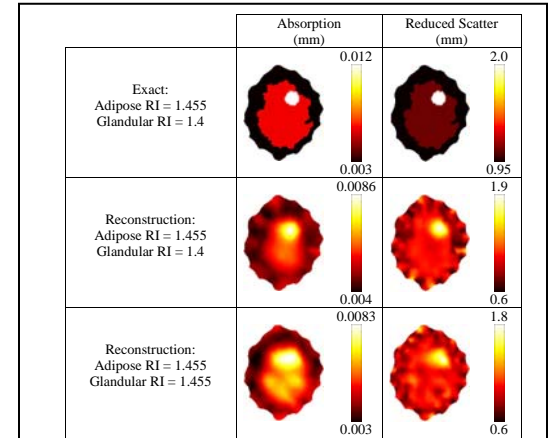


Figure 1. Images reconstructed using a model with refractive index variation. Top row shows the exact optical properties where adipose and glandular tissue have different optical properties and different refractive index (RI) of 1.455 and 1.4, respectively. Middle row shows reconstructed images assuming the correct RI distribution. Bottom row shows reconstructed images assuming a homogenous RI of 1.455.

blood content (over 1%) to be high, indicating that its bulk refractive index is likely close to that of water [5, 6].

Breast deformation modeling

In order to obtain good NIR data measurements it is essential to have good contact between the optical fibers and the breast which in-turn results in the deformation of the breast, Figure 2, due to the soft plasticity of the tissue. A tissue deformation model of the female breast has been developed that will account for the altered shape of the breast during clinical NIR measurements, Figure 3. Using a deformed model of a breast, NIR data was used to reconstruct images of tissue absorption and reduced scatter using assumptions about the imaging domain, Figure 4 [7].

Assuming a non-deformed breast shape for image reconstruction has shown to lead to poor quality images since the geometry of the breast is greatly altered, whereas using the correct deformed geometry produces the best images. The goal of this work was to incorporate this new model of breast deformation with more accurate information regarding the mechanical properties of the breast to improve the NIR image reconstruction. The mechanical property information is readily available from other imaging modalities, and the synthesis of this information may provide fundamentally new information about breast physiologic response to pressure, and/or breast pathology response to pressure. An accurate model of breast deformation should in principle allow us to create patient specific models and meshes, which would in-turn provide more clinically useful data.

Spectral and spatial a-priori information

The use of spatial a priori information was investigated during the first year of funding under this program. Namely, realistic breast phantoms were used to investigate the use of spatial information to constrain and penalize the reconstruction algorithm and have been shown to improve both the qualitative and quantitative accuracy of the reconstructed images [8-10].

The concept underpinning parametric or spectrally constrained imaging is the generation of a derived response from multi-spectral data. Typically, images are formed serially, wavelength-by-wavelength, and do not impose connectivity between the image estimate at one wavelength with that of at another. By using a spectral model composed of certain wavelength-independent parameters, as in Figure 5, it becomes possible to combine multi-spectral data in a new way. Concepts of multi-spectral and spatially constrained image reconstruction have recently been extended to NIR which has reached the point of application to experimental and clinical data and is highlighted here as an illustration in Figure 6 (row 3). Specifically, multiple wavelengths NIR data have been used simultaneously to reconstruct absolute values of chromophore concentration (deoxy and oxygenated blood concentration and water) as well as scattering properties (scattering power (b) and amplitude (A)). Thus, instead of estimating the absorption and reduced scatter properties at each wavelength, independently and then using these values to derive specific chromophore concentrations and scattering parameters, the aim is to encode directly the linear map between wavelength-dependent optical properties and chromophore concentrations through their known spectral signatures. This leads to a single reconstruction to estimate all of the final images

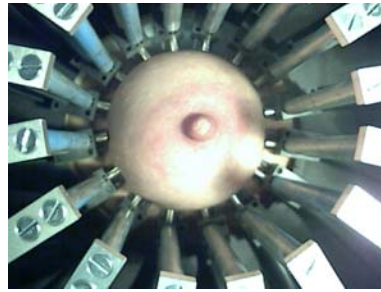


Figure 2. Photo of the breast being compressed by the optical fibers to ensure good contact for data collection.

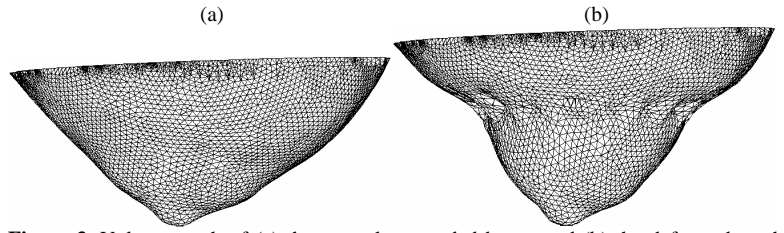


Figure 3. Volume mesh of (a) the normal suspended breast and (b) the deformed mesh after the application of the optical fiber array.

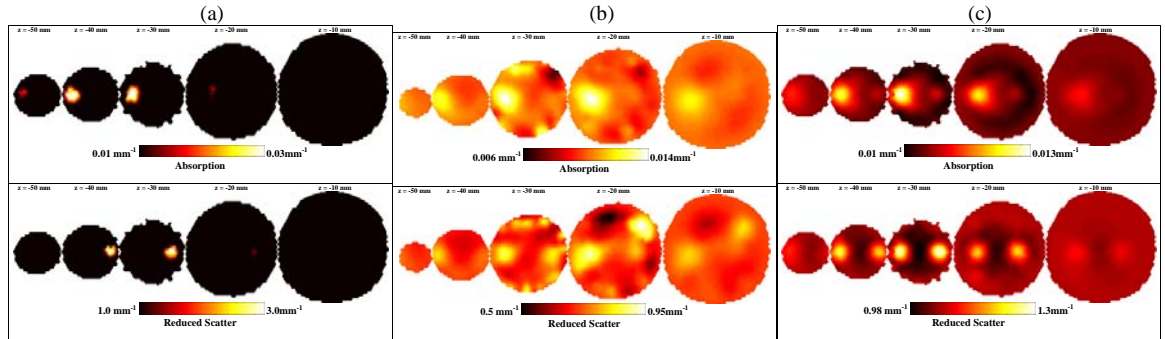


Figure 4. (a) 2D coronal slices through the deformed breast mesh, showing the position of the anomalies. The most right hand slice is near the chest while the most left hand slice is near the nipple. (b) Reconstructed images assuming no deformation, and (c) reconstructed images using a deformed mesh using information about fiber contact.

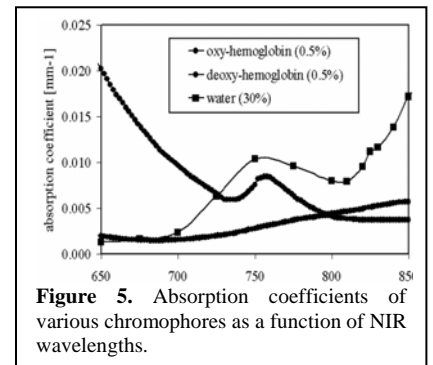
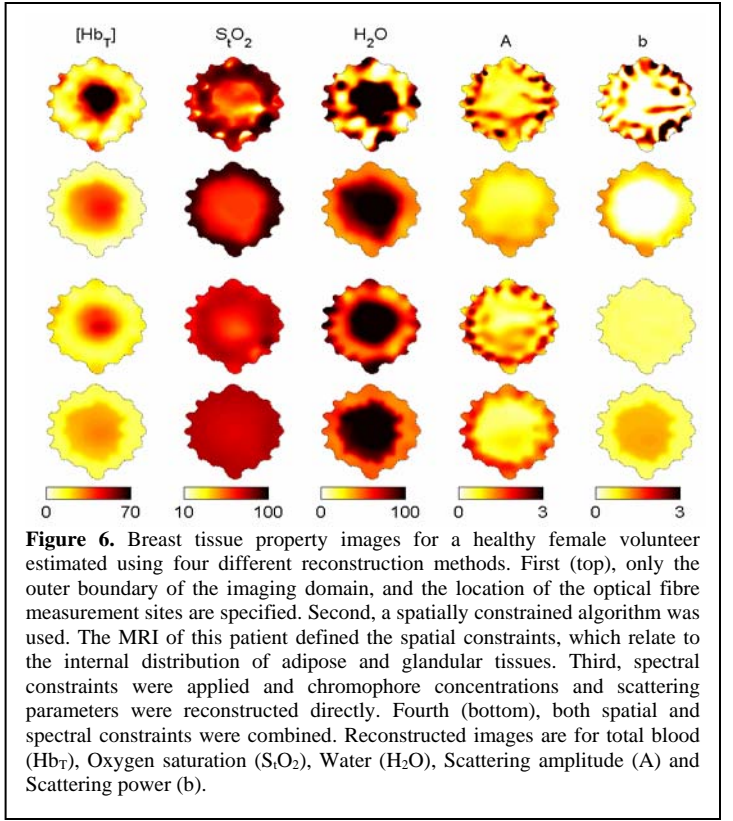


Figure 5. Absorption coefficients of various chromophores as a function of NIR wavelengths.

simultaneously and has shown to offer the advantage of reducing image sensitivity to noise at specific (individual) wavelengths, especially in the water and oxygen saturation distributions [11, 12].

A combined NIR-MRI imaging system has been used [9, 10] in a case study to estimate the properties of healthy breast tissue, Figure 6. The images obtained for the NIR parameters using an unconstrained reconstruction shows noisy images with boundary artifacts. The spatial priors act on these images, making them smoother, but preserving the trend for the quantification. For example, the scatter power shows a reduction in the glandular tissue (row 2) similar to the values obtained in the no-priors reconstruction (row 1). However, previous studies have indicated that, glandular tissue having higher number density of scatterers, may actually have higher values for scatter power, than fatty tissue. Hence, the results from spatially constrained reconstruction, while appearing smoother, may be misleading. The scatter power image obtained by application of the spectrally constrained method is more quantitatively acceptable and the spatial priors acting on this spectral method gives the most intuitively acceptable image for this parameter, showing the layered structure of the breast tissue. We observed elevated $[Hb_T]$ (25:13 μM), water (91:49 %), and scattering power (1.0:0.5) in glandular tissue relative to adipose tissue using the combined priors, which matches the higher vascularization in the glandular tissue.

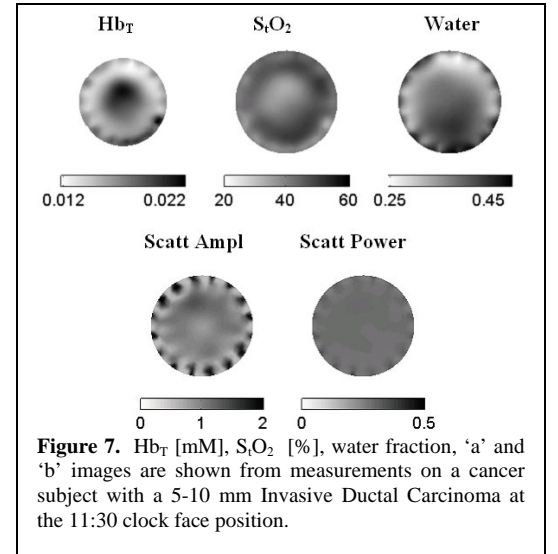
The results so far show that, while anatomical information improves the image quality resulting in reduced artifacts, it may not significantly improve quantification. The spectral prior obtained using the intrinsic behavior of tissue chromophores and scattering in the near infrared wavelength regime plays a more important role in addressing this problem, and finally, a synergy between these two priors yields the most accurate characterization of breast tissue properties currently possible.



Tissue characterization using Spectral Imaging

As an illustration, the direct spectral reconstruction method has also been applied to clinical tomography data obtained from measurements on a 66 year old subject with a 5-10 mm spiculated mass evident on mammography, which was later diagnosed as Invasive Ductal Carcinoma [12]. The subject underwent the NIR exam in accordance with the Dartmouth protocol, where informed consent was obtained prior to the exam. The position of the anomaly was provided through mammography and determined to be at 11:30 o'clock in the cranocaudal view and located about 1cm from surface. Reconstructed images are shown in Figure 7. A localized increase in $[Hb_T]$ was observed and the contrast available was 1.7:1.0 in tumor versus background. The $[S_tO_2]$ image showed a decrease at the location of the tumor with a contrast of 0.7:1. The corresponding S_tO_2 image with the conventional technique was noisier (spatially) and a similar decrease was not observed. The water fraction image showed heterogeneity in the range 0.25 to 0.5%, which is considerably smaller than the range of 0 to 1% observed with the old method. Tighter data ranges are similarly observed in the scatter images, and artifacts evident in the separate wavelength technique have been suppressed in the spectral approach.

With this new technique, higher hemoglobin content at the site of tumor is observed in the clinical case, as well as lower oxygen saturation. The water fraction and scattering images show the most significant improvement in all cases by reduction of the image artifacts. Further data analysis over a larger patient data is needed and is a subject of active research in the final year of the funded project.



Key research accomplishments

1. Assuming that the effect of the refractive index (RI) variation in breast tissue is small, such that if ignored, the errors obtained within reconstructed images are minimal. This in reality is acceptable, given that the variation in RI of tissue within the breast is small, ranging from 1.4 to 1.455.
2. The effect of breast deformation tissue to optical fiber contact has been investigated. It is shown that if the deformation is large, adequate priori knowledge about the shape of the breast is essential for useful clinical images. Such information can either be obtained using mechanical models (as demonstrated) or using a-priori structural images from for example MRI.
3. Spectral and spatial priori constraints have been developed and implemented to show improved accuracy in clinical information about reconstructed images. It is shown that incorporation of both such information significantly improves both qualitative and quantitative accuracy of images.
4. To date, spectral constraints have been used to analyze clinical data. It has been demonstrated that addition of such constraints can significantly improve the clinical accuracy of physiological data obtained from clinical cases.

Reportable outcomes

The first 2 years of the funding of this project has led to a number of peer reviews publications as well as oral presentation at international conferences. Links and collaborations have been established with Washington University at St. Louis who are now routinely using the developed code. Further collaboration has been established with University of Pennsylvania through the development of alternative image reconstruction algorithms allowing the use of large datasets. Reportable outcomes include:

1. Oral presentation at the Optical Society of America (OSA) international meeting in 2004
2. Oral presentation at the International Society for Optical Engineering international meeting in 2005
3. Applied for funding from NCI through R01 mechanism (PI Hamid Dehghani, "Breast Deformation Modeling for Near Infrared Tomography" 3 year project)
4. Applied for funding from DoD through the IDEA award mechanism (PI Hamid Dehghani, "Neoadjuvant Therapy Treatment monitoring using CT Guided Optical Tomography" 3 year project)

Conclusions

The project is continuing to reconstruct NIR images of clinical data to build the database of 3D images. Steps have also been taken as part of this project to achieve other aims specified by this project. A new and novel image reconstruction algorithm has been developed and implemented which allows the direct reconstruction of chromophore concentration and scattering functions of breast tissue. This not only allows a computationally efficient implementations, but also since all the data from all wavelength are used coupled together, a great reduction in image noise and artifact is seen. Finally, as a direct result of the 2nd aim, the project is beginning to develop, understand and implement a useful algorithm for the incorporation of a-priori information, not only in phantom studies, but also in clinical setups.

References

1. Dehghani, H., Brooksby, B., Vishwanath, K., Pogue, B. W., Paulsen K. D., *The effects of internal refractive index variation in near infrared optical tomography: A finite element modeling approach*. Phys. Med. Biol., 2003. **48**: p. 2713-2727.
2. Bolin, F.P., Preuss, L. E., Taylor, R. C., Ference, R. J., *Refractive index of some mammalian tissue using a fiber optic cladding method*. Applied Optics, 1989. **28**(12): p. 2297-2303.
3. Brooksby, B., Dehghani, H., Vishwanath, K., Pogue, B. W., Paulsen, K. D., *Internal refractive index changes affect light transport in tissue*. proceedings of spie, 2003. **4955**: p. 296-304.
4. Tromberg, B.J., Coquoz, O., Fishkin, J. B., Pham, T., Anderson, E. R., Butler, J., Cahn, M., Gross, J. D., Venugopalan, V., Pham, D., *Non-invasive measurements of breast tissue optical properties using frequency-domain photon migration*. Phil. Trans. R. Soc. Lond. B, 1997. **352**: p. 661-668.
5. Srinivasan, S., Pogue, B. W., Jiang, S., Dehghani, H., Kogel, C., Soho, S., Gibson, J. J., Tosteson, T. D., Poplack, S. P., Paulsen, K. D., *Interpreting Hemoglobin and Water Concentration, Oxygen Saturation and Scattering Measured In Vivo by Near-Infrared Breast Tomography*. PNAS, 2003. **100**(21): p. 12349-12354.
6. Pogue, B.W., Jiang, S., Dehghani, H., Kogel, C., Soho, S., Srinivasan, S., Song, X., Poplack, S. P., Paulsen, K. D., *Characterization of Hemoglobin, Water and NIR Scattering in Breast Tissue: Analysis of inter-subject variability and menstrual cycle changes relative to lesions*. JBO, 2004. **9**(3): p. 541-552.
7. Dehghani, H., Doyley, M. M., Pogue, B. W., Jiang, S., Geng, J., and Paulsen, K. D., *Breast deformation modeling for image reconstruction in near infrared optical tomography*. phys. med. biol., 2004. **49**(7): p. 1131-1146.
8. Xu, H., Springett, R., Dehghani, H., Pogue, B.W., Paulsen, K.D., and Dunn, J.F., *MRI coupled Broadband Near Infrared Tomography System for Small Animal Brain Studies*. Appl. Opt., 2005. **44**(11): p. 2177-2188.
9. Brooksby, B., Jiang, S., Dehghani, H., Pogue, B. W., Paulsen, K. D., Weaver, J., Kogel, C., and Poplack, S. P., *Combining near infrared tomography and magnetic resonance imaging to study in vivo breast tissue: implementation of a Laplacian-type regularization to incorporate magnetic resonance structure*. JBO, 2005. **10**(5).

10. Brooksby, B., Jiang, S., Kogel, C., Doyley, M., Dehghani, H., Weaver, J. B., Poplack, S. P., Pogue, B. W., Paulsen, K. D., *Magnetic Resonance-Guided Near-Infrared Tomography of the Breast*. Rev. Sci. Instrum., 2004. **75**(12).
11. Brooksby, B., Srinivasan, S., Jiang, S., Dehghani, H., Pogue, B.W., Paulsen, K.D., Weaver, J., Kogel, C., and Poplack, S.P., *Spectral-prior information improves Near-Infrared diffuse tomography more than spatial-prior*. Optics letters, 2005. **30**(15): p. 1968-1970.
12. Srinivasan, S., Pogue, B. W., Jiang, S., Dehghani, H., and Paulsen, K. D., *Spectrally Constrained Chromophore and Scattering NIR Tomography Provides Quantitative and Robust Reconstruction*. Appl. Opt., 2005. **44**(10): p. 1858-1869.

Publications List

S. Srinivasan, B. W. Pogue, S. Jiang, **H. Dehghani**, C. Kogel, S. Soho, J. J. Gibson, T. D. Tosteson, S. P. Poplack, K. D. Paulsen, "Interpreting Hemoglobin and Water Concentration, Oxygen Saturation and Scattering Measured In Vivo by Near-Infrared Breast Tomography" PNAS vol 100 no 21 pp 12349-12354 2003

X. Song, B. W. Pogue, s. Jiang, M. M. Doyley, **H. Dehghani**, T. D. Tosteson, K. D. Paulsen, "Automated Region Detection Based Upon Contrast To Noise Ratio in Near-Infrared Tomography," Applied Optics 43(5) 1053-1062, 2004

H. Dehghani, M. M. Doyley, B. W. Pogue, S. Jiang, J. Geng and K. D. Paulsen, "Breast deformation modeling for image reconstruction in near infrared optical tomography" Phys. Med. Biol. Volume 49, Number 7, pp 1131-1146 2004.

S. Srinivasan, B. W. Pogue, **H. Dehghani**, S. Jiang, X. Song and K. D. Paulsen, "Improved Quantification of Small Objects in Near-Infrared Diffuse Optical Tomography" JBO 9(6) 1161-1171 2004

B. W. Pogue, S. Jiang, **H. Dehghani**, C. Kogel, S. Soho, S. Srinivasan, X. Song, S. P. Poplack, and K. D. Paulsen, "Characterization of Hemoglobin, Water and NIR Scattering in Breast Tissue: Analysis of inter-subject variability and menstrual cycle changes relative to lesions" JBO, 9(3) 541-552, 2004.

Ben Brooksby, Shudong Jiang, Christine Kogel, Marvin Doyley, **Hamid Dehghani**, John B Weaver, Steven P Poplack, Brian W Pogue and Keith D Paulsen, "Magnetic Resonance Guided Near Infrared Tomography of the Breast", Rev. Sci. Inst. 75 5262-5270 2004

Heng Xu, Brian W. Pogue, **Hamid Dehghani**, Keith D. Paulsen, Roger Springett and Jeff F. Dunn, "Absorption and scattering imaging of tissue with steady-state second-differential spectral-analysis tomography" Optics letters 29(17) 2043-2045 2004

Hamid Dehghani, Nirmal Soni, Ryan Halter, Alex Hartov and Keith D Paulsen, "Excitation patterns in three-dimensional electrical impedance tomography" Physiol. Meas. 26 S185-S197 2005

Heng Xu, Roger Springett, **Hamid Dehghani**, Brian W Pogue, Keith D Paulsen and Jeff F Dunn, "MRI coupled Broadband Near Infrared Tomography System for Small Animal Brain Studies", Applied Optics 44(11) 2177-2188 2005

Hamid Dehghani, Ben Brooksby, Brian W Pogue and Keith D Paulsen, "Effect of Refractive Index on Near Infrared Tomography of the Breast" Applied Optics 44(10) 1870-1878, 2005

Subhadra Srinivasan, Brian W Pogue, Shudong Jiang, **Hamid Dehghani** and Keith D Paulsen, "Spectrally Constrained Chromophore and Scattering NIR Tomography Improved Quantification and Robustness of Reconstruction", Applied Optics 44(10) 1858-1869, 2005

Ben Brooksby, Shudong Jiang, **Hamid Dehghani**, Brian W. Pogue, Keith D. Paulsen, "Combining near infrared tomography and magnetic resonance imaging to study in vivo breast tissue: implementation of a Laplacian-type regularization to incorporate MR structure" JBO 2005 Accepted

Ben Brooksby, Subhadra Srinivasan, Shudong Jiang, **Hamid Dehghani**, Brian W. Pogue, Keith D. Paulsen, John Weaver, Christine Kogel and Steven P. Poplack, "Spectral-prior information improves Near-Infrared diffuse tomography more than spatial-prior" Optic Letters 2005 Accepted

Subhadra Srinivasan, Brian W. Pogue, **Hamid Dehghani**, Shudong Jiang, Xiaomei Song, Keith D. Paulsen, "Effect of image reconstruction bias upon spectroscopy-based quantification of chromophores in nearinfrared tomography" In Biomedical Topical Meetings on CD-ROM (The Optical Society of America, Washington, DC) 2004.

Ben A. Brooksby, Shudong Jiang, Gordon Ehret, **Hamid Dehghani**, Brian W. Pogue, Keith D. Paulsen, "Development of a system for simultaneous MRI and Near-infrared diffuse tomography to diagnose breast cancer In Biomedical Topical Meetings on CD-ROM (The Optical Society of America, Washington, DC) 2004.

Heng Xu, **Hamid Dehghani**, Brian W. Pogue, Keith D. Paulsen, Roger Springett, Jeff F. Dunn, "Optical tomography system based on second-differential spectroscopy for small animal brain study In Biomedical Topical Meetings on CD-ROM (The Optical Society of America, Washington, DC) 2004.

Brian Pogue, Shudong Jiang, Subhadra Srinivasan, Xiaomei Song, **Hamid Dehghani**, Keith Paulsen, Tor Tosteson, Christine Kogel, Sandra Soho, Steven P. Poplack, "Near-infrared scattering spectrum differences between benign and malignant breast tumors measured in vivo with diffuse tomography In Biomedical Topical Meetings on CD-ROM (The Optical Society of America, Washington, DC) 2004.

Hamid Dehghani, Brian W. Pogue, Marvin M. Doyley, Jason Geng, Keith D. Paulsen, "Breast deformation in near infrared optical tomography In Biomedical Topical Meetings on CD-ROM (The Optical Society of America, Washington, DC) 2004

Ben Brooksby, Subhadra Srinivasan, Brian W Pogue, Shudong Jiang, **Hamid Dehghani**, Christine Kogel, John Weaver, Steven Poplack, Justin D Pearlman and Keith D Paulsen, "Quantifying adipose and fibroglandular breast tissue properties using MRI-guided NIR tomography", Proceedings of SPIE 5693, 2005

Phaneendra K Yalavarthy, **Hamid Dehghani**, Brian W Pogue and Keith D Paulsen, "*Measurement optimization for Near-Infrared optical tomography*", Proceedings of SPIE 5693, 2005

Subhadra Srinivasan, Brian W Pogue, Shudong Jiang, **Hamid Dehghani** and Keith D Paulsen, "*Spectrally Constrained NIR tomography for breast Imaging: Simulations and Clinical Results*", Proceedings of SPIE 5693, 2005

Appendices

Four papers are included as appendices, which are as a direct result of the project funding:

Breast deformation modelling for image reconstruction in near infrared optical tomography

Hamid Dehghani¹, Marvin M Doyley², Brian W Pogue¹, Shudong Jiang¹, Jason Geng³ and Keith D Paulsen¹

¹ Thayer School of Engineering, Dartmouth College, Hanover, NH 03755, USA

² Department of Radiology, Dartmouth Medical School, Hanover, NH 03755, USA

³ Genex Technologies Inc., 10605 Concord Street, Suite 500 Kensington, MD 20895-2504, USA

Received 8 October 2003

Published 18 March 2004

Online at stacks.iop.org/PMB/49/1131 (DOI: 10.1088/0031-9155/49/7/004)

Abstract

Near infrared tomography (NIR) is a novel imaging technique that can be used to reconstruct tissue optical properties from measurements of light propagation through tissue. More specifically NIR measurements over a range of wavelengths can be used to obtain internal images of physiologic parameters and these images can be used to detect and characterize breast tumour. To obtain good NIR measurements, it is essential to have good contact between the optical fibres and the breast which in-turn results in the deformation of the breast due to the soft plasticity of the tissue. In this work, a tissue deformation model of the female breast is presented that will account for the altered shape of the breast during clinical NIR measurements. Using a deformed model of a breast, simulated NIR data were generated and used to reconstruct images of tissue absorption and reduced scatter using several assumptions about the imaging domain. Using either a circular or irregular 2D geometry for image reconstruction produces good localization of the absorbing anomaly, but it leads to degradation of the image quality. By modifying the assumptions about the imaging domain to a 3D conical model, with the correct diameter at the plane of NIR measurement, significantly improves the quality of reconstructed images and helps reduce image artefacts. Finally, assuming a non-deformed breast shape for image reconstruction is shown to lead to poor quality images since the geometry of the breast is greatly altered, whereas using the correct deformed geometry produces the best images.

(Some figures in this article are in colour only in the electronic version)

1. Introduction

Near infrared (NIR) tomography is an emerging alternative imaging method used to image physiologic parameters of biological tissue *in vivo* such as water and haemoglobin.

Measurements of light propagation (600–900 nm) within tissue can be used to map internal chromophore concentrations within tissue. Light is transmitted through tissue using multiple input and output locations on the surface of the region to be imaged, similar to a fan-beam x-ray computed tomography geometry, but using optical fibres for delivery and pick up of the light signals. The intensity and path-length distributions of the exiting photons provide information about the optical properties of the transilluminated tissue using a model-based interpretation where photon propagation is simulated by diffusion theory. Using these techniques implemented in hardware and software, NIR optical tomography becomes an inherently three-dimensional imaging method and is used to reconstruct physiologically relevant chromophore distributions from the region under investigation (Eda *et al* 1999, Fantini *et al* 1999, Boas *et al* 2001, Hebden *et al* 2001, Pogue *et al* 2001, McBride *et al* 2002, Dehghani *et al* 2003a, 2003b, 2003c). The main interest in this study lies in the ability to detect and characterize tumours within the female breast (Pogue *et al* 2001, Brooksby *et al* 2003). Since the absorption and scattering of light in tissue is a function of its optical properties, and hence its physiological state, the aim is to obtain images of internal optical absorption coefficient μ_a , reduced scattering coefficient μ_s' and ultimately images of total haemoglobin and oxygen saturation distributions. These images should in principle provide information about the physiological state of the tissue under investigation and help identify and characterize tumours within the breast. However, in recent years it has become apparent that the external shape of the tissue can dramatically impact the quality of the reconstruction, and this is largely due to mismatch between the model prediction and the actual shape of the tissue boundary. In this study, a focused effort has been put forward to examine the extent to which external boundary changes will degrade image quality and, more importantly, how this could be corrected with appropriate model-based analysis.

To obtain clinical measurements with a sufficient signal-to-noise ratio, it is key to ensure that good contact exists between the optical fibres and the tissue. More specifically to our studies, the patient lies prone on the measurement bed, which contains a single opening for the breast. The breast is suspended freely through this opening, below which the optical fibres are brought into contact with the breast. Normally, the optical fibre arrangement consists of a total of 48 fibres, 16 fibres in three separate planes. However, for the purpose of this work only one plane of 16 fibres is considered. The fibres need to make full contact with the breast for a good and adequate NIR measurement.

The breast is a soft tissue, which will deform and alter its shape on the application of external pressure. The amount of deformation is a function of the tissue mechanical properties and the amount of displacement and the external pressure applied by the optical fibre array. In most image reconstruction algorithms, the general assumption is made that the region under investigation is a uniform circular (2D) or conical or cylindrical (3D) domain. Little work has been done to evaluate the effect of any incorrect geometry in image reconstruction. For simple symmetric geometries, for example a 3D cylinder, work has been described to accurately calibrate the data to account for 2D/3D mismatch (Hillman *et al* 2000). More recently, work has been done with regard to neonatal head imaging that a slight change to the geometry model, both in terms of geometry and mesh, will result into large change in modelled data (Gibson *et al* 2003a).

In this work, the effect of such assumptions is investigated by creating a deformation of the breast model in 3D to generate simulated clinical data. Images are then reconstructed using various assumptions regarding the imaging domain including a circular or irregular 2D models as well as a 3D conical shaped model and the non-deformed breast model to evaluate image quality. An important part of this modelling effort is the recent advances which have been made in modelling soft tissue deformation (Paulsen *et al* 1999, Doyley *et al* 2000, Van Houten *et al*

2000). Beyond this, it is also becoming established that soft tissue elastic properties can be directly measured with elastography imaging *in vivo*, thereby providing the key information needed for predicting the deformation of tissue under force or displacement conditions. In this study, this displacement modelling was used along with the NIR tomography modelling to create a comprehensive three-dimensional prediction of how to approach appropriate modelling of deformed tissue that is being imaged with NIR tomography.

2. Theory

2.1. Breast deformation model

Soft tissues exhibit nonlinear elastic behaviour (Fung 1993). Nevertheless, it can be considered a linear elastic material in situations where the deforming forces produce infinitesimal deformations (i.e. $\leq 5\%$) (Timoshenko and Goodier 1970). For the purpose of this study, the breast was modelled as linear isotropic pseudo-incompressible (i.e. Poisson's ratio (ν) = 0.495 (Fung 1993)). Under these assumptions and ignoring internal body force, the governing elasticity equations for quasi-static deformation are given by Timoshenko and Goodier (1970) and Fung (1993)

$$(\lambda + \mu)\nabla(\nabla \cdot u) + \mu\nabla^2 u = 0 \quad (1)$$

for internal nodes in domain Ω , and

$$((\lambda + \mu)\nabla(\nabla \cdot u) + \mu\nabla^2 u) \cdot \hat{n} = h \quad (2)$$

for nodes on the boundary $\delta\Omega$.

Here \hat{n} represents a unit vector directed outwards from Ω , and h represents the traction on the surface or boundary of the breast. Note that u represents the displacement components in all coordinate directions, and μ and γ are Lamé's elastic constants. For an isotropic medium these constants are related to the more familiar Young's modulus (E) and the Poisson's ratio (ν) by

$$\mu = \frac{E}{2(1 + \nu)} \quad \lambda = \frac{\nu E}{(1 + \nu)(1 - 2\nu)}. \quad (3)$$

The first Lamé's elastic constant (i.e. μ) is generally known as shear modulus.

It should be stated that in this study, the breast was assumed to be traction free (i.e. no other forces are associated) and internal body forces were neglected, thus the problem is solved by imposing a prescribed displacement (i.e. induced when the optical fibres are coupled to the breast) as described in Doyley *et al* (1999).

2.2. Light propagation model

Under the assumption that scattering dominates absorption for NIR light in tissue, the Boltzmann transport equation can be simplified to the diffusion approximation, which in the frequency domain is given by

$$-\nabla \cdot D\nabla\Phi(r, \omega) + \left(\mu_a + \frac{i\omega}{c}\right)\Phi(r, \omega) = q_0(r, \omega) \quad (4)$$

where $q_0(r, \omega)$ is an isotropic source, $\Phi(r, \omega)$ is the photon fluence rate at position r and $D = \frac{1}{3(\mu_a + \mu_s')}$ is the diffusion coefficient. We use the Robin (Type III) boundary condition:

$$\Phi(\gamma) + \frac{D}{\alpha}\hat{n} \cdot \nabla\Phi(\gamma) = 0 \quad (5)$$

where α is a term which incorporates reflection as a result of refractive index mismatch (Schweiger *et al* 1995, Dehghani *et al* 2003c) at the boundary, and \hat{n} is the outward pointing normal to the boundary ($\delta\Omega$) at γ .

We assume that the data are represented by a nonlinear operator $y^* = F[\mu_a, D]$, where our data y^* are a complex vector having a real and imaginary components, which are mapped to log amplitude and phase shift in measurement. Then the image reconstruction method is posed as a solution to the following expression:

$$(\hat{\mu}_a, \hat{D}) = \arg \min_{\mu_a, D} \|(y^* - F(\mu_a, D))\| \quad (6)$$

where $\|\cdot\|$ is the weighted L2-norm, representing the square root of the sum of the squared elements, $\hat{\mu}_a$ is a vector of the absorption coefficients and \hat{D} is a vector of the diffusion coefficients. The magnitude of this is sometimes referred to as the projection error and provides a value for determining the convergence of the iterative reconstruction algorithm.

In this study, a finite-element method (FEM) is used as a general and flexible method for solving the forward problem in arbitrary geometries (Arridge *et al* 1993, Jiang *et al* 1996). In the inverse problem, where the goal is to recover internal optical property distributions from boundary measurements, it is assumed that $\mu_a(\mathbf{r})$ and $D(\mathbf{r})$ are expressed in a basis with a limited number of dimensions (less than the dimension of the finite element system matrices). A number of different strategies for defining reconstruction bases are possible; in this paper a linear pixel basis (Schweiger and Arridge 1999) is used. To find $(\hat{\mu}_a, \hat{D})$ in equation (6) we have used a Levenberg–Marquardt algorithm, where we repeatedly solve:

$$\hat{a} = J^T (J J^T + \rho I)^{-1} \hat{b} \quad (7)$$

where \hat{b} is the data vector, $\hat{b} = [y^* - F[\mu_a, D]]^T$, \hat{a} is the solution update vector, $\hat{a} = [\delta\hat{D}; \delta\hat{\mu}_a]$. Here, ρ is the regularization factor and J is the Jacobian matrix for our model which is calculated using the Adjoint method (Arridge and Schweiger 1995, Dehghani *et al* 2003b, 2003c).

3. Methods

3.1. Breast deformation

A volume mesh of a female breast of a volunteer was created from surface image data that was acquired using a 3D surface camera (Rainbow 3D Camera, Genex Technologies, Kensington MD). The 3D camera projects structural illumination patterns onto the object and calculates 3D surface profile described by over 300 000 data points (Geng 1996, Galdino *et al* 2002). A volume mesh is then generated using the Delaunay algorithm. The mesh has a geometry of $130 \times 136 \times 60$ mm, figure 1(a), and contained 15 501 nodes corresponding to 61 171 linear tetrahedral elements. The diameter of the breast at its mid-plane where optical fibre array will be applied is approximately 88 mm. To calculate the deformation due to 16 equally spaced optical fibres being applied at the mid-plane of the breast, i.e. $z = -30$ mm, it is assumed that each optical fibre pushed the breast so that the final breast diameter at $z = -30$ mm is 70 mm, and that the diameter of each optical fibre is 6 mm. The modelled elastic properties of tissue, equation (3), were assumed as isotropic and homogenous with Young's modulus of 20 kPa (Krouskop *et al* 1998) and Poisson's ratio of 0.495 (Fung 1993). Further, it was assumed that the topmost part of the mesh, i.e. $z = 0$ mm was not allowed to move since it is connected to the chest. Using this applied displacement as a boundary condition, the displacement at all nodes due to the application of the optical fibres was calculated and a deformed mesh was created, figure 1(b).

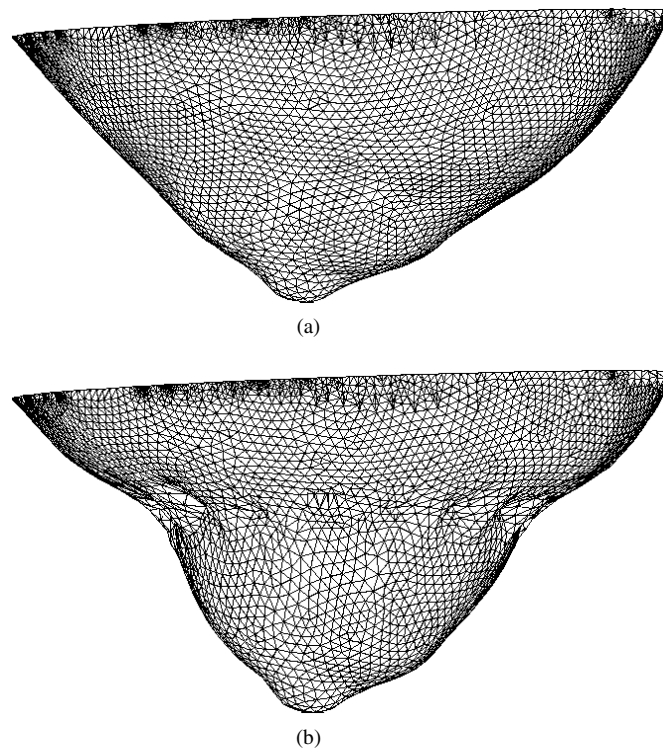


Figure 1. Volume mesh of the (a) normal suspended breast and (b) the deformed mesh after the application of the optical fibre array.

3.2. Simulation of data from deformed breast

In order to accurately simulate the clinical settings, two localized anomaly regions were placed within the mid-plane of the normal breast, both at $z = -30$ mm, figure 2(a). First was an absorbing anomaly, 19 mm from the surface and a radius 10 mm with a coefficient value of 0.03 mm^{-1} . Second was a reduced scattering anomaly, also 19 mm from the surface but with a radius of 7.5 mm and a value of 3 mm^{-1} . These anomalies were chosen as they represent the size and contrast we aim to image and so that absorption and scatter separation can also be investigated. The background optical properties were modelled with an absorption coefficient of 0.01 mm^{-1} and a reduced scatter coefficient of 1.0 mm^{-1} . For the deformed breast model the same optical properties of the normal breast were assumed (the anomalies were also assumed to have the same elastic properties of the background). Once the deformation of the model was calculated, it was assumed that the anomalies were free to move, depending on the elastic properties of the breast, figure 2(b). It is interesting to note that the displacement of the anomalies is not so much dependent on the mesh density of the breast, but more dependent on the mechanical properties, applied pressure and non-symmetric nature of the breast.

Using the deformed mesh, together with the displaced anomalies, data were simulated for 16 equally circularly spaced optical fibres placed at $z = -30$ mm. Amplitude and phase data were simulated at 100 MHz, and 1% noise was added. These data were then used as simulated patient data in the following sections. In addition, to allow data calibration as done using clinical data, and discussed elsewhere (Dehghani *et al* 2003c, McBride *et al* 2003), the data were simulated for 16 equally spaced optical fibres placed in a circle around the mid-plane of a

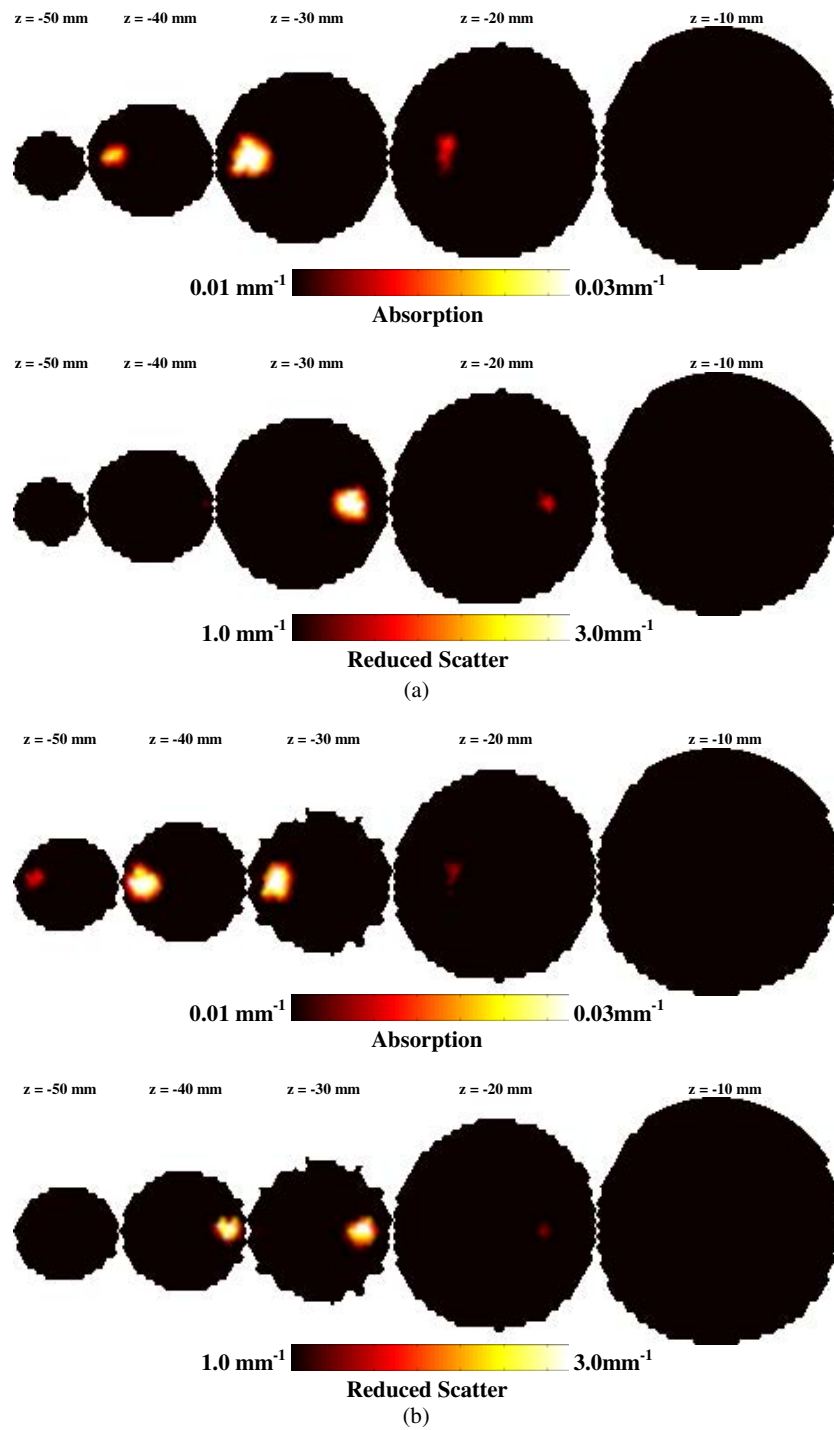


Figure 2. 2D coronal slices through (a) the normal breast mesh and (b) the deformed breast mesh, showing the position of the anomalies. The most right-hand slice is near the chest while the most left-hand slice is near the nipple.

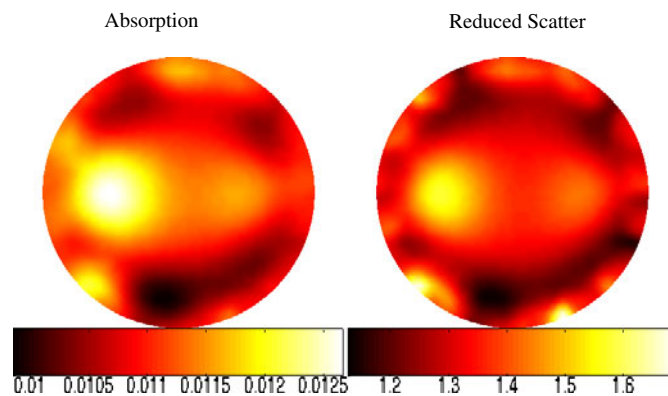


Figure 3. 2D simultaneous reconstruction of absorption and reduced scatter from deformed breast model simulated data. The mesh used for the reconstruction is a circular mesh whose diameter is the same as the optical fibre array diameter used to deform and simulate data NIR from the breast model.

non-deformable cylindrical model with a known homogenous background optical properties. The same calibration data file has been used for all presented reconstructions.

3.3. Image reconstruction using 2D meshes

Using the computed data for the deformed mesh and the reference phantom, as simulated measurements with 1% random noise added, the data were calibrated (Dehghani *et al* 2003c, McBride *et al* 2003) and images were reconstructed using two different 2D meshes. Assuming that the imaging domain was a circular domain with a radius equal to the radius of the optical fibre array, i.e. 35 mm, images were reconstructed and the results are shown in figure 3. The circular mesh used contained 1785 nodes corresponding to 3418 linear triangular elements. For the reconstruction basis (basis used for the update of the optical parameters), a 20×20 regular grid (piecewise linear) was used and the initial regularization parameter was set to 100. Images shown here, and all following sections are at iteration level where the projection error was within 5% of the previous iteration. In the 2D reconstruction cases, this projection error was reached typically in the 7th iteration.

It is evident from figure 1(b) that the breast at the plane of measurement, i.e. $z = -30$ mm, was no longer circular. In order to evaluate if a more correct *a priori* information regarding the 2D boundary at the plane of measurement would be useful, a 2D irregular mesh, with a boundary whose profile is the same as the boundary at $z = -30$ mm for the deformed mesh, was created and used for image reconstruction. The resulting images reconstructed on this mesh are shown in figure 4. The irregular mesh used contained 2405 nodes corresponding to 4619 linear triangular elements. For the reconstruction basis, a 20×20 regular grid was used and the initial regularization parameter was set to 100. Thus in this case, the irregular boundary was matched, but still the image reconstruction was approximated by a 2D forward solution.

3.4. Image reconstruction using 3D conical mesh

In the next section, we examined the improvement if a true 3D forward calculation was assumed, but with a regular geometry. In a previous work, it was hypothesized that given a set of 3D patient data, those images could be reconstructed with reasonable accuracy if

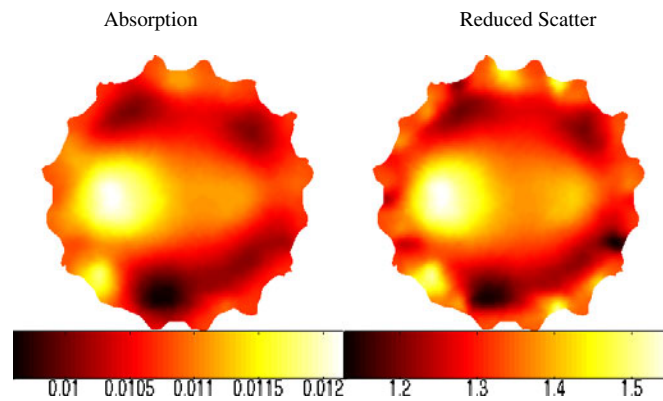


Figure 4. 2D simultaneous reconstruction of absorption and reduced scatter from deformed breast model simulated data. The mesh used for the reconstruction is an irregular whose boundary is the same as the boundary of the deformed breast mesh at $z = 30$ mm.

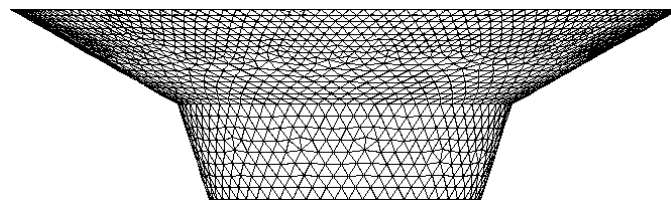


Figure 5. The conical shaped volume mesh. The geometry of the mesh is such that the diameter at the mid-plane corresponds to the diameter of the optical fibre array used to deform and simulate NIR data of the breast model. The diameter at 20 mm above and 20 mm below the NIR measurement plane of the deformed breast were also used to set the upper and lower bound of the cone model.

the breast was assumed to be a conical shaped model (Dehghani *et al* 2003c). To create a conical mesh, the information about the diameter of the measurement fibre array as well as the diameter of the breast at 20 mm above and 20 mm below the measurement plane was used, which would include all boundary information other than effects due to tissue bulging. Following this procedure, a conical shaped volume mesh was created, as shown in figure 5, which shows the upper chest wall and the confined partial-conical breast shape as a regular geometry approximation to the circularly compressed breast shape. The mesh contained 9332 nodes corresponding to 42 281 linear tetrahedral elements and was created using NETGEN (Schoberl). Using this mesh and the simulated data for the deformed breast mesh, images were reconstructed and the results are shown in figure 6.

For the reconstruction basis, a $20 \times 20 \times 10$ regular grid was used and the initial regularization parameter was set to 100. The images shown here and all through the following section are at iteration level where the projection error was within 5% of the previous iteration. These presented from the 3D cases are from the 14th iteration.

3.5. Image reconstruction using the normal and deformed breast mesh

Assuming that correct information regarding the breast is available, before the application of the optical fibre array, the normal, non-deformed mesh was used as shown in figure 1(a),

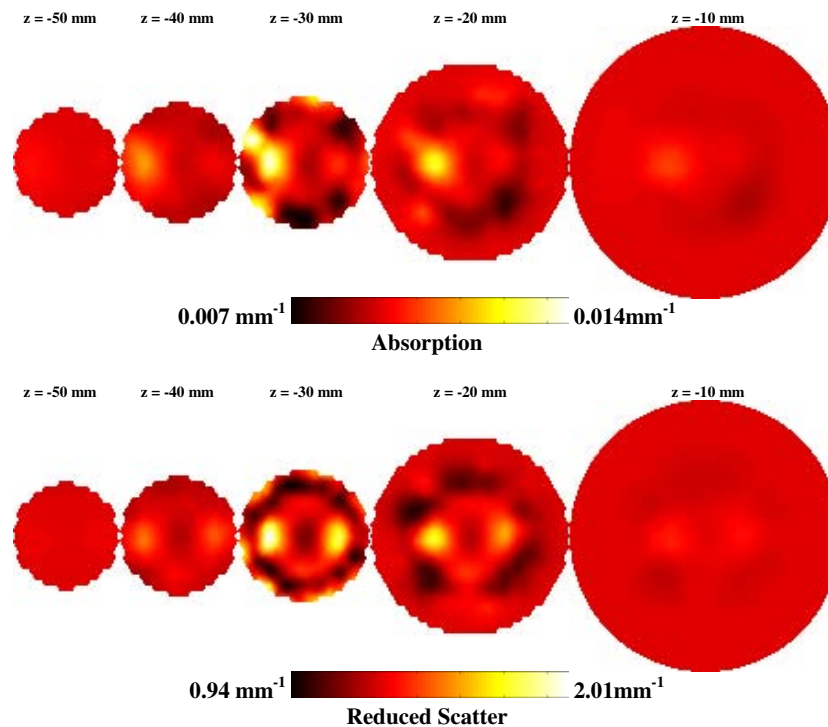


Figure 6. 3D simultaneous reconstruction of absorption and reduced scatter from deformed breast model simulated data. The mesh used for the reconstruction is the mesh shown in figure 5. The most right-hand slice is near the chest while the most left-hand slice is near the nipple.

as the reconstruction mesh for the images shown in figure 7. The reconstruction basis and parameters used were the same as for the conical model already described. Finally, to show the best possible reconstruction, the deformed mesh, figure 1(b) was used for reconstruction of images and these are shown in figure 8.

4. Results

The deformed breast mesh, as a result of applying a circular optical fibre array at $z = 30$ mm, is shown in figure 1(b). It is evident that the mesh has been compressed at the plane of applied displacement with slight bulging in-between each optical fibre. The breast mesh has also extended in the z direction near the nipple to maintain a constant volume as the nodes on the chest wall are assumed fixed. Although the mechanical properties of the tissue are assumed constant, it is interesting to note that the modelled anomalies have also been displaced due to the deformation, figures 2(a) and (b). Both the anomalies have been reduced in diameter, but have extended in the z direction as a result of the applied deformation.

Two-dimensional images reconstructed using the simulated deformed breast data are shown in figures 3 and 4. In both cases where a circular or an irregular boundary was used, good images were recovered in terms of localization of the absorption anomaly (within 1.2 mm for the circular model, and 2.0 mm for the irregular model). The recovery of the

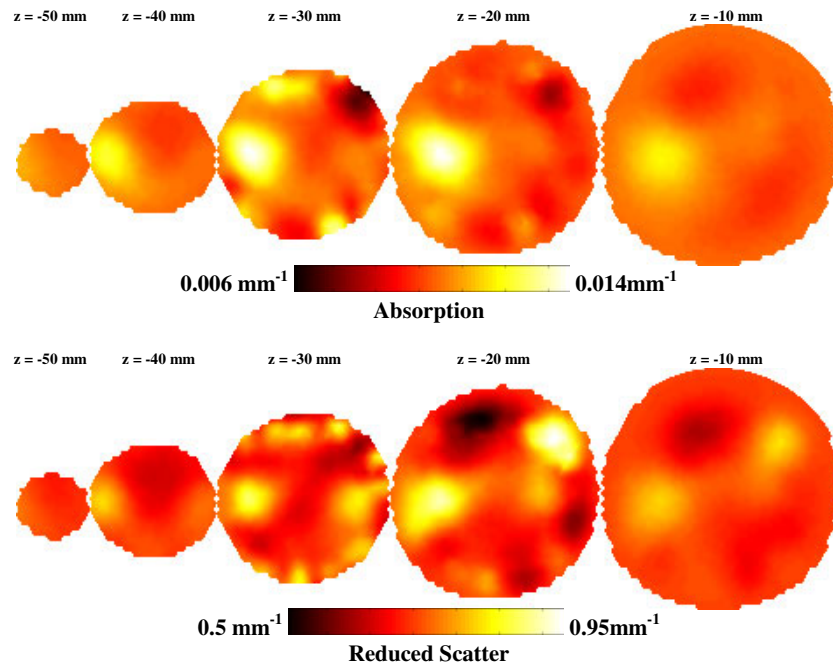


Figure 7. 3D simultaneous reconstruction of absorption and reduced scatter from deformed breast model simulated data. The mesh used for the reconstruction is the mesh shown in figure 1(a). The most right-hand slice is near the chest while the most left-hand slice is near the nipple.

reduced scattering anomaly was not as good as the absorption, and both sets of images contain large boundary artefacts. The background values of both the absorption and reduced scatter were close to the expected value, however, the target absorption value is less than 50% than expected.

Three-dimensional images reconstructed assuming a conical shaped breast are shown in figure 6. In that case, both the absorption and the scattering anomalies were recovered with good localization (within 2.00 mm for both the absorption and scattering objects) and with little boundary artefacts. Since the measured data were about the mid-plane of the breast, and the modelled cone geometry also had the optical fibres around its mid-plane, the objects recovered are centred at $z = -30$ mm. Here the background values of absorption and scatter were a little lower than expected values, however, the absorption anomaly had a maximum value of 0.014 mm^{-1} and the scattering object had a maximum value of 2 mm^{-1} .

Images reconstructed using the assumption of correct non-deformed breast geometry are shown in figure 7. In this case, although the absorbing anomaly has been reconstructed, the reduced scattering images contain large artefacts. The background absorption and scatter values are about 0.006 mm^{-1} and 0.5 mm^{-1} , respectively, while the maximum absorption for the anomaly is 0.014 mm^{-1} . Finally, images reconstructed assuming correct 3D deformed boundary are shown in figure 8. Here, both the absorbing and scattering regions have been recovered within less than 1.00 mm of expected location, giving great localization accuracy. There exists some cross talk between the absorbing and scattering anomalies. The background absorption and scatter values are about 0.01 mm^{-1} and 0.98 mm^{-1} , respectively, while the maximum absorption and scatter values for the anomaly is 0.013 mm^{-1} and 1.3 mm^{-1} , respectively.

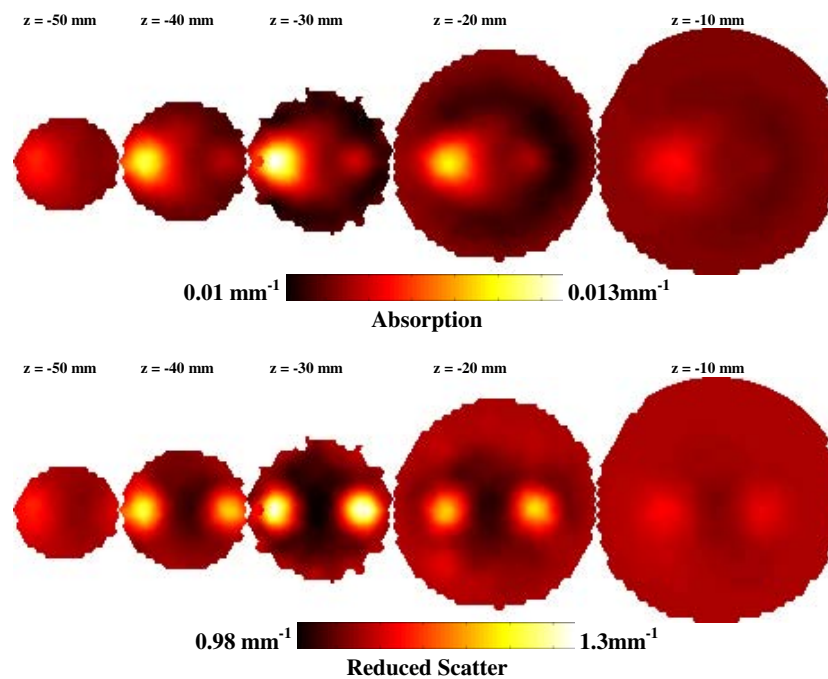


Figure 8. 3D simultaneous reconstruction of absorption and reduced scatter from deformed breast model simulated data. The mesh used for the reconstruction is the mesh shown in figure 1(b). The most right-hand slice is near the chest while the most left-hand slice is near the nipple.

5. Discussions

The deformation of the breast due to the application of 16 circular equally spaced optical fibres has been modelled using a computational mechanic model. Using this deformed model which also contains a single absorbing and a single scattering perturbations, data were simulated and 1% noise was added to more adequately represent clinical measurements. Using these simulated data, reconstructed images of absorption and reduced scatter were generated simultaneously using various different geometries of the mesh upon which the reconstruction would take place. In the first case, it was assumed that the model used for reconstruction was circular with a radius equal to the radius of the optical fibre array after breast compression, which was 35 mm. The reconstructed images have shown good accuracy in the localization of the absorbing object with a maximum absorption value of 0.014 mm^{-1} . The recovery of the scattering objects is much poorer than the absorbing anomaly, which can be attributed, perhaps, to its small size (15 mm diameter). There exist boundary artefacts in both the absorbing and scattering images. It is possible to improve the quality of the reconstructed 2D images by using several methods, including the use of various regularization parameters and/or use of *a priori* information. A good method to improve the reconstructed images in this case would be to segment the reconstructed images shown in figure 3, and use these as *a priori* information to more accurately obtain quantitative results. The application of such algorithm is discussed elsewhere, and has been found to provide superior results (Srinivasan *et al* 2004). In the case of knowing and using correct 2D boundary information in image reconstruction, figure 4, no useful improvement was seen. Although correct information was added to the reconstruction

with regard to the boundary, the image reconstruction algorithm was still constrained to be 2D. While it has been shown many times that the 2D geometry can be used to recover accurate image data from NIR tomography with a circular boundary (Pogue and McBride 1999), it is not surprising, perhaps, to find that this simplification does not continue to work as the exterior boundary becomes more complex in shape. The reconstruction mesh is no longer symmetric and contains many irregular edges, which gives rise to high frequency noise at the boundary, and those changes occur symmetrically around each optical fibre making the calculation even more dependent upon the 3D geometry out of the plane of imaging.

Next for the case where the imaging domain was assumed to be conical in shape, the reconstructed images were shown in figure 6. Here it was assumed that the mid-plane of the cone had a radius equal to the radius of the optical fibre array after breast compression. Further, it was assumed that the measurements of the diameter of the breast 20 mm above and 20 mm below the measurement plane were known. Using these data, a conical shaped mesh could be created for any patient exam as shown in figure 5. The reconstructed images had recovered both the absorbing and scattering anomalies with reasonable success. The calculated background values for absorption and scatter were 0.007 mm^{-1} and 0.94 mm^{-1} , respectively. There exists a small cross talk between the absorption and reduced scatter images, plus artefacts at the boundary of the images. The qualitative and quantitative accuracy of the conical shaped model reconstruction are better than the 2D circular case, simply because a more accurate 3D model, rather than a 2D model is used.

In the case where it is assumed that the exact breast geometry was known, but have ignored information regarding the compression due to the optical fibres, the resulting images are shown in figure 7. Here, although the absorption anomaly was recovered with relatively good accuracy, the reduced scattering image contains a large artefact. Furthermore, the calculated background values for absorption and scatter are 0.006 mm^{-1} and 0.5 mm^{-1} , respectively, which are much lower than expected. These images are, perhaps, not as accurate and useful as the conical geometry case, since, although there is a more accurate 3D model, the diameter of the breast was not correct, particularly within the measurement plane, i.e. $z = -30 \text{ mm}$. Finally, for the case of using a geometrically correct deformed mesh to reconstruct, the images are shown in figure 8. Here, the reconstructed images of absorption and scatter were found with superior localization accuracy. The scattering object has also been recovered in this case. However, the quantitative accuracy of the recovered anomalies is not as good with maximum values for absorption and scattering objects of 0.013 mm^{-1} and 1.3 mm^{-1} , respectively. This low quantitative accuracy has been reported elsewhere and is a common problem in 3D NIR imaging algorithms (Dehghani *et al* 2003b, Gibson *et al* 2003b), which may be solved using of multistage reconstruction algorithms (Srinivasan *et al* 2004) or with inclusion of *a priori* data (Brooksby *et al* 2003). Finally, using the correct model with correct information regarding the deformed boundary has produced images with very little or no artefacts.

6. Conclusions

In this work, we have presented a breast deformation model that would account for the change in shape and geometry of the breast due to the application of a circular array of optical fibres for NIR measurements. The proposed model, at present, assumes that the breast has homogenous mechanical properties, which, although not accurate, provide a good initial estimate for modelling of any deformation. Future studies may focus on using spatially

distributed mechanical properties, as these can be imaged with good spatial resolution with MR elastography (Paulsen *et al* 1999, Van Houten *et al* 2000, Weaver *et al* 2001, Doyley *et al* 2003). Also, in this work, we have deformed the breast more than adequately needed by 19 mm, whereas in a real clinical setting, the deformation will be of lower magnitude, typically about 5–10 mm. In practice for our imaging exams, we currently attempt to deform the breast as minimally as possible, however, there are strategic benefits to compressing in that the signal transmitted can be higher, and there can be pressure-induced changes which might provide meaningful contrast about what the tissue is composed of (Jiang *et al* 2003). Nevertheless we have chosen such a large deformation to provide us with a worst-case scenario for NIR image reconstruction, and to examine if it is feasible to exploit larger magnitude deformations in clinical studies while not compromising the integrity of the data collected from the breast.

Using simulated data from the deformed breast that also contains optical anomalies, we have reconstructed images assuming various reconstruction geometries. In the first case of assuming that the reconstruction mesh is either a circular or irregular 2D mesh, the reconstructed images have shown good accuracy in recovering the location of the absorbing anomaly. The 2D reconstructed scattering images are not as good as expected, which is perhaps due to the fact that the scattering object had a small diameter of 15 mm and a contrast which was three times the background, and thus the image being dominated by boundary artefacts. Also it is evident from the reconstructed images that there exist large boundary artefacts which are due to the incorrect model. However, both the quality and quantitative accuracy of 2D image reconstruction will be improved by the incorporation of *a priori* information as well as a multi-step image reconstruction where regions of interest can be identified and isolated for regional reconstruction.

In the case of 3D image reconstruction, assumptions regarding the breast not being deformed might be used and the reconstructed images provide relatively good absorption distributions, but the images contain large artefacts which will likely confound their interpretation. The reason for this can be explained by considering the overall shape of the breast before and after deformation. The non-deformed mesh at the plane of measurement has radius that is 19 mm larger than the deformed mesh. Additionally, as evident from figures 1(a) and 1(b), it is found that the breast expands above, below and between each optical fibre once compressed. This large change in shape of the breast contributes to the large artefacts seen within the reconstruction. However, if one assumes that the diameter of the breast is known within the measurement plane, as well as an approximate diameter above and below it, it is possible to create a pseudo-3D conical shaped mesh for image reconstruction. Images reconstructed using this 3D conical mesh have shown a better accuracy in recovering both the absorbing and scattering anomalies. Finally, if accurate knowledge regarding the breast deformation is available, images of optical properties can be reconstructed which localize both anomalies with great accuracy, and also contain little or no artefact which otherwise would arise from model mismatch.

The goal of this work is to incorporate this new model of breast deformation with more accurate information regarding the mechanical properties of the breast to improve the NIR image reconstruction. The mechanical property information is readily available from other imaging modalities, and the synthesis of this information may provide fundamentally new information about breast physiologic response to pressure, and/or breast pathology response to pressure. An accurate model of breast deformation should in principle allow us to create patient specific models and meshes, which would in-turn provide more clinically useful data. Work is in progress to validate and further improve the deformation model with application to the female breast imaging.

Acknowledgments

This work has been sponsored by the National Cancer Institute through grants RO1CA69544 and PO1CA80139 and DOD Breast cancer research programme DAMD17-03-01-0405.

References

- Arridge S R and Schweiger M 1995 Photon-measurement density functions. Part2: finite-element-method calculations *Appl. Opt.* **34** 8026–37
- Arridge S R, Schweiger M, Hiraoka M and Delpy D T 1993 A finite element approach for modelling photon transport in tissue *Med. Phys.* **20** 299–309
- Boas D A, Brooks D H, Miller E L, DiMarzio C A, Kilmer M, Gaudette R J and Zhang Q 2001 Imaging the body with diffuse optical tomography *IEEE Signal Process. Mag.* **18** 57–75
- Brooksby B, Dehghani H, Pogue B W and Paulsen K D 2003 Infrared (NIR) tomography breast image reconstruction with *a priori* structural information from MRI: algorithm development for reconstructing heterogeneities *IEEE J. Sel. Top. Quantum Electron.* **9** 199–209
- Dehghani H, Brooksby B, Vishwanath K, Pogue B W and Paulsen K D 2003a The effects of internal refractive index variation in near infrared optical tomography: a finite element modelling approach *Phys. Med. Biol.* **48** 2713–27
- Dehghani H, Pogue B W, Jiang S, Brooksby B and Paulsen K D 2003b Three dimensional optical tomography: resolution in small object imaging *Appl. Opt.* **42** 3117–28
- Dehghani H, Pogue B W, Poplack S P and Paulsen K D 2003c Multiwavelength three-dimensional near-infrared tomography of the breast: initial simulation, phantom, and clinical results *Appl. Opt.* **42** 135–45
- Doyle M M, Meaney P M and Bamber J C 2000 Evaluation of an iterative reconstruction method for quantitative elastography *Phys. Med. Biol.* **45** 1521–40
- Doyle M M, Weaver J B, Van Houten E E, Kennedy F E and Paulsen K D 2003 Thresholds for detecting and characterizing focal lesions using steady-state MR elastography *Med. Phys.* **30** 495–504
- Eda H, Oda I, Ito Y, Wada Y, Oikawa Y, Tsunazawa Y, Tsuchiya Y, Yamashita Y, Oda M, Sassaroli A, Yamada Y and Tamaru M 1999 Multichannel time-resolved optical tomographic imaging system *Rev. Sci. Instrum.* **70** 3595–602
- Fantini S, Franceschini M A, Gratton E, Hueber D, Rosenfeld W, Maulik D, Stubblefield P G and Stankovic M R 1999 Non-invasive optical mapping of the piglet in real time *Opt. Exp.* **4** 308–14
- Fung Y C 1993 *Mechanical Properties of Living Tissue* (Berlin: Springer)
- Galdino G M, Manson P N, Nahabedian M, Chang B, Zhuang P, Geng J Z and Vander Kolk C A 2002 Three dimensional photography in plastic surgery: clinical applications for breast surgery *Plastic Reconstr. Surg.* **110** 1–13
- Geng Z 1996 Rainbow 3D camera—a new concept for high speed and low-cost 3D vision *J. Opt. Eng.* **35** 376
- Gibson A, Riley J, Schweiger M, Hebden J c, Arridge S R and Delpy D T 2003a A method for generating patient specific finite element meshes for head modelling *Phys. Med. Biol.* **48** 481–95
- Gibson A, Yusof R M, Hillman E M C, Dehghani H, Riley J, Everdale N, Richards R, Hebden J C, Schweiger M, Arridge S R and Delpy D T 2003b Optical tomography of a realistic neonatal head phantom *Appl. Opt.* **42** 1–8
- Hebden J C, Veenstra H, Dehghani H H, Hillman E M C, Schweiger M, Arridge S R and Delpy D T 2001 Three dimensional time-resolved optical tomography of a conical breast phantom *Appl. Opt.* **40** 3278–87
- Hillman E, Hebden J C, Schmidt F E W, Arridge S R, Schweiger M, Dehghani H and Delpy D T 2000 Calibration techniques and datatype extraction for time-resolved optical tomography *Rev. Sci. Instrum.* **71** 3415–27
- Jiang H, Paulsen K D, Osterberg U L, Pogue B W and Patterson M S 1996 Optical image reconstruction using frequency-domain data: simulations and experiments *J. Opt. Soc. Am. A* **13** 253–66
- Jiang S, Pogue B W, Paulsen K D, Kogel C and Poplack S P 2003 *In vivo* near-infrared spectral detection of pressure-induced changes in breast tissue *Opt. Lett.* **28** 1212–4
- Krouskop T A, Wheeler T M, Kallel F, Garra B S and Hall T 1998 Elastic moduli of breast and prostate tissues under compression *Ultrason. Imaging* **20** 260–74
- McBride T O, Pogue B W, Jiang S, Osterberg U L, Paulsen K D and Poplack S P 2002 Multi-spectral near-infrared tomography: a case study in compensating for water and lipid content in haemoglobin imaging of the breast *J. Biomed. Opt.* **7** 72–9
- McBride T O, Pogue B W, Osterberg U L and Paulsen K D 2003 Strategies for absolute calibration of near infrared tomographic tissue imaging *Oxygen Transport Tissue XXIV* (Dordrecht: Kluwer) pp 85–99
- Paulsen K D, Miga M I, Kennedy F E, Hoopes P J, Hartov A and Roberts D W 1999 A computational model for tracking subsurface tissue deformation during stereotactic neurosurgery *IEEE Trans. Biomed. Eng.* **46** 213–25

- Pogue B W, Geimer S, McBride T O, Jiang S, Österberg U L and Paulsen K D 2001 Three-dimensional simulation of near-infrared diffusion in tissue: boundary condition and geometry analysis for finite element image reconstruction *Appl. Opt.* **40** 588–600
- Pogue B W and McBride T *et al* 1999 Comparison of imaging geometries for diffuse optical tomography of tissue *Opt. Exp.* **4** 270–86
- Schoberl J *NETGEN—An Automatic 3D Tetrahedral Mesh Generator* <http://www.sfb013.uni-linz.ac.at/~joachim/netgen/>
- Schweiger M and Arridge S R 1999 Optical tomographic reconstruction in a complex head model using *a priori* region boundary information *Phys. Med. Biol.* **44** 2703–22
- Schweiger M, Arridge S R, Hiroaka M and Delpy D T 1995 The finite element model for the propagation of light in scattering media: boundary and source conditions *Med. Phys.* **22** 1779–92
- Srinivasan S, Pogue B W, Dehghani H, Jiang S, Song X and Paulsen K D 2004 Improved quantification of small objects in near-infrared diffuse optical tomography *J. Biomed. Opt.* at press
- Timoshenko S P and Goodier J N 1970 *Theory of Elasticity* (Singapore: McGraw-Hill)
- Van Houten E E, Weaver J B, Miga M I, Kennedy F E and Paulsen K D 2000 Elasticity reconstruction from experimental MR displacement data: initial experience with an overlapping subzone finite element inversion process *Med. Phys.* **27** 101–7
- Weaver J B, Van Houten E E, Miga M I, Kennedy F E and Paulsen K D 2001 MR elastography using 3D gradient echo measurements of steady state motion *Med. Phys.* **28** 1620

Magnetic resonance-guided near-infrared tomography of the breast

Ben Brooksby, Shudong Jiang, Hamid Dehghani, Brian W. Pogue, and Keith D. Paulsen

Thayer School of Engineering, Dartmouth College, Hanover, New Hampshire 03755

Christine Kogel, Marvin Doyley, John B. Weaver, and Steven P. Poplack

Department of Diagnostic Radiology, Dartmouth Medical School, Hanover, New Hampshire 03755

(Received 13 May 2004; accepted 14 September 2004; published 15 November 2004)

The design and implementation of a multispectral, frequency-domain near infrared tomography system is outlined, which operates in a MRI magnet for utilization of MR-guided image reconstruction of tissue optical properties. Using long silica optical fiber bundles, measurements of light transmission through up to 12 cm of female breast tissue can be acquired simultaneously with MRI scans. The NIR system utilizes six optical wavelengths from 660 to 850 nm using intensity modulated diode lasers nominally working at 100 MHz. Photomultiplier tube detector gain levels are electronically controlled on a time scale of 200 ms, thereby allowing rapid switching of the source to locations around the tissue. There are no moving parts in the detection channels and for each source position, 15 PMTs operating in parallel allow sensitivity down to 0.5 pW/cm^2 at the tissue surface. Images of breast tissue optical absorption and reduced scattering coefficients are obtained using a Newton-type reconstruction algorithm to solve for an optimal solution using the measurement data. In medical imaging, it is beneficial to compare the same tissue volume as seen by a variety of modalities, and perhaps more importantly, there is the hypothesis that one imaging system which has high spatial resolution can be used to enhance the reconstruction of another system which has good contrast resolution. In this study we explore the synergistic benefits of a combined NIR-MRI data set, specifically the ways in which MRI (i.e., high spatial resolution) enhances NIR (i.e., high contrast resolution) image reconstruction. The design, calibration, and performance of the imaging system are described in the context of preliminary phantom tests and initial *in vivo* patient imaging. Co-registered MRI validates and improves optical property estimation in 2D tomographic image reconstructions when specialized algorithms are used. © 2004 American Institute of Physics. [DOI: 10.1063/1.1819634]

I. INTRODUCTION

Diffuse optical tomography (DOT) with near infrared (NIR) light can be used to produce spatially resolved images of tissue optical properties. These optical property maps can be acquired at different wavelengths and combined to reveal hemoglobin concentration, oxygen saturation, water and fat content, as well as a description of scattering structures.^{1–5} These latter parameters are important indicators of metabolic activity, functional processes, or presence and staging of disease. NIR diffuse tomography generally suffers from comparatively low spatial resolution due to the multiple scattering events that occur along each photon path.^{6–8} However, the promise of this imaging modality lies in the fact that it affords new physical bases for contrast in tissue. For example, hemoglobin-based contrast in tumors relative to normal tissue is exceptionally high (i.e., between 100%–300%).⁹ However, improving the limitations associated with its low spatial resolution is fundamental to implementing this technology clinically. *A priori* knowledge of tissue structure can be used to constrain/guide the iterative NIR image reconstruction process, and improve the spatial resolution and quantitative accuracy of recovered physiological parameters. Consequently, NIR techniques have been combined with several high spatial-resolution, structure-bearing imaging mo-

dalities including x-ray tomosynthesis,¹⁰ ultrasound (US),¹¹ and magnetic resonance imaging (MRI),^{12–14} to study human tissues and small animals. In this report, we present a combined NIR-MRI system for imaging female breast tissue, and explore the benefits of the combined data set in a planar tomographic geometry where the breast is imaged pendent in a standard MR breast coil.

In recent years, several important technological factors have contributed to the advancement of NIR spectral imaging applied to breast cancer characterization, including an increased understanding of light and tissue interaction, and new software-based developments in image-reconstruction algorithms for DOT.⁵ NIR radiation (700–900 nm) is nonionizing, light delivery and detection instrumentation is relatively inexpensive, and uncomfortable tissue compression is not required (as in mammographic level compression). Detection systems with high signal-to-noise ratios can routinely measure NIR light transmission through 10 cm of breast tissue. This distance may increase to 12 cm for breasts with fatty composition (i.e., lower radiographic density and NIR attenuation). Photon propagation within the breast is well described by diffusion theory since the probability of photon scattering is much greater than absorption. Light transmission measurements can be combined with diffusion theory to provide robust image reconstruction of tissue optical coeffi-

cients. We use a Newton-type algorithm to solve for the optimal solution that provides a minimum error between the measured data and predicted response from a model of the frequency-domain diffusion equation.¹⁵ In theory, the approach allows separation of the absorption and reduced scattering coefficients (μ_a and μ'_s). Frequency-domain measurements of optical flux provide both amplitude and time-based (i.e., phase shift) information—a unique data set to solve the estimation problem associated with recovering both coefficients simultaneously.

A variety of imaging methods have achieved high-spatial-resolution imaging with acceptable to excellent soft tissue contrast, including x-ray computed tomography (CT), US, and MRI. These techniques primarily provide images of tissue structure and have a limited ability to monitor parameters related to tissue function other than through the introduction of exogenous contrast agents. Alternatively, nuclear medicine approaches are routinely used to image tissue functions, such as metabolic fluorodeoxyglucose uptake,¹⁶ and many commercial systems exist to co-register these images with the structural data derived from CT, US, and MRI. The combination of high resolution structural imaging with lower resolution functional information is a major emphasis in contemporary medical imaging, and customized hybrid imaging systems are being developed to avoid the complications associated with tissue movement between imaging exams, which compromises the accuracy of postprocedure co-registration.

The application of NIR tomography to provide spatially-resolved functional information, such as hemoglobin levels, oxygen saturation, water, lipid and scatterer content will likely be important, yet customized imaging systems which couple to MRI, US or CT need to be developed to evaluate and exploit this potential. The pioneering work of Ntziachristos *et al.*¹³ was the first to demonstrate feasibility of the hybrid NIR-MR approach for clinical breast imaging. Their approach consisted of a co-planar array of optical source/sensors detecting time-resolved illuminations when applied to the surface of the breast. Data was presented as maps of localized optical response at each detector site but was otherwise not processed into depth-resolved images of optical property distributions. Zhu *et al.*¹¹ have demonstrated clinical application of a combined NIR-US system. With a handheld probe, they simultaneously measure reflection of ultrasound and modulated NIR excitations at the breast tissue surface, and construct co-registered images of structure and optical absorption and hemoglobin concentration.

One of the most challenging issues in hybrid system development is the incorporation of anatomical information as prior constraints into NIR image reconstruction. This has been explored theoretically in several successful reports.^{17–22} Structural information can be used to guide functional image reconstruction through knowledge of tissue composition and location by: (i) alteration of the objective functions used in image reconstruction,^{10,23} (ii) reduction of the number of unknown parameters by treating regions of the same tissue type as single zones,^{13,24} or (iii) introduction of special regularization schemes that can stabilize the inverse problem and emphasize image contrasts.^{10,25,26} Optimizing spatial resolution

more likely will depend on the application of all three techniques, while also being strongly influenced by the signal to noise ratio of the measurements, the optical contrast available, and the number of projections used. Some investigators have successfully combined different approaches with multi-stage image reconstruction algorithms.^{20,21} However, there is still no clear consensus on how best to utilize the structural information to enhance or improve the recovery of functional NIR information.

This work describes the first system to combine multi-spectral frequency-domain NIR in a planar tomographic geometry with MRI for imaging breast tissue. NIR tomography has shown the ability to localize changes in functional tissue parameters *in vivo*, and MRI has the advantage of offering a particularly rich amount of anatomical information, specifically about the layered adipose and glandular tissue structure of the breast. This system is designed to combine the benefits of both modalities into the construction of a single quantitative image. In particular, since NIR tomography has significant difficulty with the recovery of properties in layered structures, the initial information from MRI can significantly improve the estimation of breast properties, including in localized regions such as tumors.

The design and operation of the NIR-MRI system elements are described in Sec. II. The NIR component is similar to an imaging system described previously,²⁷ which is currently being evaluated clinically, yet has the unique design feature of having no moving parts in the detection channels, allowing significant reduction in the NIR data acquisition time. In Sec. III we outline the theoretical basis, and the practical application and utilization of image reconstruction in NIR tomography. After applying several approaches to optimizing this hybrid reconstruction, an algorithm is examined that takes advantage of the composite data set. In Sec. IV we discuss system performance and present images of phantom and breast optical properties which are both high resolution and quantitatively accurate.

II. SYSTEM DESIGN

This section describes the four elements that comprise the NIR-MRI system: (A) light delivery, (B) detector array, (C) fiberoptic patient interface, and (D) computer control and electronics. Element (C) extends from (A) and (B) into a MRI scanner for clinical studies, as shown schematically in Fig. 1. Photographs of the rack-mounted system and patient interface are presented in Fig. 2. Section (E) briefly describes phantom fabrication, and its importance in imaging system development and validation.

A. Light delivery

The system deploys six laser diodes: 661 nm (40 mW), 752 nm (50 mW), 785 nm (50 mW), 805 nm (50 mW), 829 nm (50 mW), and 849 nm (50 mW). Each wavelength is amplitude modulated at 100 MHz by mixing a dc current source (LDX-3220, ILX Lightwave, Bozeman, MT) and an ac current from a frequency generator (IFR-2023A, IFR Systems, Wilmington, MA), through a bias T (#5545, Picosecond Pulse Labs, Boulder, CO). Each diode is held in a laser

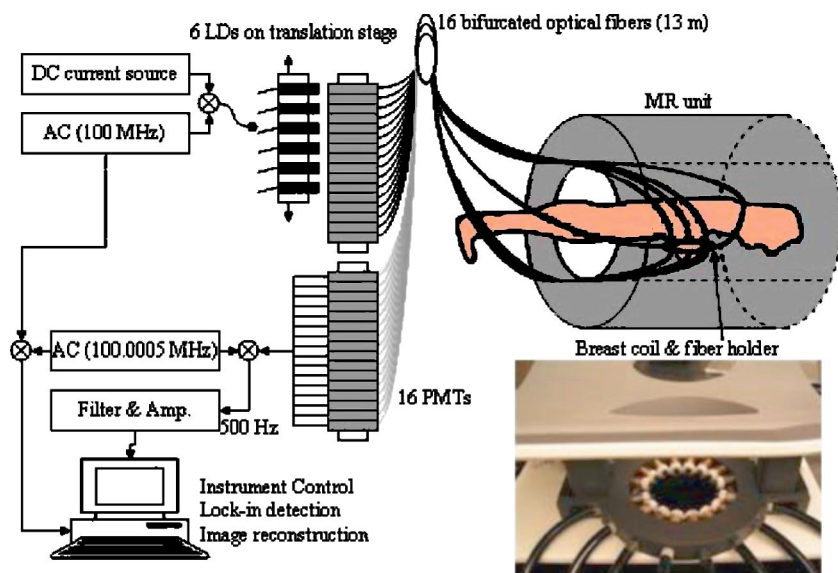


FIG. 1. (Color online) Schematic design of a dual modality NIR-MRI system (left). Frequency-domain NIR tomography is performed inside the MRI unit (upper right). Six laser diodes (660–850 nm) are amplitude modulated, and sixteen projections yield 240 measurements of amplitude and phase of transmitted light. The fiberoptic array is positioned inside the open breast coil, to allow positioning along the length of the pendant breast (bottom right).

tube (Thorlabs, Newton, NJ), and mounted on a linear translation stage (MA2515P5-S2.5 Velmex, Bloomfield, NY). This stage directs a specified wavelength into one of sixteen bifurcated optical fiber bundles which were custom designed for this application (Ceramoptec, East Longmeadow, MA). The 248-piece bundles (0.37 N.A., 0.68 packing fraction) are pure silica core (210 μm), silicone clad (230 μm) fibers suitable for transmission wavelengths from 400 nm to 2400 nm. The source light is delivered through the central seven fibers in each bundle, and the remaining fibers surrounding these are delivered to the detectors. The common end, which makes contact with the tissue, has a diameter of 4 mm. Each fiber bundle is 13 m in length and extends from the instrument cart, located outside of the MR suite, into the bore of the scanner (1.5T whole body imager, GE Medical Systems, Milwaukee, WI) to the patient interface. The efficiency of the optical switching is approximately 50%, yielding an average source power of 15 mW at the tissue surface.

B. Light detection

For each source excitation, light transmission is recorded from 15 surface locations. This signal is measured by 15

photomultiplier tubes (PMT R6357, Hamamatsu, Japan) operating in parallel. The gain of the PMTs is varied to account for the large variation in light level between detectors depending on their distance from the source. The gains are set with PMT modules (HC120, Hamamatsu) by applying computer generated voltages between 0.4 and 1.2 V to their control lines, which sets the anode to cathode voltage between approximately 350 V to 1000 V, respectively. Using the higher gain settings, a PMT can reliably measure optical signals in the pW range. The optimal gain levels are determined prior to each imaging series. Each PMT is fixed to a particular fiber, so it is necessary to switch gains electronically during the course of data collection. A 100 M Ω resistor was used in the dynode chain of each PMT to achieve fast settling times after gain adjustment (200 ms for large gain changes). Electrical heterodyning through rf mixers (Minicircuits, Brooklyn, NY) is used to down convert the 100 MHz PMT signal to a lower frequency (500 kHz). This offset frequency is achieved with a second frequency-synthesizer which is synchronized to the one driving the laser current, and is set to 100.0005 MHz. The resulting offset frequency is filtered and amplified by a 16 channel circuit designed for

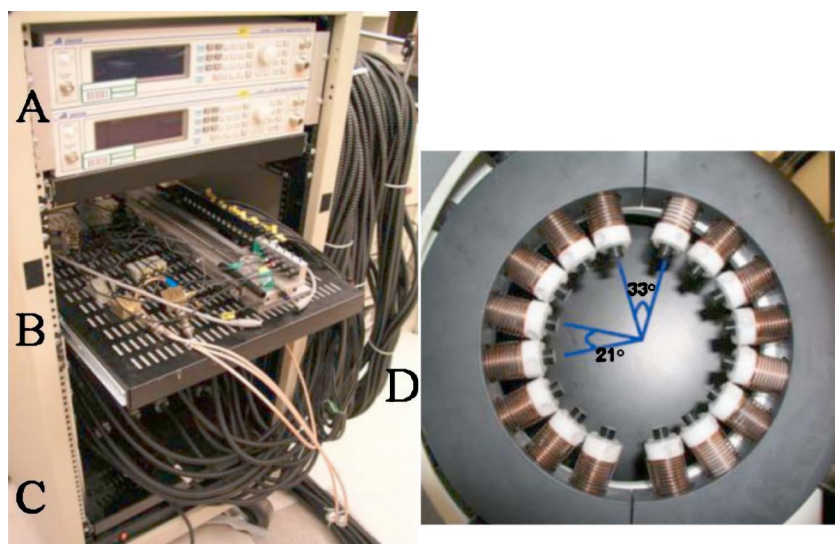


FIG. 2. (Color online) Photograph of the rack mounted, portable system (left). System components are marked, including (A) frequency generators, (B) optical switching stage, (C) PMT detection plate, and (D) optical fibers and patient interface. The fiber-patient interface (at right) can accommodate breasts 6–12 cm in diameter. A close up of the tissue coupling system shows that the fibers are spring-loaded and make light contact with the full circumference of a pendant breast.

this application (Audon Electronics, Nottingham, UK), then read by the computer. Lock-in detection is executed in software to extract amplitude and phase data for each of the detectors in parallel.

C. Fiberoptic patient interface

The MR exam is performed using a breast array coil (MRI Devices, Waukesha, WI) that offers high-resolution imaging. The coil also provides an open architecture, which allows for the integration of the NIR-breast interface shown in Fig. 1. A circular ring machined from polyvinyl chloride (PVC) positions the common ends of the sixteen fibers around the full circumference of the pendant breast. Phosphor bronze compression springs ($k=0.09$ lbs/in., Ace Wire Spring and Form, McKees Rocks, PA) guide each fiber through holes in the ring, into light contact with the tissue surface. The ring separates into equal halves so that it can easily be moved from one breast to the other. The angular separation between each fiber is 21° , except between fibers adjacent to the line of ring deviation, where the separation is 33° . The ring can be positioned vertically, such that the plane of measurements intersects the region of interest in tissue. This design allows each fiber to move independently, therefore their radial positions may vary by several millimeters. In order to avoid serious artifacts in reconstructed images, the position of each fiber must be accurately known during data acquisition. Annular fiducial markers (MM 3005, IZI Medical Products, Baltimore, MD) are fixed to each fiber and can be located with submillimeter accuracy in the MRI.

D. Computer system

A PC running Labview software (National Instruments, Austin, TX) is used to control all light delivery and detection equipment. The laser current source and frequency generator parameters are set by a general purpose interface bus (GPIB, NI). The linear translation stage is addressed through the serial port. An analog output board (NI) is used for PMT gain control. A multipurpose data acquisition (DAQ) board acquires the 16 analog input channels and the single reference channel. This board also provides six digital output lines to the high power radio-frequency switch for the laser sources. For each source position, 15 signals from the detector system are amplified by a gain of 1000 and low pass filtered to prevent aliasing prior to the DAQ board using a 16 channel amplifier and filter network mounted in a BNC coupled box (Audon Electronics, Nottingham, UK). Data are acquired for 500 ms, and phase and amplitude of each signal are calculated and written to file. Including the time required to determine optimal gain values, measurement with 6 wavelengths takes approximately 4 min. The MR exam is controlled separately, operated in parallel, and a full volume breast MRI is of similar duration. A FORTRAN, or MATLAB based reconstruction program reads and processes the NIR data.^{28–30} MR images are processed off-line with an addition to the MATLAB software package, and incorporated into a modified iterative optical property reconstruction (see Sec. III).

E. Phantom design

Tissue-simulating phantoms with known property distributions, geometries, and imaging orientations are commonly used to validate imaging systems. We have developed a recipe for producing gelatin materials with desired optical properties, and a shelf life of several months.³¹ A heated mixture of water, gelatin (G2625, Sigma Inc.), India ink (for absorption), and titanium dioxide powder (for scatter) (TiO_2 , Sigma Inc.) is poured into a mold of a desired shape, and solidified by cooling to room temperature. Variation in the water concentration provides MR contrast, and variable gel stiffness. The phantom imaged here (Sec. IV B) combines three gels with different optical properties in an irregular structure.

III. DATA PROCESSING AND IMAGE RECONSTRUCTION

Quantitative NIR imaging with model-based methods requires (A) important instrument calibration procedures, and (B) a reconstruction algorithm that incorporates an accurate model of light propagation in tissue.

A. System calibration

Calibration issues and other practical considerations associated with our NIR imaging approach have been discussed in detail elsewhere.²⁹ Two important procedures are briefly noted here: (1) detector calibration, and (2) homogeneous phantom calibration. First, the amplitude and phase response of each detection channel must be characterized in order to remove systematic noise in the data acquisition hardware. Each detector is exposed to the same optical signal, and the differences in log amplitude and phase are used as correction factors. The log amplitude response of the PMT is plotted against the log of the input power for each gain setting. A log-log regression is performed and the coefficients are used to calibrate detected PMT amplitude in terms of optical power. The phase does not fluctuate significantly with changing light level for a single gain setting (i.e., minimal phase-amplitude cross-talk), but is altered dramatically with changing gain. Relative phase differences between detectors are stored for calibration. These calibration curves are very similar to those created by McBride *et al.*²⁷ This characterization needs to be performed only once as long as the system is not modified.

The second important practical procedure is the correction for inter fiber variations and coupling issues, which is accomplished through a homogeneous phantom calibration process.^{29,32} This accounts for offsets due to optical fiber differences in transmission and alignment, as well as any errors in discretization or data-model mismatch. A homogeneous phantom is generally measured each day, and after system changes. The differences between data measured from the phantom, and data calculated from the model are stored and subtracted from measurements of the heterogeneous phantom or tissue under investigation. A homogeneous fitting algorithm is used to determine the μ_a and μ_s' values supplied to the model calculation. This algorithm can also be used to calculate the initial optical properties specified in

iterative reconstruction of heterogeneous media. When dealing with tissues having arbitrary shape, the effectiveness of this fitting algorithm and homogeneous phantom calibration hinges on the accurate specification of source and detector locations. The ability to extract accurate fiber positions from MRI scans preserves the integrity of this method for nonuniform boundary data.

B. FEM analysis

Data acquired from the detection system is processed by a FEM based reconstruction algorithm to generate tomographic images of absorption and reduced scattering coefficients simultaneously. The algorithm exploits the frequency-domain diffusion equation approximation to light behavior in a highly scattering medium,²⁸

$$-\nabla \cdot D(\mathbf{r}) \nabla \Phi(\mathbf{r}, \omega) + \left(\mu_a(r) + \frac{i\omega}{c} \right) \Phi(\mathbf{r}, \omega) = S(r, \omega), \quad (1)$$

where $S(r, \omega)$ is an isotropic light source at position r , $\Phi(r, \omega)$ is photon density at r , c is the speed of light in tissue, ω is the frequency of light modulation, μ_a is the absorption coefficient, and $D = 1/[3(\mu_a + \mu'_s)]$ is the diffusion coefficient. The reduced (transport) scattering coefficient is given by $\mu'_s = \mu_s(1-g)$, where g is the mean cosine of the single scatter function (the anisotropy factor), and μ_s is the scattering coefficient.

For a given μ_a and μ'_s distribution, the diffusion equation is used to predict the optical flux at the detector sites for each source excitation. In the inverse problem (image reconstruction), the goal is the estimation of optical properties at each FEM node, based on measurements of optical flux at the detector sites on the tissue surface. This is achieved numerically by minimizing the difference between the calculated data Φ^C , and measured data, Φ^M , for all source/detector combinations (NM). Typically,

$$\chi^2 = \sum_{i=1}^{NM} (\Phi_i^C - \Phi_i^M)^2 \quad (2)$$

is minimized in a least squares sense by setting the first derivative equal to zero, and using a Newton–Raphson approach to find the set of optical property values which approximate the point of stationarity. We use a Levenberg Marquardt algorithm, and repeatedly solve the equation

$$a = (J^T J + \lambda I)^{-1} J^T b, \quad (3)$$

where $b = (\Phi^C - \Phi^M)^T$ is our data vector, and a is the solution update vector, $a = [\delta D_j; \delta \mu_{a,j}]$, defining the difference between the true and estimated optical properties at each reconstructed node j . Here, λ is a regularization factor to stabilize matrix inversion and J is the Jacobian matrix for our model, which is calculated using the Adjoint method.³³

Improving NIR reconstructions by incorporating MRI data has been explored in previous work,^{22,23} and by other authors.^{13,21,24} Techniques used to produce the images shown in Sec. IV include: (i) accurately defining the imaging volume, (ii) tailoring a regularization scheme which optimizes the reconstructed contrast of a suspicious area in the image,

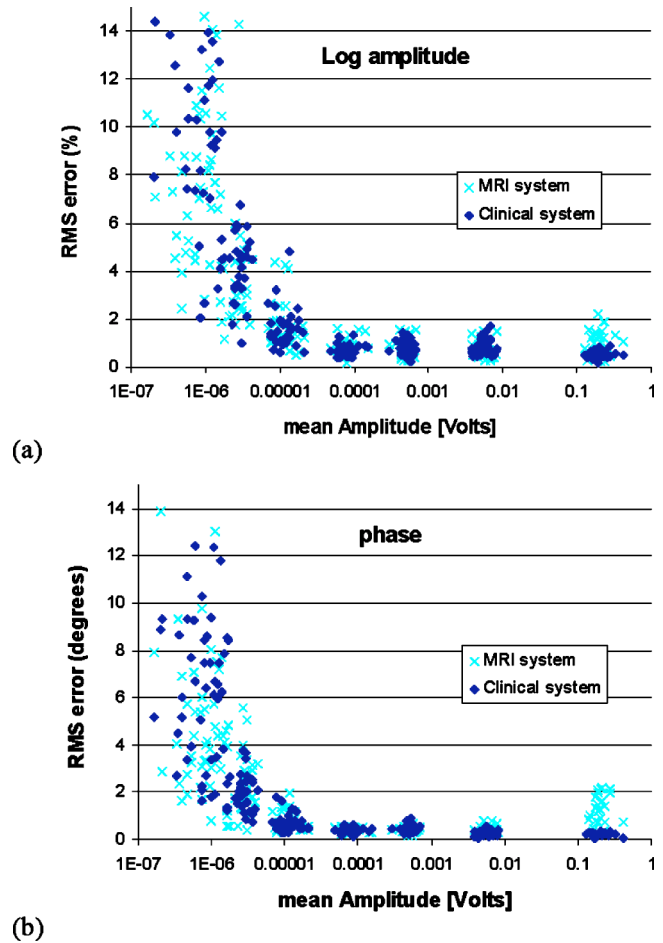


FIG. 3. (Color online) Repeatability assessment for (a) log amplitude and (b) phase of NIR component of combined NIR-MRI system and stand-alone NIR tomography system at Dartmouth. The performance of the two systems is comparable. In routine operation, PMT voltage signals are above 1.0×10^{-5} V.

and (iii) reducing the number of unknown parameters by segmenting tissue types visible in the MRI. Defining the imaging volume, (i), is relatively straight forward and can be accomplished by creating a structured finite element mesh from the MRI. This mesh will often contain regional differences depending on tissue types present, and an irregular outer boundary due to impressions caused by fiber-tissue contact. In simulation studies, not presented here, it has been found that image reconstruction accuracy is easily degraded if the mesh (2D or 3D) does not represent the true outer tissue boundary. Step (ii) can be accomplished by changing λI in Eq. (3) to λA , where A is a regularization matrix, or filter matrix. Regularization can be thought of as a smoothing operator, where one can apply selective smoothing by linking together the property updates for all nodes associated with the same region or tissue type. Modifications to the Jacobian matrix size in a parameter reduction technique are used to implement step (iii).²³

IV. PERFORMANCE AND EXPERIMENTAL RESULTS

In this section we (A) compare measurements from this system to those from a similar NIR tomography instrument

TABLE I. Optical properties at 785 nm for 15 tissue simulating phantoms, and % differences from values determined using another NIR tomography system.

| | $\mu_a(\text{mm}^{-1})$ (NIR-MRI) | % difference | $\mu'_s(\text{mm}^{-1})$ (NIR-MRI) | % difference |
|-----------|--------------------------------------|--------------|---------------------------------------|--------------|
| Mean | 0.0055 | -6.2 | 1.34 | 9.1 |
| Max | 0.0102 | -23.4 | 1.91 | 29.6 |
| Std. Dev. | 0.0024 | 8.7 | 0.41 | 7.9 |

described previously²⁷ for a number of tissue simulating phantoms. NIR-MRI phantom studies are described in (B), and *in vivo* images are shown in (C). For all results presented here, we used a single laser diode (785 nm) for convenience, and 2D modeling and image reconstruction. System performance and image quality at the other five wavelengths are comparable, and 3D imaging is readily achievable.

A. System performance

Measurement repeatability in terms of phase and log amplitude error was assessed by serially imaging a phantom with optical properties similar to those of average breast tissue ($\mu_a=0.004$, $\mu'_s=1.35$). The average rms error at each detector site was determined to be 0.26% in ac intensity and 1.04° in phase. These values compare with those obtained from the system described by McBride *et al.* (0.32% in ac intensity and 0.48° in phase).²⁷ rms error for each of the 240 source-detector combinations for both systems is plotted versus the PMT signal in Fig. 3. For both phase and amplitude, error sharply increases when incident light falls below approximately 0.5 pW. These points are excluded in the calculation of average rms error. As an additional comparison, we used both devices to measure a collection of homogeneous phantoms ($N=15$) of varying diameters (73–91 mm) and optical properties ($\mu_a=0.0023$ –0.0102 mm⁻¹, $\mu'_s=0.33$ –1.91 mm⁻¹). After processing the measurements with the calibration procedure described in Sec. III, we used the homogeneous fitting algorithm to determine a single μ_a and μ'_s for each material. Table I shows the optical coefficients obtained with the NIR-MRI system, along with a measure of their discrepancy with those obtained with our stand-alone DOT instrumentation. We observed good agreement between

TABLE II. Approximate optical properties of gelatin phantom.

| | Outer layer | Inner layer | Inclusion |
|--------------------------|-------------|-------------|-----------|
| $\mu_a(\text{mm}^{-1})$ | 0.0044 | 0.0062 | 0.02 |
| $\mu'_s(\text{mm}^{-1})$ | 0.51 | 0.68 | 0.9 |

the two systems, consistent throughout the range of phantom properties. The absorption and scattering coefficients show correlation coefficients of $R^2=0.984$ and $R^2=0.980$, respectively.

B. Phantom imaging

Due to the limited spatial resolution of DOT, layered media, small objects, and low contrast heterogeneity pose key challenges in image reconstruction. The capability of the presented system to address these challenges was investigated by imaging a phantom comprised of three gels with different optical properties. The phantom is cylindrical and the boundary between the outer layer and inner layer is irregular. A two centimeter spherical inclusion is embedded within the inner layer. The optical coefficients of each gel are known (Table II), as each material was created using a practiced recipe to give desired values. Furthermore, the true value of each layer was validated by creating a separate homogeneous phantom for each layer (at the same time as creating layered phantom) and measuring bulk properties with a homogeneous fitting algorithm. To increase MRI contrast between layers, OmniscanTM (gadodiamide) was added to the inner layer (0.005 g/ml).

A photograph of the phantom, alongside another spherical inclusion is shown in Fig. 4(a). Figure 4(b) shows a T1-weighted, gradient echo MRI (25 ms TR, 3 ms TE, 45° flip angle) crosssection of the phantom in the plane of the optical fibers. This was used to create a 2D structured finite element mesh and to locate the positions of the 16 fibers [Fig. 4(c)]. Fiber fiducials were not used in this experiment, but the 16 impressions caused by each optical fiber are clearly visible around the perimeter of the gel. Each of the three regions are also visible, corresponding to each of the three types of optically variant gel. 3D meshing and imaging is also possible, given that a stack of MR slices represent the full volume

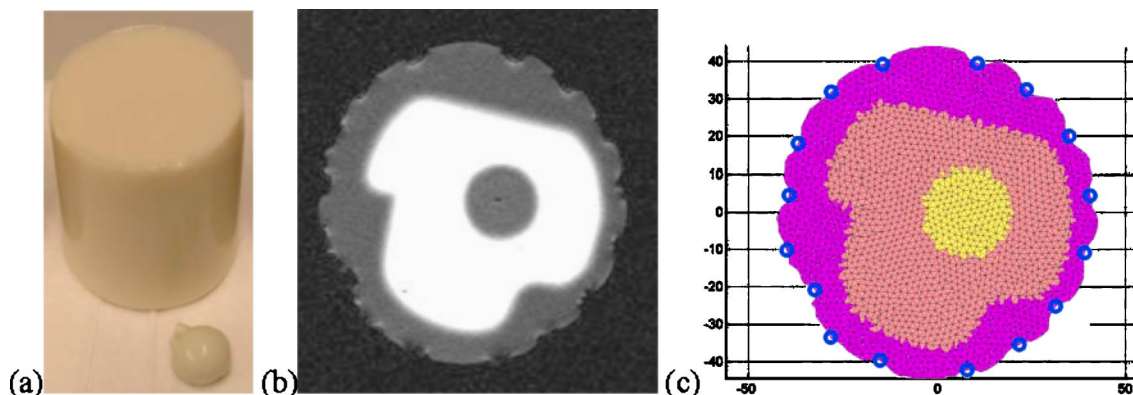


FIG. 4. (Color online) (a) The gelatin phantom. (b) T1-weighted MRI image of the structure of the phantom cross section. The inner layer (light region) contains gadodiamide for MR contrast (0.005 g/ml). The inner inclusion is a 2 cm diameter sphere. (c) Finite element mesh derived from the three-layered structure image in (b). The circles on the outer boundary indicate the fiber locations. Axes are in millimeters.

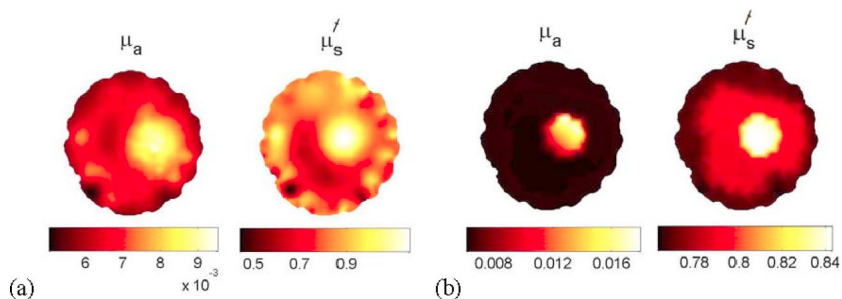


FIG. 5. (Color online) Images in (a) show absorption coefficient (left) and reduced scattering coefficient (right) reconstructions without MRI guidance. In (b), reconstructions improve when the interior structural information of the MRI is incorporated. Comparing these two images, the latter has a reduction in artifacts in the reduced scattering coefficient image, and both the spatial resolution and contrast have improved. The recovered values compare favorably with the approximate true values shown in Table II.

structure of the phantom. The system design allows for NIR data acquisition in multiple planes if desired.

Using log amplitude and phase data, images of optical properties were reconstructed with two different algorithms. The first algorithm solves Eq. (3) without *a priori* guidance, except for the use of the mesh and source locations from Fig. 4(c). The corresponding reconstructed images are presented in Fig. 5(a). The second algorithm uses the layered structure from the MRI to constrain Eq. (3). The regularization parameter associated with each reconstructed node is adjusted based upon its location and area of influence. Lower values are used for small regions close to the center of the reconstructed volume, whereas peripheral regions (which are prone to large artifacts) have larger regularization. A regularization matrix (A), or filter matrix, based upon the *a priori* structural information from the MRI was also used to further improve the algorithm. The optimal values for λ and A were determined in simulation studies of this geometry, using similar contrast and noise levels. These can also be chosen automatically once an empirical knowledge of their effect is established. The images reconstructed from this modified constrained algorithm are shown in Fig. 5(b).

Qualitatively, the algorithm that uses MRI information to guide the iterative process performs much better. The optical property images in Fig. 5(a) are blurry and “edge artifacts” are clearly visible, especially for μ'_s . The absorbing sphere near the center of the phantom is recovered with poor spatial resolution, and its contrast is underestimated. The property maps in Fig. 5(b) have improved resolution. Spatial resolution and contrast of the spherical inclusion are better. As a quantitative measure of the accuracy of image reconstruction, we compute the rms error between the target image and the reconstructions, node by node. This measure indicates a dramatic improvement for the second method [$\text{rms}(\mu_a)$

$=0.0024$, $\text{rms}(\mu'_s)=0.19$] relative to the first [$\text{rms}(\mu_a)$
 $=0.0034$, $\text{rms}(\mu'_s)=0.25$].

C. In vivo imaging

The Institutional Review Board (IRB) at the Dartmouth Hitchcock Medical Center approved this clinical examination protocol, and written informed consent was obtained from all volunteering women. Figures 6(a) and 6(b) show a photograph of a subject lying on the examination platform, and an anatomical axial MR image through the breast. NIR measurements (4 wavelengths in this case) and a full volume MRI (50 coronal slices, 25 ms TR, 6 ms TE, 45° flip angle, 2 mm slice thickness) were obtained in less than 10 min. Fig. 7(a) shows an anatomically coronal MRI with 16 fiducial-marked fibers (appearing as bright white spots outside the breast). The radiographic density of this participant is heterogeneously dense (HD), and a large interior region of glandular tissue is easily defined in the FEM mesh shown in Fig. 7(b).

As with the phantom study, we present images of μ_a and μ'_s at 785 nm reconstructed with two different algorithms. The first result, obtained by solving Eq. (3), without *a priori* guidance, is shown in Fig. 7(c). As expected, we see higher absorption and scatter in the glandular region (central) relative to the adipose tissue (peripheral). However, the region of increase does not span the full area expected, and heterogeneity is visible (especially around the perimeter of the image). The second algorithm assumes homogeneous optical properties for each tissue type, and utilizes parameter reduction,²³ which leads to a “fitting” for four values: $\mu_a \text{ adipose}=0.003$, $\mu'_s \text{ adipose}=0.93$, $\mu_a \text{ glandular}=0.006$, $\mu'_s \text{ glandular}=1.12$ [Fig. 7(d)]. This algorithm is robust to noise and converges after a few iterations. The result is quantita-

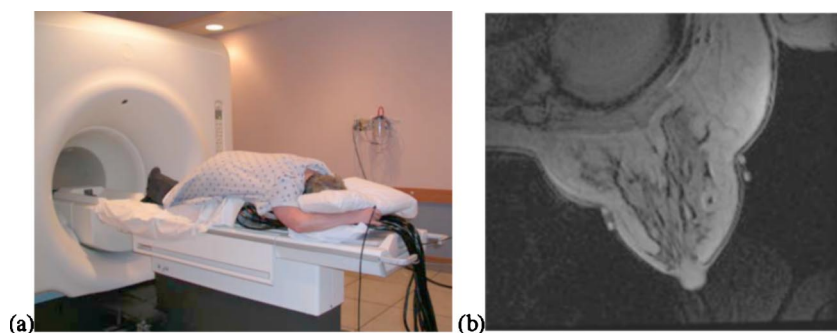


FIG. 6. (Color online) Photograph in (a) shows a female volunteer prepared for the simultaneous MRI-NIR exam. In an anatomical axial T1-weighted MRI slice from the right breast, (b), fiducial markers (outside the breast) indicate the location of the fiber plane.

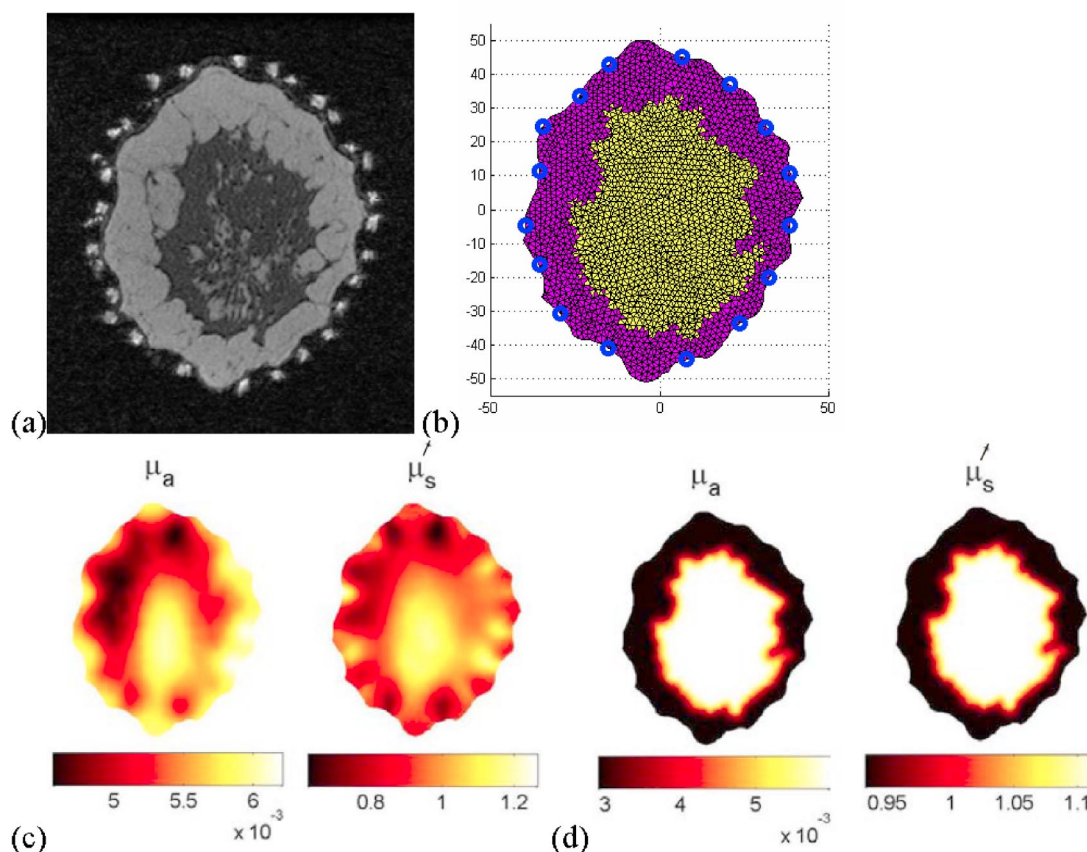


FIG. 7. (Color online) In (a), an anatomically coronal T1-weighted MRI displays adipose (outer) and glandular (inner) tissue types. A two layer structured FEM mesh and source locations, created from (a), is shown in (b). Absorption and reduced scattering coefficient (mm^{-1}) reconstructions in (c) are obtained without utilizing the internal structure of (b). In (d), MRI data guides a two-region parameter fitting algorithm. Relative to (c), resolution has improved and contrast has increased—showing higher absorption and scatter in glandular relative to adipose tissue.

tively logical, and similar values are recovered using spatially varying regularization (as described in the phantom reconstruction).

V. DISCUSSION

This article describes a novel *in vivo* breast imaging system that synergistically combines NIR tomography with MRI. Tissue structures visible with high resolution in MRI can be applied *a priori* to optical property reconstructions from frequency-domain NIR measurements. Thus, the reconstruction process can be optimized to produce high resolution, quantitatively accurate maps of absorption and reduced scattering coefficients, and ultimately physiologically relevant parameters. Various physiological tissue types exhibit significant contrast in the NIR, primarily though, the combined system could be very effective at locating and diagnosing breast tumors.

The NIR component provides multispectral (6 wavelengths) frequency-domain (log amplitude and phase) data from 16 fiber-tissue contact positions around the breast's circumference. Data acquisition is fully automated, and a complete set of measurements (240 source-detector pairs) for one wavelength requires approximately 40 s. Light detection is highly sensitive (subpicowatt limit) with low noise (rms $<0.26\%$, $<1.04^\circ$ in phase). All optical elements and controls are mounted in a portable cart, and operation inside strong

magnetic fields is facilitated with long optical fibers and an easy-to-use positioning system/patient interface.

The deployment of dual modality NIR imaging systems in clinical applications has been limited to date, mainly because of the complexity of the image reconstruction problem. Here, a representative phantom and *in vivo* study using one wavelength (785 nm) are presented. We have shown that co-registered MRI validates and improves optical property estimation in 2D tomographic image reconstructions when specialized algorithms are used. Future work will involve 3D modeling and reconstruction, which could further improve both qualitative and quantitative aspects of the recovered coefficient values.

Preliminary results are encouraging, and have allowed us to optimize reconstruction techniques, and automate constraint selection. We have performed several phantom studies, and demonstrated the feasibility of imaging volunteers with healthy breasts. Through the study of more healthy subjects, with different radiographic densities, we aim to compare functional parameters of adipose versus glandular tissue. To test the system's ability at diagnosing tumors, cancer patients will be recruited, and the simultaneous exam will likely involve MR contrast enhancement.

ACKNOWLEDGMENTS

The authors would like to express sincere gratitude to Gordon Ehret and Richard Johnson for their fine fabrication

work. This work has been sponsored by the National Cancer Institute through Grants Nos. RO1CA78734, PO1CA80139, and DAMD17-03-1-0404.

- ¹V. Ntziachristos, A. H. Hielscher, A. G. Yodh, and B. Chance, *IEEE Trans. Med. Imaging* **20**, 470 (2001).
- ²B. W. Pogue, S. P. Poplack, T. O. McBride, W. A. Wells, O. K. S. Osterman, U. L. Osterberg, and K. D. Paulsen, *Radiology* **218**, 261 (2001).
- ³S. Srinivasan, B. W. Pogue, S. Jiang, H. Dehghani, C. Kogel, S. Soho, J. J. Gibson, T. D. Tosteson, S. P. Poplack, and K. D. Paulsen, *Proc. Natl. Acad. Sci. U.S.A.* **100**, 12349 (2003).
- ⁴B. J. Tromberg, N. Shah, R. Lanning, A. Cerussi, J. Espinoza, T. Pham, L. Svaasand, and J. Butler, *Neoplasia* **2**, 26 (2000).
- ⁵S. R. Arridge, *Inverse Probl.* **15**, R41 (1999).
- ⁶H. Dehghani, B. W. Pogue, S. Jiang, B. A. Brooksby, and K. D. Paulsen, *Appl. Opt.* **42**, 3117 (2003).
- ⁷V. Chernomordik, A. H. Gandjbakhche, M. Lepore, R. Esposito, and I. Delfino, *J. Biomed. Opt.* **6**, 441 (2001).
- ⁸D. A. Boas, K. Chen, D. Grebert, and M. A. Francheschini, *Opt. Lett.* **29**, 1506 (2004).
- ⁹B. W. Pogue, S. Jiang, H. Dehghani, C. Kogel, S. Soho, S. Srinivasan, X. Song, T. D. Tosteson, S. P. Poplack, and K. D. Paulsen, *J. Biomed. Opt.* **9**, 541 (2004).
- ¹⁰A. Li, E. L. Miller, M. E. Kilmer, T. J. Brukilaccio, T. Chaves, J. Stott, Q. Zhang, T. Wu, M. Choriton, R. H. Moore, D. B. Kopans, and D. A. Boas, *Appl. Opt.* **42**, 5181 (2003).
- ¹¹Q. Zhu, N. G. Chen, and S. H. Kurtzman, *Opt. Lett.* **28**, 337 (2003).
- ¹²B. W. Pogue, H. Zhu, C. Nwaigwe, T. O. McBride, U. L. Osterberg, K. D. Paulsen, and J. F. Dunn, *Oxygen Transport to Tissue*, Vol. XXIV, p. 215 (2002).
- ¹³V. Ntziachristos, A. G. Yodh, M. D. Schnall, and B. Chance, *Neoplasia* **4**, 347 (2002).
- ¹⁴G. Gulsen, H. Yu, J. Wang, O. Nalciglu, S. Merritt, F. Bevilacqua, A. J. Durkin, D. J. Cuccia, R. Lanning, and B. J. Tromberg, *Technol. Cancer Res. Treat.* **1**, 1 (2002).
- ¹⁵K. D. Paulsen and H. Jiang, *Med. Phys.* **22**, 691 (1995).
- ¹⁶M. Tatsumi, C. Cohade, Y. Nakamoto, and R. L. Wahl, *Radiology* **229**, 831 (2003).
- ¹⁷R. L. Barbour, H. L. Graber, J. Chang, S. S. Barbour, P. C. Koo, and R. Aronson, *IEEE Comput. Sci. Eng.* **2**, 63 (1995).
- ¹⁸A. H. Barnett, J. P. Culver, A. G. Sorensen, A. Dale, and D. A. Boas, *Appl. Opt.* **42**, 3095 (2003).
- ¹⁹V. Ntziachristos, X. H. Ma, and B. Chance, *Rev. Sci. Instrum.* **69**, 4221 (1998).
- ²⁰M. Torregrossa, C. V. Zint, and P. Poulet, *Opt. Tomography and Spectroscopy of Tissue V* (2003).
- ²¹M. Schweiger and S. R. Arridge, *Phys. Med. Biol.* **44**, 2703 (1999).
- ²²B. W. Pogue, T. O. McBride, C. Nwaigwe, U. L. Osterberg, J. F. Dunn, and K. D. Paulsen, *Proc. SPIE* **3597**, 484 (1999).
- ²³B. A. Brooksby, H. Dehghani, B. W. Pogue, and K. D. Paulsen, *IEEE J. Sel. Top. Quantum Electron.* **9**, 199 (2003).
- ²⁴N. G. Chen, P. Guo, S. Yan, D. Piao, and Q. Zhu, *Appl. Opt.* **40**, 6367 (2001).
- ²⁵B. W. Pogue, T. O. McBride, J. Prewitt, U. L. Osterberg, and K. D. Paulsen, *Appl. Opt.* **38**, 2950 (1999).
- ²⁶M. Belge, M. E. Kilmer, and E. L. Miller, *Inverse Probl.* **18**, 1161 (2002).
- ²⁷T. O. McBride, B. W. Pogue, S. Jiang, U. L. Osterberg, and K. D. Paulsen, *Rev. Sci. Instrum.* **72**, 1817 (2001).
- ²⁸H. Dehghani, B. W. Pogue, S. P. Poplack, and K. D. Paulsen, *Appl. Opt.* **42**, 135 (2003).
- ²⁹T. O. McBride, B. W. Pogue, U. L. Osterberg, and K. D. Paulsen, *Oxygen Transport to Tissue* Vol. XXIV, p. 85 (2002).
- ³⁰B. W. Pogue, S. Geimer, T. O. McBride, S. Jiang, U. L. Osterberg, and K. D. Paulsen, *Appl. Opt.* **40**, 588 (2001).
- ³¹D. Li, P. M. Meaney, T. D. Tosteson, S. Jiang, T. Kerner, T. O. McBride, B. W. Pogue, A. Hartov, and K. D. Paulsen, *Med. Phys.* **30**, 2194 (2003).
- ³²S. Jiang, B. W. Pogue, T. O. McBride, M. M. Doyley, S. P. Poplack, and K. D. Paulsen, *J. Electron. Imaging* **12**, 613 (2003).
- ³³S. R. Arridge and M. Schweiger, *Appl. Opt.* **34**, 8026 (1995).

Effects of refractive index on near-infrared tomography of the breast

Hamid Dehghani, Ben A. Brooksby, Brian W. Pogue, and Keith D. Paulsen

Near infrared (NIR) optical tomography is an imaging technique in which internal images of optical properties are reconstructed with the boundary measurements of light propagation through the medium. Recent advances in instrumentation and theory have led to the use of this method for the detection and characterization of tumors within the female breast tissue. Most image reconstruction approaches have used the diffusion approximation and have assumed that the refractive index of the breast is constant, with a bulk value of approximately 1.4. We have applied a previously reported modified diffusion approximation, in which the refractive index for different tissues can be modeled. The model was used to generate NIR data from a realistic breast geometry containing a localized anomaly. Using this simulated data, we have reconstructed optical images, both with and without correct knowledge of the refractive-index distribution to show that the modified diffusion approximation can accurately recover the anomaly given *a priori* knowledge of refractive index. But using a reconstruction algorithm without the use of correct *a priori* information regarding the refractive-index distribution is shown as recovering the anomaly but with a degraded quality, depending on the degree of refractive index mismatch. The results suggest that provided the refractive index of breast tissue is approximately 1.3–1.4, their exclusion will have minimal effect on the reconstructed images. © 2005 Optical Society of America

OCIS codes: 170.3010, 170.3830, 170.6960.

1. Introduction

Near-infrared (NIR) optical tomography, is a noninvasive imaging modality in which images of internal optical properties are reconstructed by use of measured transmission data.^{1–8} More specifically, a number of optical fibers are placed around the surface of the tissue to be imaged and light is transmitted from one fiber at a time, while all other fibers are used to measure the exiting light at discrete locations around the tissue. The recovery of the interior optical properties is treated as a nonlinear inverse problem based on measurements at the exterior of the domain to be imaged. The light source can be operated in continuous-wave (cw) pulsed or intensity-modulated modes, giving rise to output measurements of light intensity, temporal point-spread function, or phase and amplitude, depending on the strategy adopted.

Typically light sources are applied at a number of NIR wavelengths, each, in turn, giving rise to additional spectrally independent boundary measurements. The time-resolved or frequency-domain data allows for reconstruction of internal optical property distributions of absorption (μ_a) and/or reduced scatter (μ_s') for each wavelength, which can in turn be used to calculate images of the concentrations of the dominant chromophores, including oxyhemoglobin, deoxyhemoglobin and water, as well as scattering power and amplitude.⁹ These images are the end results of NIR tomography, and they may complement other imaging modalities, potentially defining NIR tomography as a functional imaging technique.

For image reconstruction with the measured boundary data, several different algorithms can be used, depending on datatype, number of measurements, and domain under investigation.¹⁰ Many imaging algorithms rely on a numerical model, whereby the process for iteratively updating the internal distribution of absorption and scatter is to match the measured data to model-based predictions. Assuming that the tissue scatter dominates absorption and that the imaging domain is large enough so that the smallest source–detector fiber distance is greater than a few mean scattering lengths, the diffusion approximation (DA) models the light propagation effectively.

The authors are with the Thayer School of Engineering, Dartmouth College, 8000 Cummings Hall, Hanover, New Hampshire 03755-8000. H. Dehghani's e-mail address is hamid.dehghani@dartmouth.edu.

Received 26 July 2004; revised manuscript received 9 November 2004; accepted 17 November 2004.

0003-6935/05/101870-09\$15.00/0

© 2005 Optical Society of America

Recently, advances have been made in representing bulk internal refractive-index (RI) variation in tissue within the numerical model.^{11–13} Jiang and Xu¹² have used a higher-order DA that also takes into account the RI as a spatially varying property and have presented reconstructed images of internal absorption, reduced scatter, and refractive index using cw data. Our earlier study showed the implementation of RI spatial variation within the DA using a finite-element modeling approach.¹¹ Specifically, we defined an internal boundary condition that allows for discontinuous internal variations of RI between regions of contrast (or slowly varying) optical properties. This approach provided a good match between three-dimensional finite-element model results and Monte Carlo simulations, as well as controlled experimental measurements,¹⁴ suggesting that the technique is a valid approximation.

The absolute values of RI for breast tissue types are still a subject under investigation. Estimates are difficult to obtain accurately *in vivo*, but some data have been reported for various tissue types.^{14,15} Although adipose tissue (fatty layer) has been measured to be 1.455, to the best of our knowledge no results exist for fibroglandular tissue. Nonetheless, the RI of glandular tissue is believed to be lower than that of adipose (e.g., values of 1.4 have been assumed^{15,16}). The rationale for a lower value is sound in that estimates of the composition of fibroglandular tissue place its water (typically greater than 60%) and blood content (greater than 1%) to be high, indicating that its bulk RI is likely close to that of water.^{17,18}

In this paper, we have investigated at the effect of variation of RI within a realistic two-dimensional model of a female breast, by assuming distinct values for the adipose and glandular tissue compartments. Using our current dual modality magnetic resonance imaging (MRI)-NIR system, we can collect NIR and MRI data simultaneously¹⁹ allowing accurate *a priori* information regarding the tissue structure under investigation. Specifically, we have generated NIR data from a two-dimensional model of the female breast, obtained from MRI, within which we have assumed RI variation for the two main types, namely, adipose and glandular tissue. Within the glandular layer, we have inserted an abnormality with absorption and scatter-only contrast. Using the modeled NIR data perturbed by noise, we have reconstructed images of internal absorption and reduced scatter and have shown the effect on RI variation within reconstructed images for the cases of either no *a priori* or exact information on the RI values.

2. Theory

A. Forward Model

It is generally accepted that if the magnitude of the isotropic fluence rate within tissue is significantly larger than the directional flux magnitude, the light field is diffuse, which occurs when the scattering interaction dominates over absorption in a region of interest. Mathematically, this assumption allows a

simplification of the Boltzmann transport equation, by converting the description of an anisotropic light field into a diffusion equation approximation. The diffusion approximation in the frequency domain is given by

$$-\nabla \cdot \kappa(r) \nabla \Phi(r, \omega) + \left[\mu_a(r) + \frac{i\omega}{c_m(r)} \right] \times \Phi(r, \omega) = q_0(r, \omega), \quad (1)$$

where μ_a and μ_s' are absorption and reduced scattering, respectively; $q_0(r, \omega)$ is an isotropic source; $\Phi(r, \omega)$ is the photon fluence rate at position \mathbf{r} ;

$$\kappa = \frac{1}{3(\mu_a + \mu_s')}$$

is the diffusion coefficient; and $c_m(r)$ is the speed of light in the medium at any point, defined by $c/n(r)$, where $n(r)$ is the index of refraction at the same point and c is the speed of light in a vacuum.

The best description of the air-tissue boundary, is reported through an index-mismatched type III condition, in which the fluence at the edge of the tissue exits and does not return.²⁰ The flux leaving the external boundary is equal to the fluence rate at the boundary weighted by a factor that accounts for the internal reflection of light back into the tissue. This relation is described in

$$\Phi(\xi, \omega) + 2A\hat{\mathbf{n}} \cdot \kappa(\xi) \nabla \Phi(\xi, \omega) = 0, \quad (2)$$

where ξ is a point on the external boundary ($\partial\Omega_1$), and A depends on the relative RI mismatch between tissue Ω_1 and air. A can be derived from Fresnel's law,

$$A = \frac{2/(1 - R_0) - 1 + |\cos \theta_c|^3}{1 - |\cos \theta_c|^3}, \quad (3)$$

where $\theta_c = \arcsin(n_{\text{AIR}}/n_1)$, the angle at which total internal reflection occurs for photons moving from region Ω_1 with RI n_1 to air with RI n_{AIR} , and

$$R_0 = \frac{(n_1/n_{\text{AIR}} - 1)^2}{(n_1/n_{\text{AIR}} + 1)^2}. \quad (4)$$

At the external boundaries, $n_{\text{AIR}} = 1$, the RI of free space.

At interior nodes, which lie on an interface between two media with different indices of refraction, we apply the conditions used by Schmitt *et al.*,²¹ Takatani and Graham,²² and Faris²³:

$$\hat{\mathbf{n}} \cdot D_1 \nabla \Phi_1(\xi, \omega) = \hat{\mathbf{n}} \cdot D_2 \nabla \Phi_2(\xi, \omega), \quad (5)$$

$$\frac{\Phi_1(\xi, \omega)}{\Phi_2(\xi, \omega)} = \left(\frac{n_1}{n_2} \right)^2. \quad (6)$$

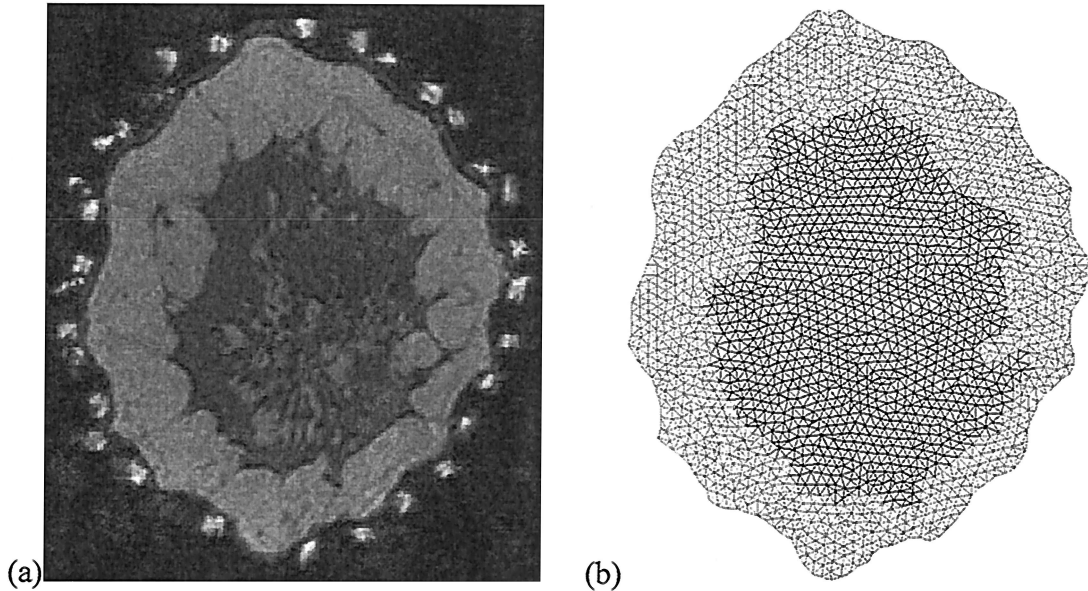


Fig. 1. (a) Coronal slice of an MRI of a female subject showing adipose and glandular tissue layers and (b) the finite-element model mesh created from segmenting the MRI.

These equations enforce continuity in the flux across a step change in RI (n), and establish a corresponding discontinuity in the fluence on the basis of the two RIs defining the regions separating the boundary.

B. Inverse Model

The data is represented by a nonlinear operator $\mathbf{y}^* = F[\mu_a, \kappa]$, where \mathbf{y}^* is a complex vector having a real and imaginary components, which are mapped to log amplitude and phase in measurement. Then the image reconstruction method seeks a solution to

$$(\hat{\mu}_a, \hat{\kappa}) = \arg \min_{\mu_a, \kappa} \|\mathbf{y}^* - F(\mu_a, \kappa)\|, \quad (7)$$

where $\|\cdot\|$ is the weighted L2-norm, representing the square root of the sum of the squared elements. The magnitude of this is sometimes referred to as the projection error and provides a value for determining the convergence of the iterative reconstruction algorithm.

The finite-element method is used as a general and flexible method for solving the forward problem in arbitrary geometries.^{11,24,25} In the inverse problem, in which the aim is to recover internal optical property distributions from boundary measurements, we assume that $\mu_a(\mathbf{r})$ and $\kappa(\mathbf{r})$ are expressed in a basis with a limited number of dimensions (less than the dimension of the finite-element system matrices). A number of different strategies for defining reconstruction bases are possible; in this paper we use a linear pixel basis. To find $(\hat{\mu}_a, \hat{\kappa})$ in Eq. (7), we used a Levenberg–Marquardt algorithm in which is repeatedly solved

$$\mathbf{a} = J^T(JJ^T + \rho I)^{-1}\mathbf{b}, \quad (8)$$

where \mathbf{b} is the data vector, $\mathbf{b} = (\mathbf{y}^* - F[\mu_a, \kappa])^T$; \mathbf{a} is

the solution update vector, $\mathbf{a} = [\delta\kappa; \delta\mu_a]$; ρ is the regularization factor; and J is the Jacobian (sensitivity or weight) matrix for the DA model that is calculated with the Adjoint method.²⁶

3. Simulation Methods

An MRI of a female subject, Fig. 1(a), was used to create a two-dimensional mesh Fig. 1(b).¹⁹ The mesh contained 2306 nodes corresponding to 4042 linear triangular elements and has a major and minor axis diameter of 101 and 82 mm, respectively. For this subject, experimental data was collected with an MRI-NIR system.¹⁹ We combined the NIR measurements with *a priori* anatomical information from the MRI (assuming no RI variation) to estimate the optical absorption and reduced scatter for each tissue type. These procedures generated estimates of the adipose layer as having an absorption of 0.003 mm^{-1} and a reduced scatter of 0.95 mm^{-1} , whereas the glandular tissue resulted in an absorption of 0.006 mm^{-1} and a reduced scatter of 1.1 mm^{-1} . Alternatively, assuming a single tissue type within the breast, we calculated bulk properties for the breast as having an absorption of 0.0056 mm^{-1} and a reduced scatter of 1.125 mm^{-1} . Assuming an RI of 1.455 for the adipose tissue¹⁵ and an RI of 1.2, 1.3, or 1.4 for glandular tissue, we calculated data with the presence of an anomaly within the breast, for two separate cases:

1. Assuming a homogenous distribution of absorption and reduced scatter of 0.0056 and 1.125 mm^{-1} , respectively, it was assumed that the RI varied between each layer with a value of 1.455 for the adipose tissue and 1.2, 1.3, or 1.4 for glandular tissue. The modeled anomaly, as shown in Fig. 2 (top row) had a contrast in absorption and reduced scatter only and

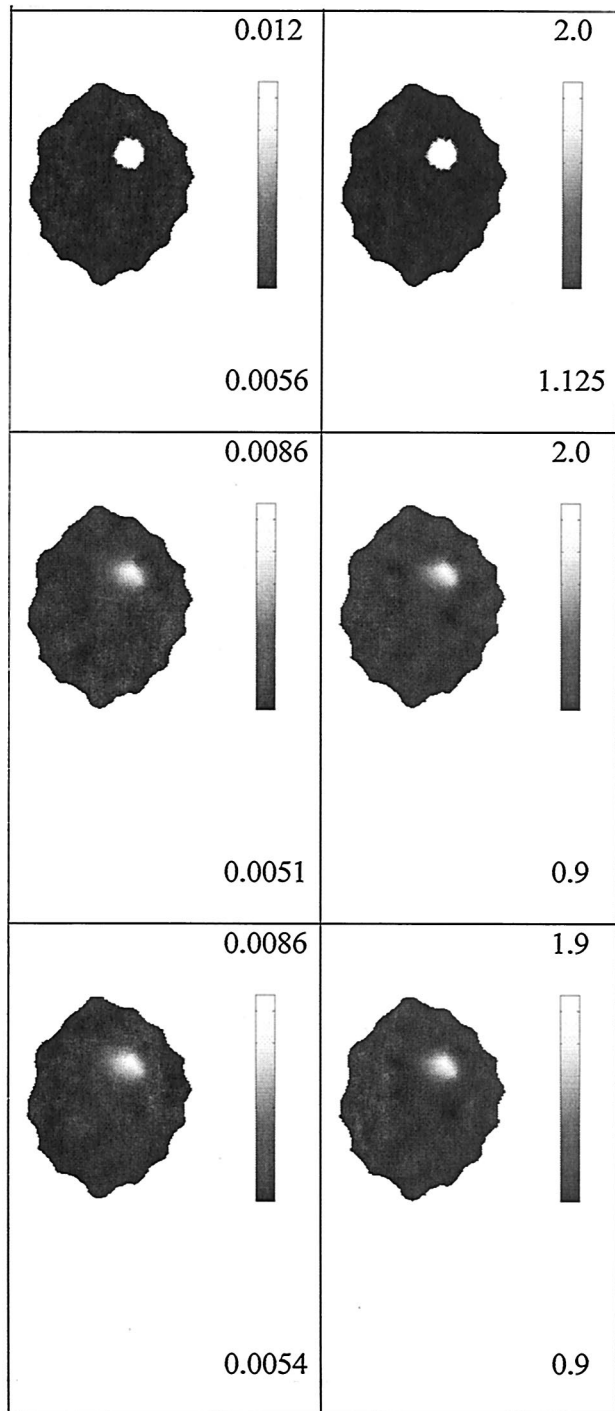


Fig. 2. Images [left column, absorption (mm^{-1}); right column, reduced scatter (mm^{-1})] reconstructed from synthetic data generated with a model with RI variation. Top row shows the exact optical properties; the adipose and glandular zones have the identical optical properties but different RI of 1.455 and 1.4, respectively. Middle row shows reconstructed images assuming the correct RI (same as in top row) distribution. Bottom row shows reconstructed images assuming a homogenous RI of 1.455.

was assumed to have the same RI as glandular tissue.

2. The adipose layer had an absorption of

0.003 mm^{-1} and a reduced scatter of 0.95 mm^{-1} , whereas the glandular tissue had an absorption of 0.006 mm^{-1} and a reduced scatter of 1.1 mm^{-1} . The RI varied between each layer with a value of 1.455 for the adipose tissue and 1.2, 1.3, or 1.4 for glandular tissue. The modeled anomaly, as shown in Fig. 5 below, (top row) had a contrast in absorption and reduced scatter only and was assumed to have the same RI as glandular tissue.

Boundary data was modeled for 16 equally spaced sources and detectors arranged on the external periphery of the model, with added Gaussian noise of 1% in amplitude and 1° in phase. For each set of data, two types of reconstruction were investigated: (i) correct (*a priori*) information on RI variation and (ii) a constant RI of 1.455. In all cases images were reconstructed on a 20×20 uniform grid basis by use of an initial regularization [Eq. (8)] of $\rho = 10$, and the number of iterations was continued until the projection error [Eq. (7)] changed by less than 1% from the previous iteration.¹

4. Results

In each of the cases described in Section 3, the simulated data were calibrated with methods described elsewhere^{1,27,28} to provide an estimate of the bulk optical properties of absorption and reduced scatter for initiating the reconstruction algorithm.

Figure 2 shows the exact (top row) and the reconstructed images for the model, which has a homogeneous absorption and reduced scatter of 0.0056 and 1.125 mm^{-1} , respectively, except within the anomaly that was assigned values of 0.012 and 2 mm^{-1} . The RI is 1.455 for the adipose tissue and 1.4 for the glandular and the anomaly tissues. Images were reconstructed assuming either correct values of RI for each layer (middle row) or a constant RI distribution of 1.455 (bottom row). In each case, images of absorption and reduced scatter were recovered simultaneously by use of log amplitude and phase of the NIR data.

Figures 3 and 4 present exact (top row) and reconstructed images in which the model is identical to that in Fig. 2, except for the RI of the glandular and the anomaly tissues, which was set to 1.3 and 1.2, respectively.

Figure 5 shows exact (top row) and reconstructed images in which the adipose layer had an absorption of 0.003 mm^{-1} and a reduced scatter of 0.95 mm^{-1} whereas the glandular tissue had an absorption of 0.006 mm^{-1} and a reduced scatter of 1.1 mm^{-1} . The anomaly within the glandular tissue had an absorption of 0.012 mm^{-1} and a reduced scatter of 2 mm^{-1} . The RI was 1.455 for the adipose tissue and 1.4 for the glandular and the anomaly tissues. As in Fig. 2, images were produced assuming either the correct values for the RI in each layer (middle row) or a homogeneous RI distribution of 1.455 (bottom row). Figures 6 and 7 show analogous results to those in Figure 5, except for the RI of the glandular and the

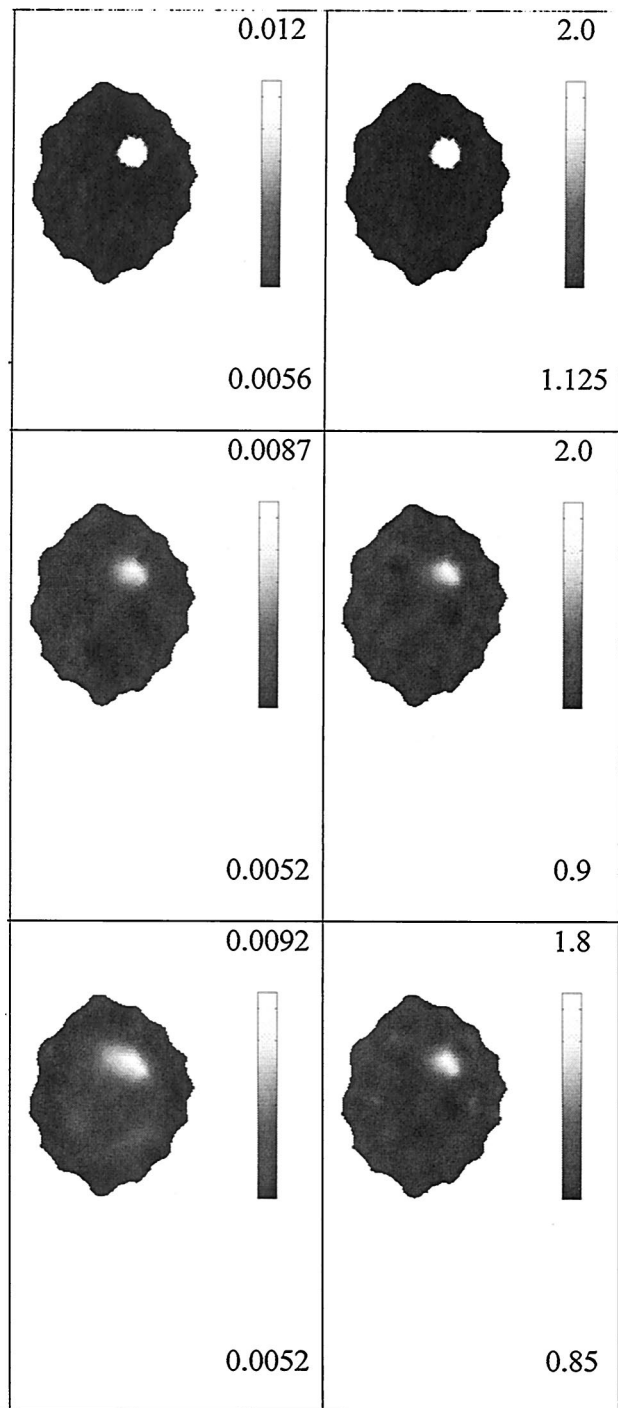


Fig. 3. Same as Fig. 2 except that the glandular tissue (and the anomaly) has an RI of 1.3.

anomaly tissues, which was set to 1.3 and 1.2, respectively.

5. Discussion

In cases in which the tissue is optically (absorption and reduced scatter) homogenous (except for an anomaly) but has different RIs for different tissue types, the recovered optical properties are very similar to the expected values, yielding a peak value of

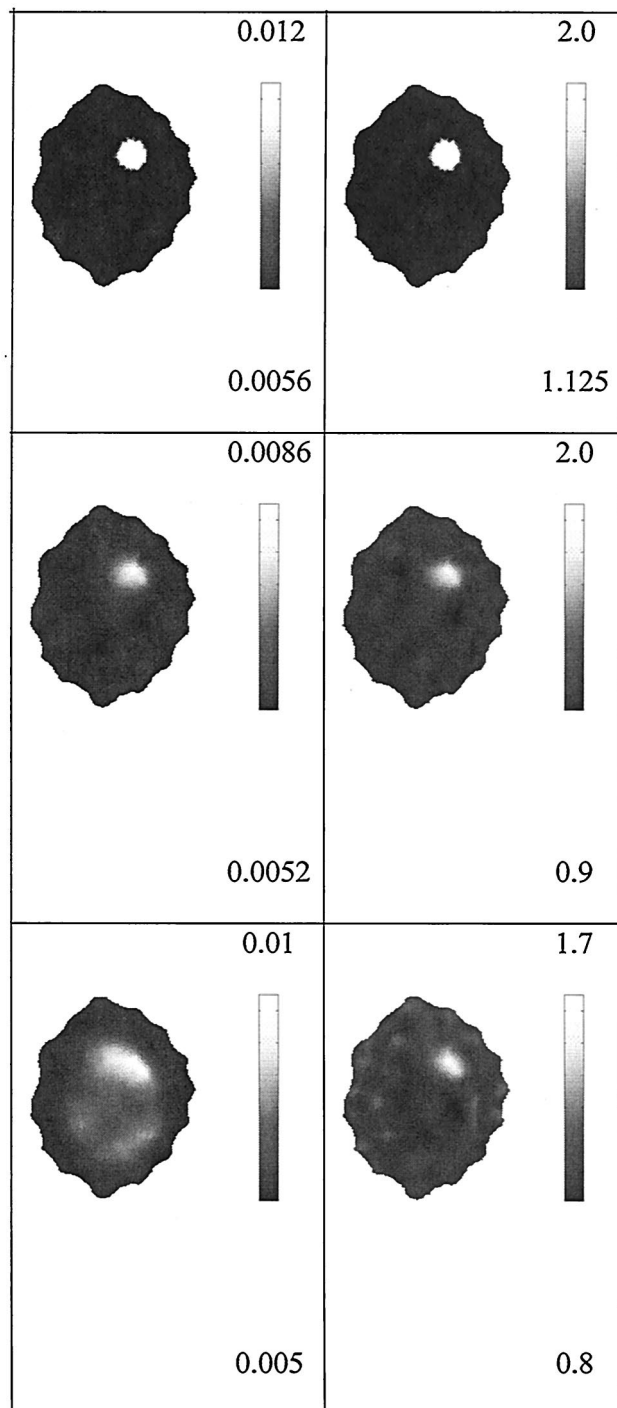


Fig. 4. Same as Fig. 2 except that the glandular tissue (and the anomaly) has an RI of 1.2.

the anomaly for absorption and reduced scatter of approximately 0.0087 and 2.0 mm^{-1} , respectively, when correct *a priori* information on RI distribution is applied throughout the model. Assuming that the model is also uniform in RI, the quality of the reconstructed images varies, depending on the degree of deviation from the true values of RI as expected. For small deviations of RI, that is, when the glandular tissue has an RI of 1.455 but is assumed to be 1.4, the

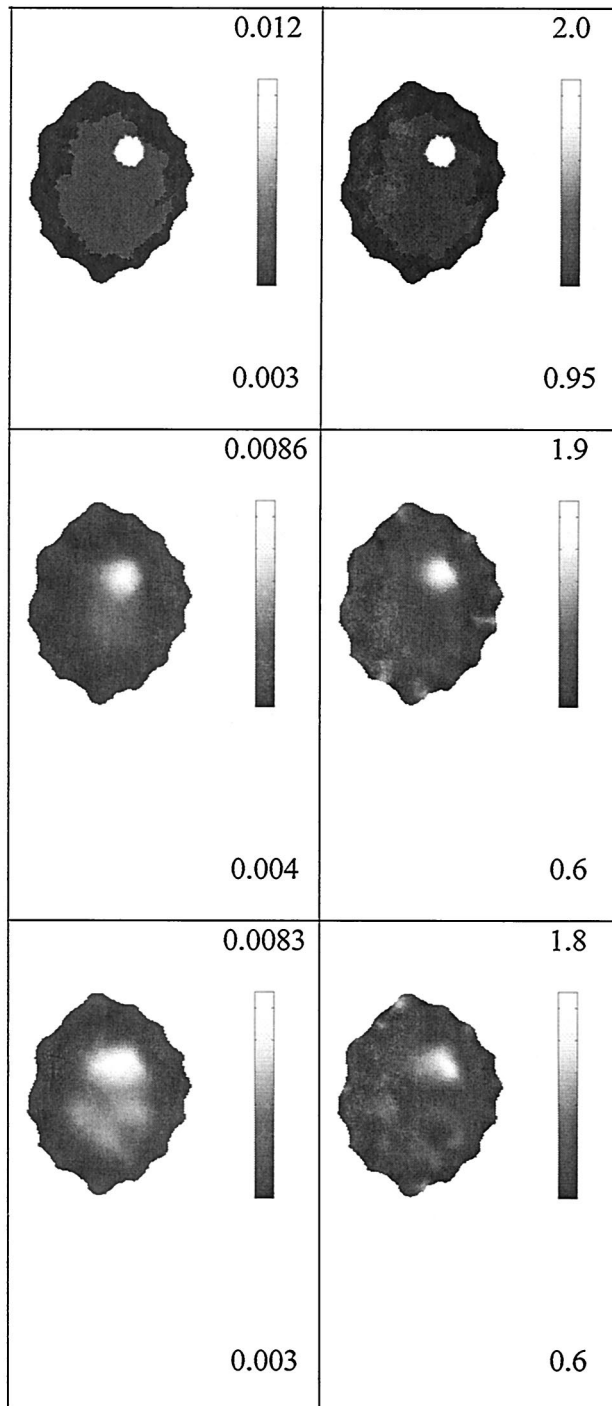


Fig. 5. Images [left column, absorption (mm^{-1}); right column, reduced scatter (mm^{-1})] reconstructed from synthetic data generated with a model with RI variation. Top row shows the exact optical properties; the adipose and glandular tissue have different optical properties and different RI of 1.455 and 1.4, respectively. Middle row shows reconstructed images assuming the correct RI distribution. Bottom row shows reconstructed images assuming a homogenous RI of 1.455.

reconstructed images are very similar to the case in which correct RI is assumed, Fig. 2. As the deviation is increased (Figs. 3 and 4), the quality of the recon-

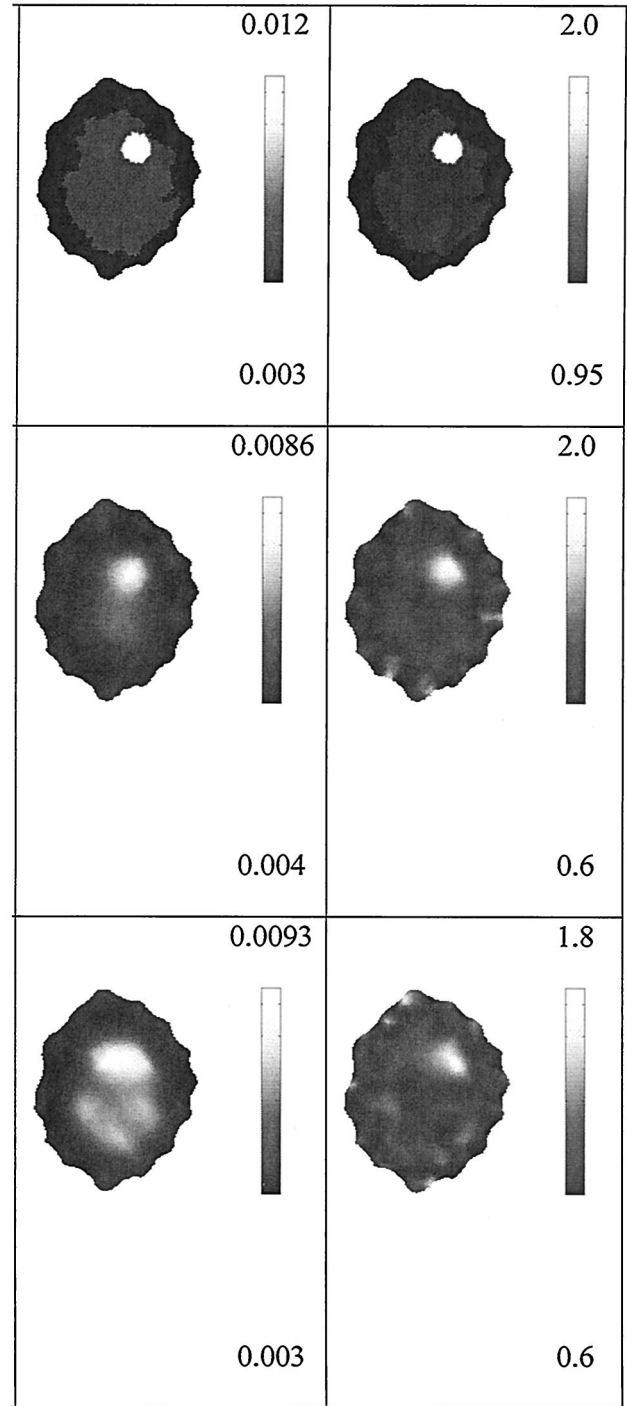


Fig. 6. Same as Fig. 5 except that the glandular tissue (and the anomaly) has an RI of 1.3.

structed images is reduced. For example, in Fig. 4 (an assumed value of 1.2 for glandular tissue RI), the amount of background noise in absorption and scatter is increased, and the recovered anomaly is blurred and overly smoothed. Interestingly, the peak value of absorption has increased to 0.01 mm^{-1} .

When the tissue is heterogeneous in both optical (absorption and reduced scatter) properties and RI, correct *a priori* information on the RI distribution

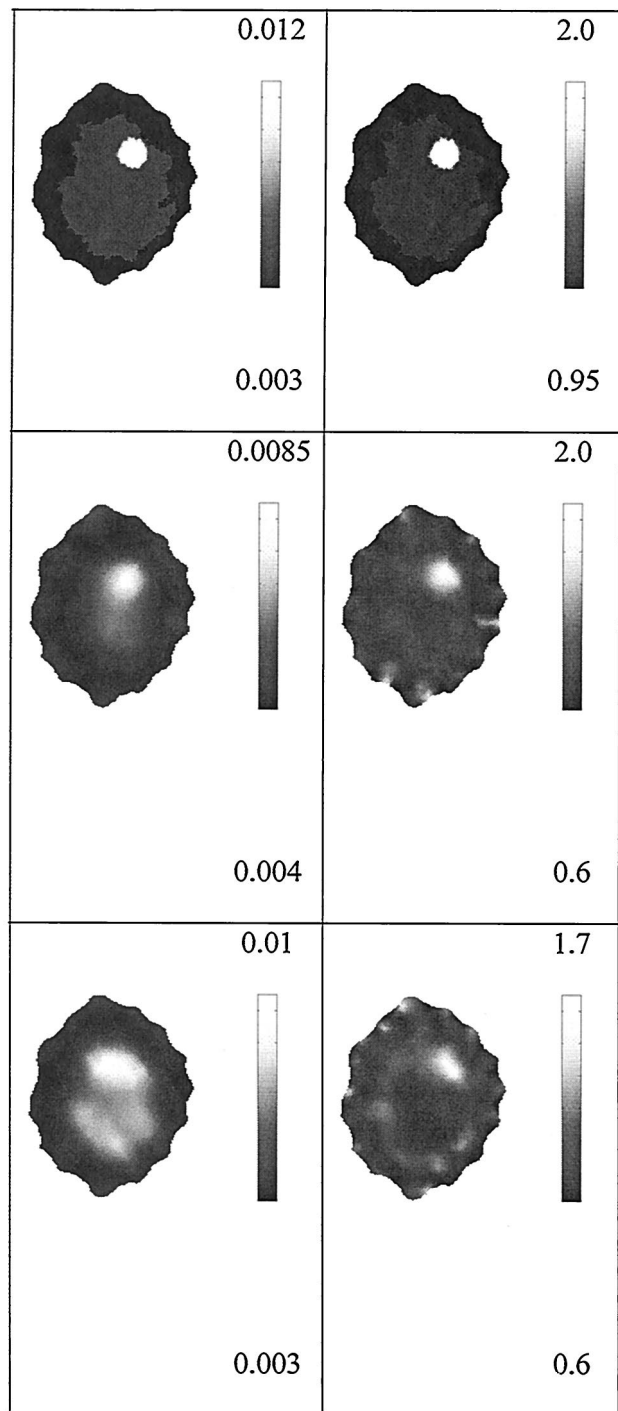


Fig. 7. Same as Fig. 5 except that the glandular tissue (and the anomaly) has an RI of 1.2.

throughout the model generates recovered optical properties that are very similar to the expected values, yielding a peak value in the anomaly for absorption and reduced scatter of approximately 0.0086 and 2.0 mm^{-1} , respectively. If the reconstruction assumes a uniform RI, the quality of the reconstructed images again varies, depending on the level of deviation from the true distribution of RI. For small deviations, the

reconstructed images are similar to the case in which correct RI is used (Fig. 5). As the deviation of the assumed RI increases (Figs. 6 and 7), the quality of the reconstructed images is reduced, but the peak value of recovered absorption increases. In Fig. 7, for example, the RI of the glandular tissue is 1.2, whereas the assumed value for the homogenous reconstruction is 1.455 (bottom row). As in the homogenous case, the amount of background noise in absorption and scatter is increased; however, the recovered anomaly is blurred and overly smoothed, and the peak value of absorption has increased to 0.01 mm^{-1} .

Figure 8 shows the sensitivity map (Jacobian matrix) of log amplitude and absorption for a single source and detector, where the RI distribution is assumed to be either homogeneous at 1.455 or heterogeneous with an adipose layer of RI = 1.455 and a glandular layer of RI = 1.2. From this figure, it evident that a decrease in RI of the glandular tissue reduces the sensitivity deep within the breast. This reduction in sensitivity may explain the increased errors observed when a homogenous assumption of RI is used for image reconstruction. A lower sensitivity within the glandular region will give rise to overly smoothed reconstructed images. However, note that an assumption for the glandular tissue RI of 1.2 is probably not realistic and is only included here for bracketing the effects on image reconstruction.

The recovery of the reduced scatter images seems to have been less affected by the variation of the RI. Although only the sensitivity maps of log amplitude and absorption are only shown, similar trend is seen for other available data types and optical properties (log amplitude or phase versus absorption and scatter). However, it is important to note that the magnitude of the reduced sensitivity for scatter and log amplitude or phase (not shown) is much smaller than that seen for log amplitude and absorption.

6. Conclusion

The effect of discrete RI changes within breast tissue upon NIR image reconstruction has been investigated. Previous studies¹¹ reported our results in modeling the effect of RI on the forward model. In our current results, the initiative was advanced to investigate the effect of RI variation on NIR image reconstruction, either by assumption of correct knowledge of the RI of each tissue or by application of a homogenous value throughout the model.

Synthetic measurement data have been generated from a realistic two-dimensional breast MRI, exhibiting two distinct layers of adipose and glandular tissue. Published values exist for the RI of adipose tissue but not for the glandular tissue. However, it is generally accepted that glandular tissue has a lower RI, and we have assumed a value of 1.4.¹⁶ Nonetheless, to illustrate the effects of RI variation with NIR image reconstruction, we have generated data assuming an RI of glandular tissue of 1.4, 1.3, or 1.2. Furthermore, we have also modeled two distinct

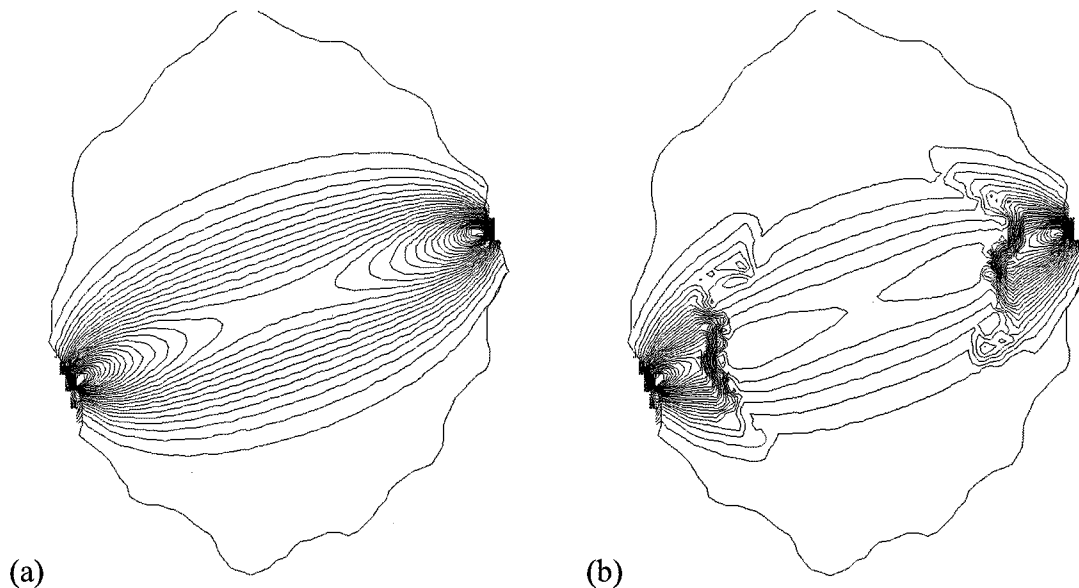


Fig. 8. Sensitivity map (30 contour lines) of log amplitude to absorption changes for a single source and detector combination for (a) a model of homogenous RI of 1.455 having a maximum value of 1.4×10^{-10} and a minimum value of -1.72 and (b) a heterogeneous RI of adipose, 1.455, and glandular tissue, 1.2, having a maximum value of 1.3×10^{-10} and a minimum value of -1.78 .

cases in which each layer had either the same or different absorption and reduced scatter properties, allowing us to separate the effects of absorption and reduced scatter from RI variation. In either case, we modeled an anomaly deep within the breast and reconstructed images assuming either correct information on the RI or simply assuming it to be homogenous.

The reconstructed images show that providing the RI of the glandular tissue, when it is not far from the value of adipose tissue, has little effect on the qualitative and quantitative accuracy of the results. For the layered model (Figs. 5–7) the difference in contrast of the reconstructed anomaly (between use of the correct RI or a homogenous value) is 3.5% when the actual glandular tissue RI is 1.4 (but assumed to be 1.455) and increases to 16% when the actual glandular tissue RI is 1.2. If the RI variation is not modeled, the background noise in the reconstructed images increases, and the reconstructed anomaly exhibits a more blurred character, which can be as large as 200% in the absorption images. This increase in noise and in blurriness can be understood by examination of the sensitivity functions in Fig. 8, which show that as the RI of the glandular tissue decreases with respect to adipose tissue, the sensitivity within the glandular tissue also decreases. Another interesting and very important point to note here is that when the RI distribution is not correctly modeled within the reconstruction algorithm, the effects of the data mismatched owing to the RI are exhibiting themselves within the reconstructed absorption images, clearly seen in Figs. 3 and 4. Also, images were reconstructed (not shown) assuming a homogeneous RI of 1.3 and 1.2 in all of the presented results (depending on the RI of the glandular tissue), and sim-

ilar results were found, as presented, when a homogeneous RI of 1.455 was assumed.

Our research has considered only the reconstruction of absorption and reduced scatter with data generated by a model with RI variation. Assuming the RI of the whole breast is similar, for example, the RI is 1.455 for adipose and 1.4 for glandular tissue, reconstructed images of absorption and scatter can be obtained that ignore the effect of RI with modest degradation in the recovery of information about an abnormality. However, it is also important to note that this analysis was completed under the assumption that the abnormality (i.e., tumor) has the same RI as its background tissue and is most typically located in the fibroglandular tissue. Although, a study by Jiang and Xu¹² has reported large variations in the RI of tumors relative to the background, little other pathologic or *in vivo* data exists on the RI of glandular tissue or the various types of tumor. Further studies are needed to establish the RI variation for different types of tumor and to investigate how such variations might alter NIR tomography.

This research has been sponsored by DOD Breast cancer research program DAMD17-03-01-0405 and the National Cancer Institute through grants RO1CA69544 and PO1CA80139.

References

1. H. Dehghani, B. W. Pogue, S. P. Poplack, and K. D. Paulsen, "Multiwavelength three-dimensional near-infrared tomography of the breast: initial simulation, phantom, and clinical results," *Appl. Opt.* **42**, 135–145 (2003).
2. S. Fantini, S. A. Walker, M. A. Franceschini, M. Kaschke, P. M. Schlag, and K. T. Moesta, "Assessment of the size, position, and optical properties of breast tumors *in vivo* by noninvasive optical methods," *Appl. Opt.* **37**, 1982–1989 (1998).

3. J. Hebden, A. Gibson, T. Austin, R. Yusof, N. Everdell, D. Delpy, S. Arridge, J. Meek, and J. Wyatt, "Imaging changes in blood volume and oxygenation in the newborn infant brain using three-dimensional optical tomography," *Phys. Med. Biol.* **49**, 1117–1130 (2004).
4. B. Chance, "Near-infrared (NIR) optical spectroscopy characterizes breast tissue hormonal and age status," *Acad. Radiol.* **8**, 209–210 (2001).
5. J. C. Hebden, F. M. Gonzalez, A. Gibson, E. M. C. Hillman, R. Yusof, N. Everdell, D. T. Delpy, G. Zaccanti, and F. Martelli, "Assessment of an *in situ* temporal calibration method for time-resolved optical tomography," *J. Biomed. Opt.* **8**, 87–92 (2003).
6. A. Y. Bluestone, G. Abdoulaev, C. Schmitz, R. L. Barbour, and A. H. Hielscher, "Three-dimensional optical-tomography of hemodynamics in the human head," *Opt. Express* **9**, 272–286 (2001), <http://www.opticsexpress.org>.
7. E. M. C. Hillman, J. C. Hebden, M. Schweiger, H. Dehghani, F. E. W. Schmidt, D. T. Delpy, and S. R. Arridge, "Time resolved optical tomography of the human forearm," *Phys. Med. Biol.* **46**, 1117–1130 (2001).
8. H. Xu, H. Dehghani, B. W. Pogue, R. Springett, K. D. Paulsen, and J. Dunn, "Near-infrared imaging in the small animal brain: optimization of fiber positions," *J. Biomed. Opt.* **8**, 102–110 (2003).
9. T. O. McBride, B. W. Pogue, S. Jiang, U. L. Osterberg, K. D. Paulsen, and S. P. Poplack, "Multi-spectral near-infrared tomography: a case study in compensating for water and lipid content in hemoglobin imaging of the breast," *J. Biomed. Opt.* **7**, 72–79 (2002).
10. S. R. Arridge, "Optical tomography in medical imaging," *Inv. Probl.* **15**, R41–R93 (1999).
11. H. Dehghani, B. Brooksby, K. Vishwanath, B. W. Pogue, and K. D. Paulsen, "The effects of internal refractive index variation in near-infrared optical tomography: a finite element modelling approach," *Phys. Med. Biol.* **48**, 2713–2727 (2003).
12. H. Jiang and Y. Xu, "Phase-contrast imaging of tissue using near-infrared diffusing light," *Med. Phys.* **30**, 1048–1051 (2003).
13. J. H. Lee, S. Kim, and Y. T. Kim, "Finite element method for diffusive light propagations in index-mismatched media," *Opt. Express* **12**, 1727–1740 (2004), <http://www.opticsexpress.org>.
14. B. Brooksby, H. Dehghani, K. Vishwanath, B. W. Pogue, and K. D. Paulsen, "Internal refractive index changes affect light transport in tissue," in *Optical Tomography and Spectroscopy of Tissue V*, B. Chance, R. R. Alfano, B. J. Tromberg, M. Tamura, and E. M. Sevick-Muraca, eds., *Proc. SPIE* **4955**, 296–304 (2003).
15. F. P. Bolin, L. E. Preuss, R. C. Taylor, and R. J. Ference, "Refractive index of some mammalian tissue using a fiber optic cladding method," *Appl. Opt.* **28**, 2297–2303 (1989).
16. B. J. Tromberg, O. Coquoz, J. B. Fishkin, T. Pham, E. R. Anderson, J. Butler, M. Cahn, J. D. Gross, V. Venugopalan, and D. Pham, "Non-invasive measurements of breast tissue optical properties using frequency-domain photon migration," *Phil. Trans. R. Soc. Lond. B* **352**, 661–668 (1997).
17. S. Srinivasan, B. W. Pogue, S. Jiang, H. Dehghani, C. Kogel, S. Soho, J. J. Gibson, T. D. Tosteson, S. P. Poplack, and K. D. Paulsen, "Interpreting hemoglobin and water concentration, oxygen saturation and scattering measured *in vivo* by near-infrared breast tomography," *Proc. Natl. Acad. Sci. USA* **100**, 12349–12354 (2003).
18. B. W. Pogue, S. Jiang, H. Dehghani, C. Kogel, S. Soho, S. Srinivasan, X. Song, S. P. Poplack, and K. D. Paulsen, "Characterization of hemoglobin, water and NIR scattering in breast tissue: analysis of inter-subject variability and menstrual cycle changes relative to lesions," *J. Biomed. Opt.* **9**, 541–552 (2004).
19. B. Brooksby, S. Jiang, C. Kogel, M. Doyley, H. Dehghani, J. B. Weaver, S. P. Poplack, B. W. Pogue, and K. D. Paulsen, "Magnetic resonance-guided near-infrared tomography of the breast," *Rev. Sci. Instrum.* **75**, 5262–5270 (2004).
20. M. Schweiger, S. R. Arridge, M. Hiroaka, and D. T. Delpy, "The finite element model for the propagation of light in scattering media: boundary and source conditions," *Med. Phys.* **22**, 1779–1792 (1995).
21. J. M. Schmitt, G. X. Zhou, E. C. Walker, and R. T. Wall, "Multilayer model of photon diffusion in skin," *J. Opt. Soc. Am. A* **7**, 2141–2153 (1990).
22. S. Takatani and M. Graham, "Theoretical analysis of diffuse reflectance from a two-layer tissue model," *IEEE Trans. Biomed. Eng.* **26**, 656–664 (1979).
23. G. W. Faris, "Diffusion equation boundary conditions for the interface between turbid media: a comment," *J. Opt. Soc. Am. A* **19**, 519–520 (2002).
24. H. Jiang, K. D. Paulsen, U. L. Osterberg, B. W. Pogue, and M. S. Patterson, "Optical image reconstruction using frequency-domain data: simulations and experiments," *J. Opt. Soc. Am. A* **13**, 253–266 (1996).
25. S. R. Arridge, M. Schweiger, M. Hiraoka, and D. T. Delpy, "A finite element approach for modeling photon transport in tissue," *Med. Phys.* **20**, 299–309 (1993).
26. S. R. Arridge and M. Schweiger, "Photon-measurement density functions. Part 2: Finite-element-method calculations," *Appl. Opt.* **34**, 8026–8037 (1995).
27. T. O. McBride, B. W. Pogue, U. L. Osterberg, and K. D. Paulsen, "Strategies for absolute calibration of near infrared tomographic tissue imaging," in *Oxygen Transport to Tissue XXIV*, J. F. Dunn and H. M. Schwartz, eds., *Adv. Exp. Med. Biol.* **531**, 85–99 (2003).
28. T. McBride, "Spectroscopic reconstructed near infrared tomographic imaging for breast cancer diagnosis," Ph.D. dissertation (Dartmouth College, Hanover, 2001).

Spectrally constrained chromophore and scattering near-infrared tomography provides quantitative and robust reconstruction

Subhadra Srinivasan, Brian W. Pogue, Shudong Jiang,
Hamid Dehghani, and Keith D. Paulsen

A multispectral direct chromophore and scattering reconstruction technique has been implemented for near-infrared frequency-domain tomography in recovering images of total hemoglobin, oxygen saturation, water, and scatter parameters. The method applies the spectral constraint of the chromophores and scattering spectra directly in the reconstruction algorithm, thereby reducing the parameter space of the inversion process. This new method was validated by use of simulated and experimental data, and results show better robustness and stability in the presence of higher levels of noise. The method suppresses artifacts, especially those significant in water and scatter power images, and reduces cross talk between chromophore and scatter parameters. Variation in scattering was followed by this spectral approach successfully in experimental data from 90-mm-diameter cylindrical phantoms, and results show linear variation in scatter amplitude and reduced scattering coefficient (μ_s'), with total hemoglobin, oxygen saturation, and water remaining constant and quantitatively accurate. Similar experiments were carried out for varying oxygen saturation and total hemoglobin. Accurate quantification was obtained with a mean error of 7.7% for oxygen saturation and 6.2% for total hemoglobin, with minimal cross talk between different parameters. © 2005 Optical Society of America

OCIS codes: 170.3010, 170.6960.

1. Introduction

Near-infrared (NIR) tomography can be used to characterize malignant and normal tissue based on the high-contrast available from heme in the blood, leading to images that are related to intrinsic pathophysiologic processes such as angiogenesis and hypoxia. Absorption-based parameters can be recovered such as total hemoglobin in the tissue, hemoglobin oxygen saturation, and water fraction. It is also possible to estimate elastic scattering images that may provide information about the composition of the tissue. *In vivo* studies have demonstrated levels of hemoglobin in tumors over twice that in normal breast,^{1,2} and lower levels of oxygen saturation have been found in malignancies^{2,3}; however, one of the current chal-

lenges is to optimize the quantitative accuracy with which these parameters can be determined. The quantification of chromophores and scattering parameters relies upon the spectral decomposition of the images acquired at a sparse number of discrete wavelengths instead of a complete spectrum. This sparse spectral sampling coupled with an image reconstruction process that is ill posed, tends to amplify errors in quantifying the spatially resolved parameters of the tissue. In this study a spectrally constrained approach to image reconstruction is introduced, which follows the recent pioneering developments proposed by Corlu *et al.*⁴ and Li *et al.*,⁵ who showed that incorporation of spectral information into the reconstruction process improves the uniqueness of the image formation by using continuous-wave data. In this paper the addition of phase information and the improved accuracy in fitting water and scattering power are specifically examined by use of this spectrally constrained approach. The improvement in quantification of water and scattering has dramatic implications in terms of the value of these particular parameters in breast imaging. The potential to reduce cross talk between chromophores is also important.

The authors are with the Department of Biomedical Engineering, Thayer School of Engineering, Dartmouth College, P.O. Box 8000, Hanover, New Hampshire 03755. S. Srinivasan's e-mail address is subha@dartmouth.edu.

Received 27 August 2004; revised manuscript received 22 November 2004; accepted 5 December 2004.

0003-6935/05/101858-12\$15.00/0

© 2005 Optical Society of America

In earlier research the absorption and scattering coefficients were recovered from boundary measurements of amplitude or phase or both on the object of interest, such as the breast or brain, by means of computational models in which both analytical and numerical approaches were used by different research groups.^{6–8} After recovery of these optical coefficients, a spectral fitting to known absorption signatures of oxyhemoglobin, deoxyhemoglobin, and water is used to obtain the concentrations of these absorbing chromophores. Similarly, the reduced scattering coefficients at separate wavelengths were fit to yield the scatter amplitude (a) and scatter power (b), which are related to the structure of the tissue in terms of scatterer size and density. In this paper a modified reconstruction approach is used, which implements the possible spectral shapes of the chromophore and scattering models into the image formation process, thereby adding a spectral constraint into the reconstruction. The chromophore concentrations and scatter parameters are estimated directly by incorporating the known Beer's law attenuation relation and Mie scattering behavior as constraints. This type of parameter reduction has been applied in electrical impedance tomography in which Brandstatter *et al.*⁹ showed that by using multifrequency data and by assuming a frequency dependence, one can reduce the ill-posed nature of the problem and make the reconstruction more robust to noise in data. A similar application in microwave image reconstruction¹⁰ provides evidence of reduced artifacts in the images as a result of coupling measurements from different frequencies. Corlu *et al.*⁴ implemented this approach by using continuous-wave (cw) measurements to find the optimal four wavelengths that reduce the cross talk between absorption and scatter parameters. Their results from simulations are encouraging and are based on the assumption that all change in scattering is due to the scatter amplitude with the scatter power kept constant. A similar approach to cw data has been implemented by Li *et al.*⁵ used two of three wavelengths under the assumption that there is no scattering perturbation. They have applied this method to find chromophore concentrations directly and have shown in simulated and experimental data that their technique results in reduced image artifacts and parameter cross talk.

In the current study this overall approach is extended to the application of frequency-domain data, using six wavelengths. The method is evaluated with experimental data following individual variation of oxygen saturation, hemoglobin, and scattering parameters. A finite-element model of the diffusion equation is used, and the algorithm reconstructs images for five parameters: oxyhemoglobin, deoxyhemoglobin, water fraction, scatter amplitude, and scatter power, with no assumptions on the scatter amplitude or power. The results show that the new technique is more robust to noise in measurements than the conventional method. In addition, the spectral constraint reduces the noise in the recovered chromophore con-

centrations, especially in the water and scattering images, and the reconstructions from the experimental data show quantitatively accurate results.

2. Materials and Methods

A. Instrumentation

The NIR frequency-domain system for breast imaging has been described in detail in previous papers.¹¹ Briefly, it consists of optical fibers placed in three planes in a circular geometry. Each plane has 16 source–detector positions, and intensity light modulated at 100 MHz is used at six different wavelengths in the range 660–850 nm. The signals are detected by high-gain photomultiplier tubes, and the electrical signals are passed through rf mixer circuits to heterodyne down to a 500-Hz offset frequency. The signal amplitude and phase are calibrated to compensate for system offsets by matching measured data from homogeneous phantoms¹² to simulated results from the finite-element model. When optimized, the calibrated data have less than 1% offset from simulated values and provide a highly stable data set from which to reconstruct absorption and scattering coefficient images.

B. Reconstruction without Spectral Constraints

Under the assumption that breast tissue is a scatter-dominated medium, the diffusion approximation to the radiative transfer equation^{8,13} was used to model the propagation of light at large distances from the source location. This is given by

$$-\nabla \cdot \kappa(r) \nabla \Phi(r, \omega) + \left(\mu_a(r) + \frac{i\omega}{c} \right) \Phi(r, \omega) = q_0(r, \omega), \quad (1)$$

where $\Phi(r, \omega)$ is the isotropic fluence at modulation frequency ω and position r , $\kappa(r)$ is the diffusion coefficient, $\mu_a(r)$ is the absorption coefficient, c is the speed of light in the medium, and $q_0(r, \omega)$ is an isotropic source. The diffusion coefficient can be written as

$$\kappa(r) = \frac{1}{3[\mu_a(r) + \mu_s'(r)]}, \quad (2)$$

where μ_s' is the reduced scattering coefficient.

A finite-element-based-model solution to this equation was developed and was described and validated in Refs. 14 and 15. Briefly, the forward problem involves solving Eq. (1) for fluence, given an initial distribution of the optical properties, with the appropriate boundary conditions applied. The image reconstruction uses a Newton–Raphson minimization that iteratively updates the optical property parameters based on a least-squares-error norm given by

$$\chi^2 = \sum_i \left[\frac{(\phi_i^{\text{meas}} - \phi_i^{\text{cal}})^2}{\sigma_i^2} \right], \quad (3)$$

where ϕ_i^{meas} is the measured data and ϕ_i^{cal} is the data calculated for an initial distribution of the properties, using the forward solver. Here the measurements are assumed to be independent of each other. Using a Taylor's series approximation for the solution at some close distance from the boundary data (ϕ^{cal}) for the initial distribution and ignoring the higher-order terms, the update in the optical properties is related to the difference between the measured and the calculated data as

$$\partial\phi = \mathfrak{J} \partial\mu, \quad (4)$$

where $\partial\phi$ refers to the change in boundary data; \mathfrak{J} is the Jacobian, the matrix containing the sensitivity of the boundary data to a change in optical properties, $\mathfrak{J} = [\mathfrak{J}_{\mu_a}; \mathfrak{J}_{\kappa}]$; and $\partial\mu$ is the update in the optical properties given by $\partial\mu = [\partial\mu_a; \partial\kappa]$.

The reconstruction is sensitive to the initial estimate of the parameters, which are given by a homogeneous prefitting algorithm based on the analytical solution for infinite medium.¹² The matrix \mathfrak{J} , being ill conditioned, requires that the inverse problem in Eq. (4) be solved with the application of a Levenberg–Marquardt regularization scheme^{16,17} for stabilization. The stopping criterion for this reconstruction was chosen to be when the χ^2 error in Eq. (3), known as the projection error, changes by less than 2% between successive iterations.

Previously¹⁸ the optical properties at each wavelength were obtained, and then the calculation of the chromophore concentrations was performed with a constrained least-squares fit to the Beer's law relation

$$\mu_a = [\varepsilon]c, \quad (5)$$

where ε is the molar absorption spectra of the absorbing chromophores and c is the concentration of these chromophores. Oxyhemoglobin (HbO_2), deoxyhemoglobin (Hb), and water are assumed to be the main absorbers, and their molar absorption spectra were obtained experimentally in our instrument. This approach of using values estimated by the system compensates for any offsets from the theoretical values, yet there was little difference between our experimental and theoretical estimates of molar absorption coefficients. By fitting for the concentrations, we calculate total hemoglobin as $\text{HbT} = \text{HbO}_2 + \text{Hb}$ [in micromolar (μM)] and oxygen saturation as $\text{SO}_2 = \text{HbO}_2/\text{HbT} \times 100$ (in percent); the contribution from other chromophores such as lipids has been found to be negligible, because the wavelengths used here were limited to less than 850 nm where lipid is a weak absorber. The constraints on the fitting process were for HbT to be below 100 μM , oxygen saturation to be nonnegative and with an upper bound of 100%, and water to be in the range [0%, 100%].

Similarly, the μ_s' spectrum of tissue has been shown to fit well to an empirical approximation to Mie scattering theory,^{19,20} given by

$$\mu_s' = a\lambda^{-b}. \quad (6)$$

Equation (6) was used to derive the scatter amplitude (a) and the scatter power (b), with wavelength in micrometers. The coefficient μ_s' has units of inverse millimeters, and b is dimensionless so that a has units given by $10^{-3b}(\text{mm})^{b-1}$. Both the scattering power and the amplitude depend on the scattering center size and number density and may reflect variations in breast structural composition due to different cellular, organelle, and structural sizes and densities for fatty and glandular tissue. Typically, large scatterers have lower b and a values, whereas small scatterers have higher b and a coefficients.^{19,20} Although scatterers in tissue are not necessarily homogeneous spheres, as assumed in Eq. (6), studies on red blood cells and yeast have shown this to be a reasonable approximation since measurements of μ_s' in these cells show trends similar to Mie theory.^{21,22}

C. Spectrally Constrained Chromophore and Scattering Reconstruction

Instead of estimating the optical properties at each wavelength and then spectrally deconvolving the chromophore concentrations [Eqs. (5) and (6)], one can incorporate these constraints into the reconstruction to directly determine oxyhemoglobin, deoxyhemoglobin, water, scatter amplitude, and scatter power, thus reducing the parameter space from 12 images (μ_a and μ_s' at 6 wavelengths) to 5 parametric images. Assuming that we know $\mathfrak{J}_{\mu} = \partial\phi/\partial\mu$ and $\mathfrak{J}_{\kappa} = \partial\phi/\partial\kappa$, as calculated by the previous method (reconstruction without spectral priors), in the new approach the measurements at all wavelengths are coupled together, and the relations in Eqs. (5) and (6) are combined to create a new set of relations, which for each wavelength is represented by

$$\partial\phi_{\lambda} = \mathfrak{J}_{c,\lambda} \partial c + \mathfrak{J}_{a,\lambda} \partial a + \mathfrak{J}_{b,\lambda} \partial b, \quad (7)$$

where

$$\mathfrak{J}_{c,\lambda} = \frac{\partial\phi}{\partial c} \bigg|_{\lambda} = \frac{\partial\phi}{\partial\mu} \frac{\partial\mu}{\partial c} \bigg|_{\lambda},$$

for each chromophore (c) in the model. From Eq. (5) we get $\partial\mu = \varepsilon \partial c$, so that, substituting for $\partial\mu/\partial c$,

$$\begin{aligned} \mathfrak{J}_{c,\lambda} &= \frac{\partial\phi}{\partial c} \bigg|_{\lambda} = \frac{\partial\phi}{\partial\mu} \varepsilon \bigg|_{\lambda} \\ &= \left(\frac{\partial\phi}{\partial\mu} \bigg|_{\mu} \right) \otimes (\varepsilon_{\lambda}^{c1, c2, c3}) = \mathfrak{J}_{\mu, \lambda} \otimes (\varepsilon_{\lambda}^{c1, c2, c3}), \end{aligned} \quad (8)$$

where \otimes refers to the Kronecker tensor product.

Similarly,

$$\mathfrak{J}_{a,\lambda} = \frac{\partial\phi}{\partial a} \bigg|_{\lambda} = \frac{\partial\phi}{\partial\kappa} \frac{\partial\kappa}{\partial a} \bigg|_{\lambda}. \quad (9)$$

Rewriting

$$\frac{\partial \kappa}{\partial a} = \left(\frac{\partial \kappa}{\partial \mu_s'} \right) \left(\frac{\partial \mu_s'}{\partial a} \right)$$

and knowing that

$$\kappa = \frac{1}{3(\mu_a + \mu_s')},$$

we get

$$\frac{\partial \kappa}{\partial \mu_s'} = \frac{1}{3} \left[\frac{-1}{(\mu_a + \mu_s')^2} \right] = \frac{1}{3} (-9\kappa^2) = -3\kappa^2,$$

$$\frac{\partial \mu_s'}{\partial a} = \lambda^{-b}.$$

Substituting these expressions in Eq. (9) leads to

$$\mathfrak{J}_{a,\lambda} = \frac{\partial \phi}{\partial a} = \frac{\partial \phi}{\partial \kappa} \frac{\partial \kappa}{\partial a} \Big|_{\lambda} = \mathfrak{J}_{\kappa} (-3\kappa^2) (\lambda^{-b}) \Big|_{\lambda}. \quad (10)$$

Similarly, for the scatter power

$$\begin{aligned} \mathfrak{J}_{b,\lambda} &= \frac{\partial \phi}{\partial b} = \frac{\partial \phi}{\partial \kappa} \frac{\partial \kappa}{\partial b} \Big|_{\lambda} \\ &= \left(\frac{\partial \phi}{\partial \kappa} \right) \left(\frac{\partial \kappa}{\partial \mu_s'} \right) \left(\frac{\partial \mu_s'}{\partial \ln \mu_s'} \right) \left(\frac{\partial \ln \mu_s'}{\partial b} \right). \end{aligned} \quad (11)$$

Knowing that $\partial \ln \mu_s' = (1/\mu_s') \partial \mu_s' \Rightarrow \partial \mu_s' / \partial \ln \mu_s' = \mu_s'$ and from Eq. (6), $\ln \mu_s' = \ln a - b \ln \lambda$, then it is found that $\partial \ln \mu_s' / \partial b = -\ln \lambda$. Substituting these relations produces

$$\mathfrak{J}_{b,\lambda} = \mathfrak{J}_{\kappa} (-3\kappa^2) (\mu_s') (-\ln \lambda) \Big|_{\lambda}. \quad (12)$$

The overall system of equations is assembled by substituting the relations from Eqs. (8), (10), and (12) into Eq. (7):

$$\begin{pmatrix} \partial \phi_{\lambda 1} \\ \partial \phi_{\lambda 2} \\ \vdots \\ \partial \phi_{\lambda n} \end{pmatrix} = \begin{bmatrix} \mathfrak{J}_{c1,\lambda 1} \mathfrak{J}_{c2,\lambda 1} \mathfrak{J}_{c3,\lambda 1} \mathfrak{J}_{a,\lambda 1} \mathfrak{J}_{b,\lambda 1} \\ \mathfrak{J}_{c1,\lambda 2} \mathfrak{J}_{c2,\lambda 2} \mathfrak{J}_{c3,\lambda 2} \mathfrak{J}_{a,\lambda 2} \mathfrak{J}_{b,\lambda 2} \\ \vdots \\ \mathfrak{J}_{c1,\lambda n} \mathfrak{J}_{c2,\lambda n} \mathfrak{J}_{c3,\lambda n} \mathfrak{J}_{a,\lambda n} \mathfrak{J}_{b,\lambda n} \end{bmatrix} \begin{pmatrix} \partial c_1 \\ \partial c_2 \\ \partial c_3 \\ \partial a \\ \partial b \end{pmatrix}. \quad (13)$$

The size of the left-hand vector is equal to the number of wavelengths multiplied by the number of measurements per wavelength, and the size of the right-hand side vector is equal to the number of chromophores and scatter parameters multiplied by the number of nodes for updating each parameter in the mesh. The individual Jacobian matrices for each chromophore were computed with a dual-mesh technique,²³ on a 2000-node mesh for forward diffusion calculations and a 425-node mesh was used for image reconstruction.

Equation (13) was implemented by building the new Jacobian (5×425 by 480×6), and the same Levenberg–Marquardt regularization scheme was applied. The computation time was approximately 25 min for typically 5–7 iterations, with the measure of convergence being when the projection error was less than 2% of the previous iteration value. Additional constraints based on the physiologically possible values for the parameters were applied at each iteration so that HbT does not exceed 100 μM (based on typical concentrations found in the breast), that oxygen saturation is in the range [0%, 100%], and that water is in the range [0%, 100%]. The scatter amplitude is bounded in the range [0.5, 2.0] in units of $10^{-3b}(\text{mm})^{b-1}$, and the scatter power is in the range [0, 2] based on previous studies,²⁴ so that together they cover the possible range for the reduced scattering coefficient. This range is [0.5, 3.25] mm^{-1} for 785 nm. The approach can easily be extended to additional wavelengths without any computational expense in the inversion process since the size of the new Hessian from Eq. (13) depends on the number of nodes and not on the number of measurements, although the number of wavelengths will influence the calculation of individual Jacobian matrices. The algorithm typically converges after a lower number of iterations than the conventional method does, and no spatial filtering was necessary since the noise in the images is already damped by the spectral constraints.

3. Results

Subsections 3.A and 3.B show the improvement of the spectral technique over the conventional method by quantitative assessment of the mean and standard deviation from recovered images by use of simulated and experimental data. The results shown in Subsections 3.C, 3.D, and 3.E focus on validating the accuracy of the spectral technique in following the variation of scattering, oxygen saturation (Hill curve), and total hemoglobin individually by use of the appropriate experiments.

A. Effect of Noise in Amplitude and Phase Measurements

It is expected that the spectrally constrained nature of this new algorithm will make the reconstruction more immune to noise in measurements as compared with the conventional method, since all data are coupled. More noise in the data is typically observed at 661 nm for tissues containing lower oxygenation (due to high absorption of deoxyhemoglobin) and 849 nm (due to water absorption) and in higher-scattering cases. This behavior is taken into consideration in the algorithm by the *a priori* spectral information. To test the hypothesis of reduced noise sensitivity of the spectral method, we simulated amplitude and phase data at six wavelengths by using the finite-element model for a homogeneous phantom of diameter 86 mm with concentrations of 30 μM HbO₂, 30- μM Hb, 60% water, scatter amplitude of 1 [units of $10^{-3b}(\text{mm})^{b-1}$], and scatter power of 1. This yields

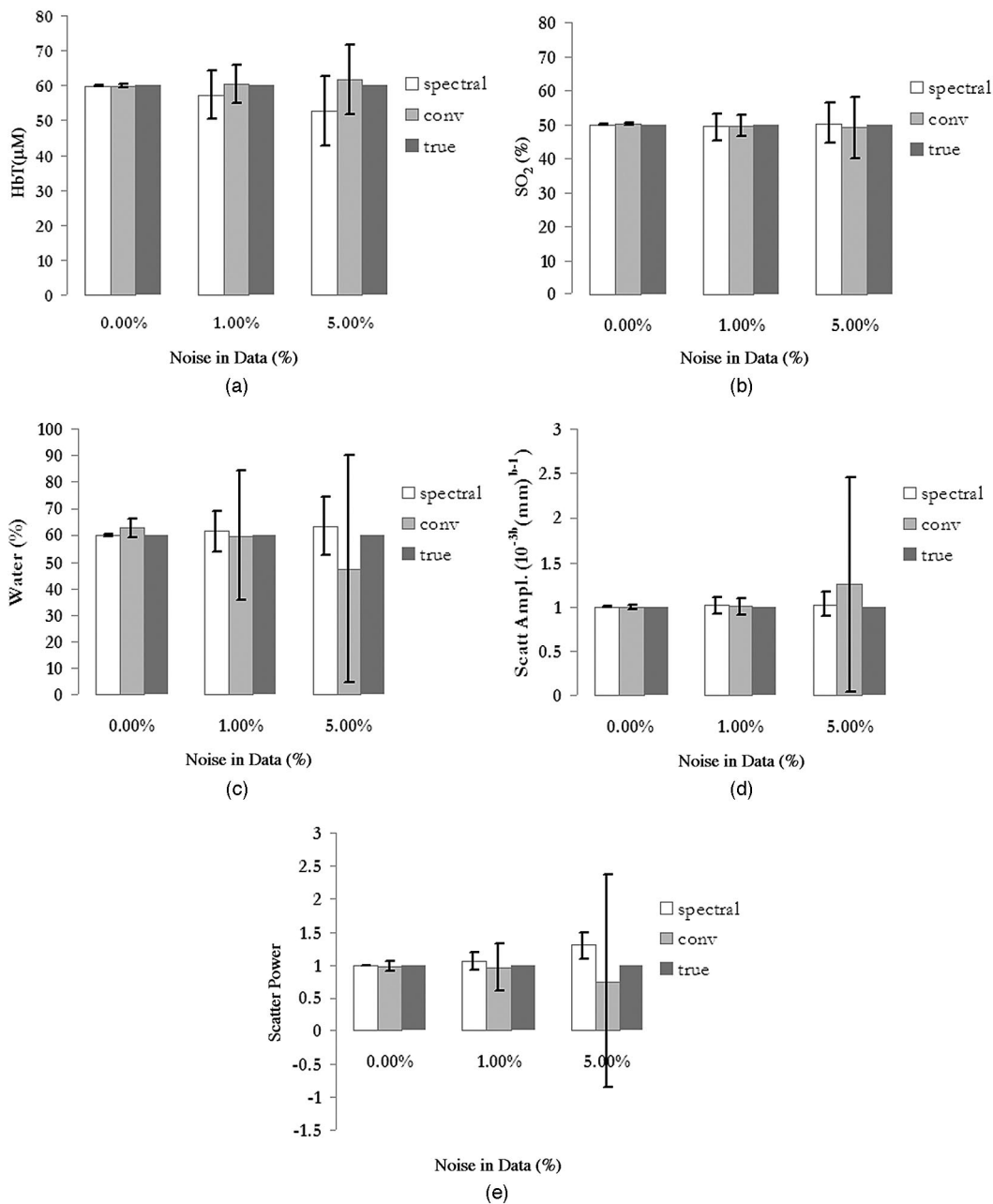


Fig. 1. Recovered mean values with standard deviation error bars are shown for (a) hemoglobin, (b) oxygen saturation (SO_2), (c) water (in percent), (d) scatter amplitude, and (e) scatter power. These were estimated from the interior of a homogeneous field reconstructed with different levels of noise in the original data. Values for the new spectrally constrained reconstruction are shown alongside results from the conventional approach.

total hemoglobin of $60 \mu\text{M}$, $\text{SO}_2 = 50\%$, and μ_s' at $785 \text{ nm} = 1.27 \text{ mm}^{-1}$, which are concentrations typically found in the breast. Random Gaussian distributed noise was added to the amplitude and phase measurements in a systematic manner from 0.5% to 5%, and the spectrally constrained reconstruction was carried out on the data. The conventional technique of reconstructing each wavelength separately and then carrying out the spectral fit was also applied to these data for comparison. The mean and standard deviation for the reconstructed images from both techniques for each of the parameters are plotted in

Fig. 1; the results are shown for the cases with no noise, 1% noise, and 5% noise.

For the noiseless data reconstruction, both techniques show an accurate recovery of all five parameters (mean is within 3% of the true value), with an average standard deviation of 0.5% of the mean for the spectral method and 3.7% for the conventional technique. For the 1% and 5% noise cases, the standard deviation increases as expected; however, this increase is much more evident in the images from the conventional technique than from the spectral method. The results from the spectral method do not

differ significantly from the conventional technique for total hemoglobin and oxygen saturation images; however, the noise is significantly suppressed in the water and scatter images from the spectral method. For 1% noise in data, the mean is still within 5% of the true value for both methods, but the standard deviation in water has reduced from 40% in the conventional method to 12% of the mean for the spectral technique. Even in the 5% noise case, the spectral method shows a reasonable recovery of mean values for the parameters (accurate to within 10% on an average), with a 15.3% standard deviation (as percent of the mean). This shows a reduced sensitivity of the reconstruction to higher levels of noise compared with the conventional method.

B. Reduced Standard Deviation in Homogeneous Experimental Data

To assess the mean and standard deviation from homogeneous images in experimental data, we collected measurements on a liquid tissue-simulating phantom within a plastic circular container of 90-mm diameter, consisting of 9.3- μ M pig blood in buffered saline and 1% Intralipid concentration. The blood hematocrit was measured before the experiment with a clinical co-oximeter that showed 1% of the pig blood contained 9.3 μ M of hemoglobin for this sample. The expected values for the scatter amplitude and scatter power were derived from the work of van Staveren *et al.*¹⁹ Using the expression given by van Staveren *et al.* with the units suitably modified produces the following equation: $\mu_s' = 0.928\lambda^{-1.4} - 0.16\lambda^{-2.4}$. Incorporating the higher-order term into the scatter amplitude factor (since the amplitude factor of the second term is much lower than that of the first term) by assuming that $\mu_s' = 1 \text{ mm}^{-1}$ at 800 nm, the scatter amplitude (a) = 0.73 and the scatter power (b) = 1.4. Water and oxygen saturation are expected to be close to 100%, since the phantom was an oxygenated liquid solution. Both the spectral and conventional techniques were applied to this data, and the mean and standard deviation from the reconstructed images are plotted in Fig. 2(a), along with the expected values. As described in Section 2, both reconstructions were terminated by use of the projection error criterion, and reconstructed parameters 15 mm from the edge have been removed from the calculation of mean and standard deviation to diminish contribution from any boundary artifacts.

Figure 2(a) shows the reduced standard deviation in the images obtained from the spectral method, compared with the conventional technique. The mean values for the parameters are accurate to within 6%, on average, for the spectral scheme and to within 11% for the conventional method. As with the simulations, no spatial filtering is applied to the spectral reconstruction, whereas the conventional method uses a mean filter. The stopping criterion for the spectral technique is a projection error change of less than 2% between iterations, and it converges in seven iterations. For the conventional method, the equivalent 7th iteration at

every wavelength was used to obtain images based on earlier studies²⁵ that indicated 5–9 iterations are most suitable for experimental data. Both methods use the same initial regularization parameter (equal to 10 in this study¹⁵). The main improvement here was the suppression of noise in the water and scattering images by use of the spectral technique.

Figure 2(b) shows the reconstructed images from both methods along with a cross section of the middle plane. The spatial variation in the cross section is less in the spectral technique, and some of the boundary artifacts in the hemoglobin, water, and scatter power images are reduced. The scatter amplitude image shows some artifacts close to the boundary, which may indicate the need for higher regularization for the parameter. The hemoglobin and water images from the conventional technique show some cross talk between the images. A central artifact can be seen in the HbT image in which there is a decrease in its value, with saturation in the water image at this same region (=100%). The scatter parameter images, especially scatter power, show considerable noise that is possibly due to cross talk between the two scatter parameters and between deoxyhemoglobin and scatter.

C. Scattering Parameter Validation

Having shown that spectral reconstruction is superior to the conventional method of reconstructing each wavelength separately and then applying the spectral information in terms of reduced sensitivity to noise in the data and suppression of artifacts in the images, we now focus the following sections on validating the accuracy of the spectral reconstruction. One of the key advantages of the spectral method over the conventional technique is the reduction of noise in the water and scatter parameters. The implementation of this technique on frequency-domain measurements allows the separation of absorption and scatter, and this along with multiwavelength capability allows a modest separation of the scatter amplitude and scatter power. To test the cross talk and noise in the scatter parameters with experimental measurements and to follow their variation, the Intralipid concentration was varied in the liquid phantom solution containing 1% blood, from 0.75% to 1.5% in steps of 0.25% (the data from 1% Intralipid was also used for Fig. 2). The amplitude and phase measurements were taken for each concentration, and the spectrally constrained reconstruction was applied to the data. The total hemoglobin was constant through the varying concentrations of Intralipid, and the saturation for both water and oxygen was 100% for all data sets. The mean value along with standard deviation from the images are plotted for scatter amplitude and scatter power in Fig. 3(a), and Fig. 3(b) shows the average μ_s' at 661 and 785 nm. Figure 3(c) shows the total hemoglobin and Fig. 3(d) shows the oxygen saturation and water content. The scatter amplitude varies linearly with concentration and shows more variation (range 0.6–1.25) than the scatter power (range 1.3–1.53). Scatter power values are

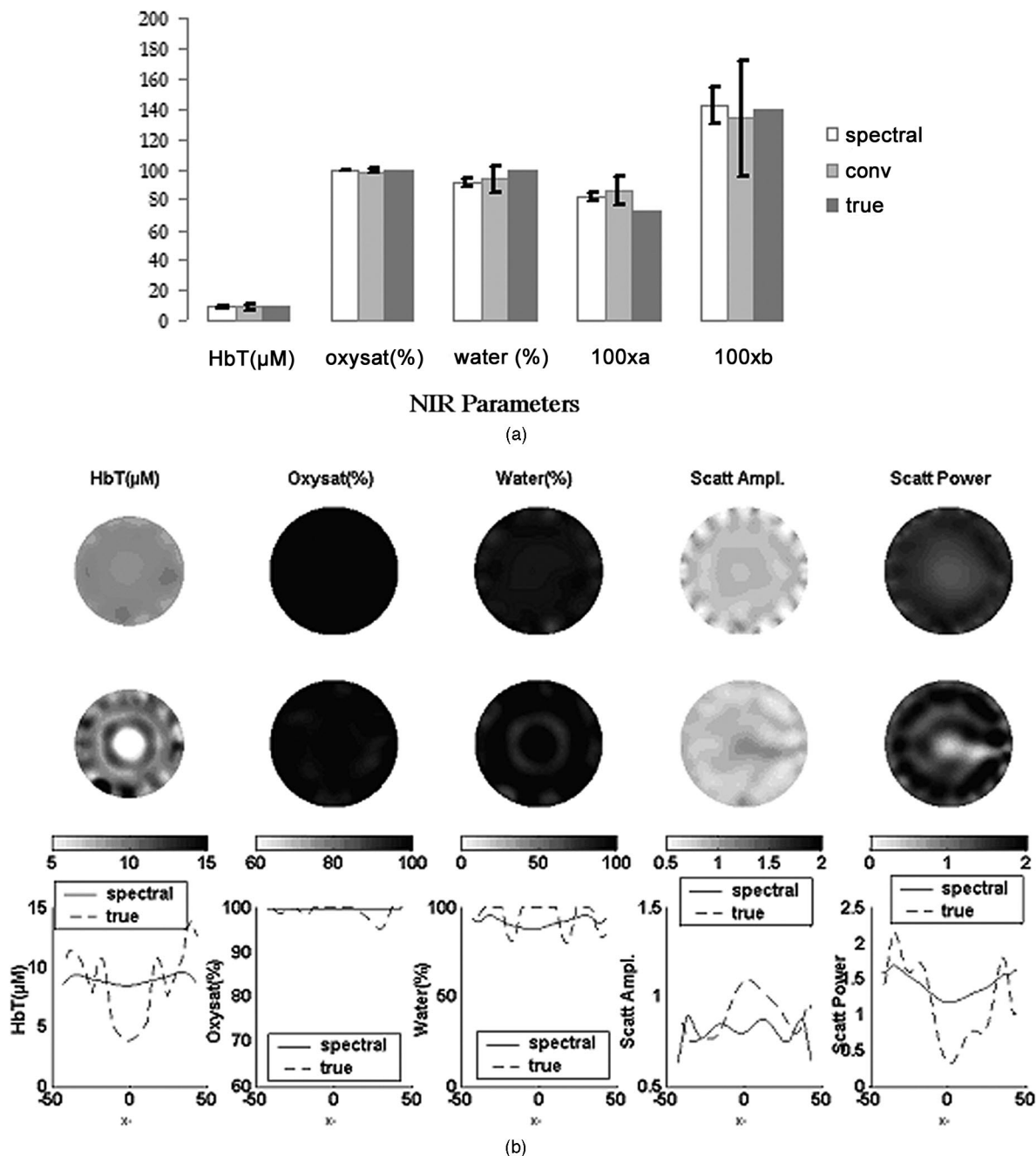


Fig. 2. Recovered mean values with standard deviation error bars are shown in (a) from reconstructed data with a 90-mm-diameter liquid phantom containing 1% Intralipid with 9.3- μM total hemoglobin. Values for the spectrally constrained reconstruction are shown alongside those obtained with the conventional reconstruction approach and the true theoretical values. (b) Images from this phantom are shown for comparison with the spectrally constrained reconstruction (top row), the conventional reconstruction (middle row), and the profile plots from the midplane of these images (bottom row).

comparable with the expected value of 1.4 from van Staveren *et al.*,¹⁹ showing a mean of 1.4 ± 0.1 through the change in concentrations. The mean μ_s' at 785 nm varies linearly (slope of ≈ 1) with the change in percent Intralipid, and the value approximately doubles (0.89 versus 1.7 mm^{-1}) when the concentration doubles from 0.75% to 1.5% Intralipid, which is encouraging. The reduced scattering coefficient at 661 nm also shows a similar trend. The total hemoglobin stays constant with change in scattering

with a mean of $8.2 \mu\text{M} \pm 0.8$, and the oxygen saturation shows a mean value of $99.3\% \pm 1.2\%$, close to expected value of 100%. Water shows an average of $92.4\% \pm 4.2\%$, and some cross talk can be seen between hemoglobin and water at the higher Intralipid concentrations owing to the high-scattering medium.

D. Oxygen Saturation Validation

Malignant tumors typically have lower partial pressure values for oxygen (PO_2) owing to hypoxia,²⁶ and

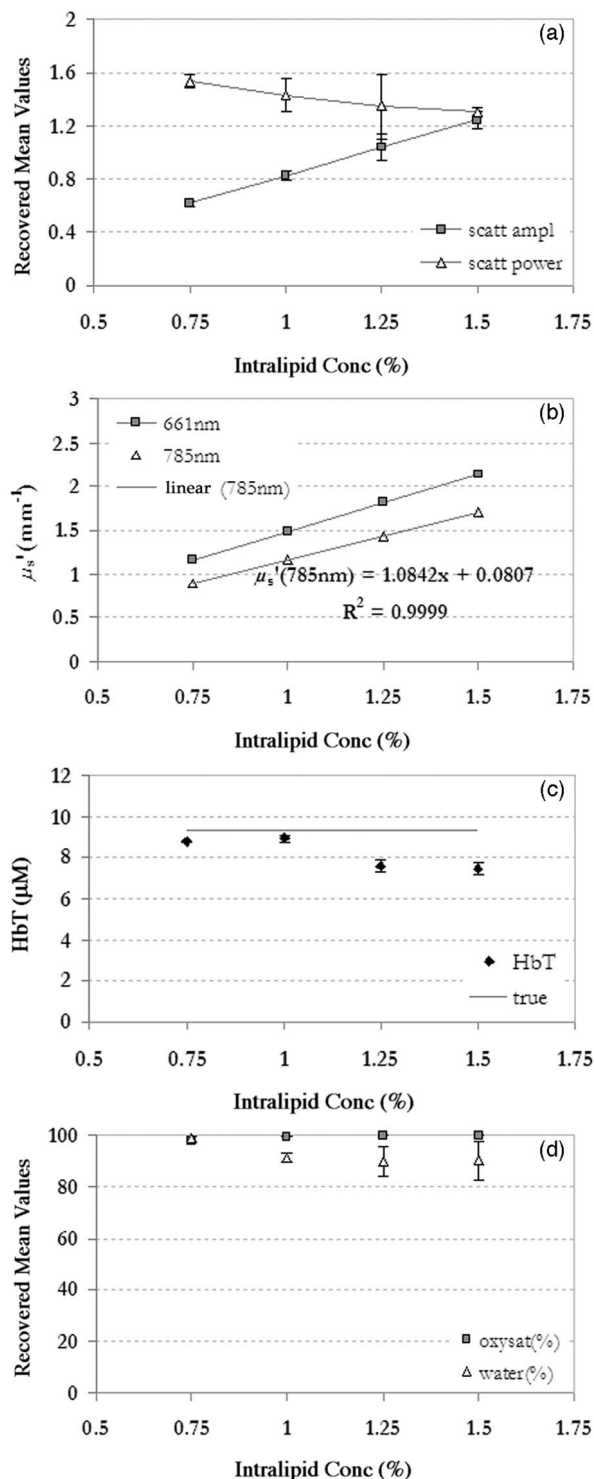


Fig. 3. Recovered mean values are shown from a series of phantoms in which the scattering coefficient was systematically varied through concentrations (Conc) of Intralipid ranging between 0.75% and 1.5%. The estimated scattering power and amplitudes are shown in (a), and the reduced scattering coefficients at 661 and 785 nm are shown in (b). The total hemoglobin, which did not vary, is shown in (c), along with a line corresponding to the theoretical value. In (d) the oxygen saturation and water values are shown, which also did not vary. Both have theoretical estimates of 100%. Error bars represent the standard deviation of all pixels within the interior 60 mm of the region imaged.

it is useful to verify that the spectrally constrained reconstruction can follow these hypoxic conditions. The relation between oxygen saturation and the variation in partial pressure of oxygen has a well-characterized behavior given by the Hill curve. This curve was obtained previously for the conventional method and published in Ref. 27. Data were acquired by use of a phantom solution containing 1% whole blood and 1% Intralipid in saline, in a thin-walled plastic container, 70-mm in diameter. The whole blood (1%) was found to have 18- μM hemoglobin, and the oxygenation of the solution was reduced by varying the PO_2 values from 150 to 0 mm Hg by the addition of yeast. The PO_2 was independently measured by means of a chemical microelectrode after calibration of the electrode overnight in a saline solution. By varying the PO_2 gradually, using a small amount of yeast, and making measurements over this period of time, we eventually reduced the PO_2 to zero and obtained a complete set of data over the required range. The spectral reconstruction of this data gave HbT, SO_2 , water, scatter amplitude, and scatter power images, from which the mean and standard deviation are plotted in Fig. 4. The oxygen saturation in Fig. 4(a) follows the theoretical Hill curve²⁸ reasonably well with a mean error of 7.7%, with the worst accuracy close to zero PO_2 and the higher accuracy when PO_2 is above 80% saturation. For PO_2 below 20-mm Hg, oxygen saturation is still accurate to within 15%, with a low standard deviation in the images.

With variation of PO_2 , the total hemoglobin concentration stayed approximately constant [Fig. 4(b)], with a mean value of $17.5 \pm 2.1 \mu\text{M}$, which is within 97% of the true value given above, and water exhibited a mean value of $94.2\% \pm 8.3\%$. Both parameters show some cross talk at PO_2 values below 11-mm, which is possibly unavoidable owing to the limited number of wavelengths used in these data. Both scatter amplitude and scatter power stay approximately constant until a PO_2 of 11-mm Hg, beyond which both show some variation, which could be the result of cross talk between the two parameters. Above 11-mm Hg, the scatter amplitude has value of $0.92 \pm 0.04 \cdot 10^{-3b}(\text{mm})^{b-1}$, and the scatter power has values of 1.49 ± 0.14 . The reduced scattering coefficient, however, stays constant throughout, as shown for 785 nm in Fig. 4(d), with a mean of $1.3 \pm 0.03 \text{ mm}^{-1}$.

E. Total Hemoglobin Validation

The final experimental homogeneous data set involved varying the total hemoglobin while keeping oxygen saturation, water, and scatter parameters constant. This was accomplished by use of a similar liquid phantom, with 1% Intralipid in saline, and by variation of the concentration of whole blood. The hematocrit level was measured by a clinical co-oximeter, yielding 1% blood, which is equivalent to 22- μM total hemoglobin. The blood concentration was varied from 0.2% to 1% in increments of 0.2%, and the amplitude and phase

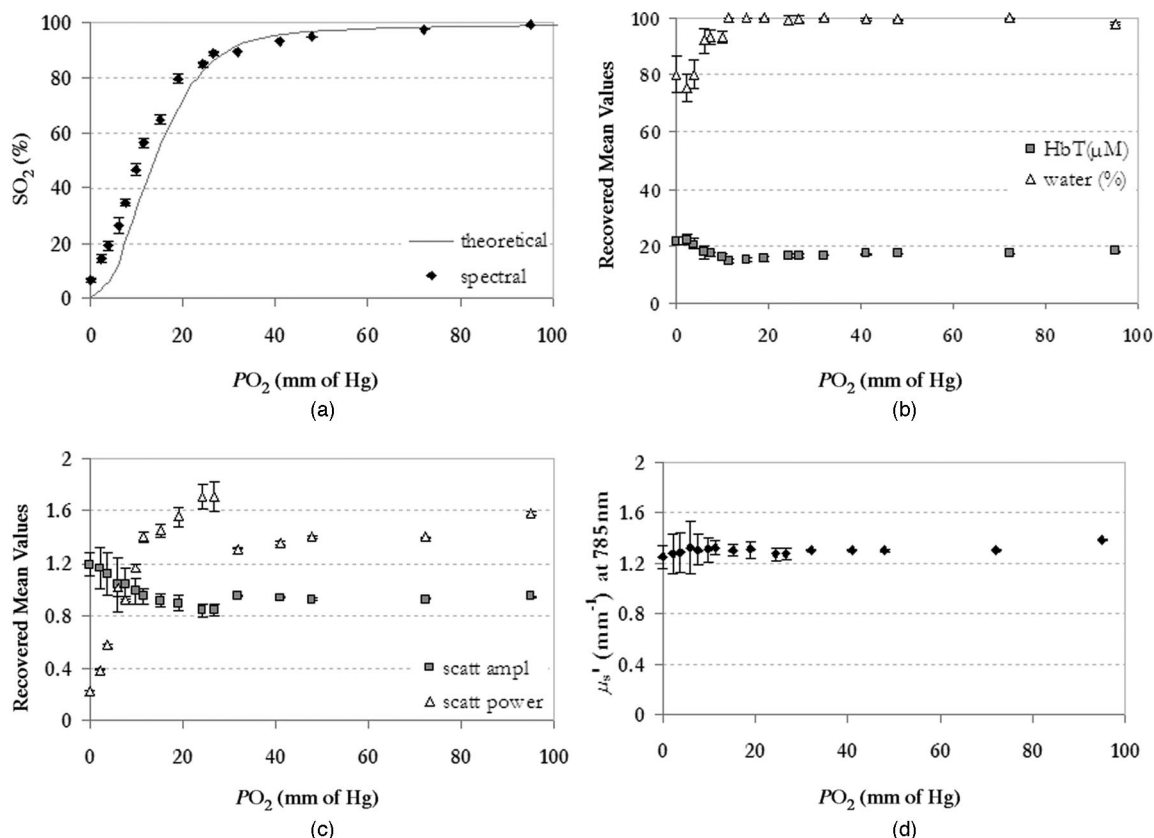


Fig. 4. Estimated mean values are shown from homogeneous reconstructions of a phantom with varying oxygen partial pressure (PO_2) of the solution induced by addition of yeast. The oxygen saturation is shown in (a), along with the theoretical estimate from the Hill curve. The total hemoglobin and percent water are shown in (b) with the theoretically estimated values of 18 mM and 100%, respectively, and should not vary with changes in oxygenation. The scatter power and amplitude are shown in (c) and should not vary. The reduced scattering coefficient at 785 nm is also shown in (d).

measurements were obtained for each level. After calibration, the spectrally constrained reconstruction was applied to the data, and the recovered mean and standard deviation from the NIR parameters are plotted in Fig. 5. The theoretical water and oxygen saturation values were 100%, as the phantom was a liquid oxygenated solution.

Figure 5(a) shows that the total hemoglobin followed the variation in blood (%) linearly and is quantitatively accurate, with a mean percent error of 6.2%. Oxygen saturation stayed constant with change in blood concentration [Fig. 5(b)], with a mean value of $98.9 \pm 0.6\%$. The same trend was found in water, with a mean value of $98.2 \pm 1.5\%$. The scatter amplitude and scatter power, shown in Fig. 5(b), are also independent of the variation in blood concentration, with a scatter amplitude of 0.65 ± 0.01 . The scatter power had a mean value of 1.39 ± 0.08 , and this agreed well with the estimated 1.4 derived from van Staveren *et al.*¹⁹ The reconstruction converged in 4–6 iterations for the different concentrations, and no spatial filtering was applied in the reconstruction.

4. Discussion and Conclusions

The spectrally constrained direct chromophore and scattering reconstruction has been implemented and

validated by use of simulated and experimental frequency-domain measurements. The results from Subsection 3.A show improved robustness of the reconstruction to increased amounts of noise in the data. The frequency-domain instrumentation in use typically has 0.5% noise in amplitude and 0.5 deg in phase,¹¹ and at this noise level. With simulated data from a homogeneous phantom, water images show a reduction in standard deviation from 32% to 10% (as percent of the mean) in going from the conventional to the spectral approach. Even at a 5% noise level, the spectral approach shows recovery of the parameters that is accurate within 10%, on average, with a significantly reduced standard deviation as compared with the conventional method. This insensitivity to noise is due to the use of multiwavelength data together with the spectral constraints, which results in a reduction in the number of unknowns, making the reconstruction problem less ill posed. The reduction in noise in the images is also observed in the homogeneous experimental data and is especially significant in water and scatter power. The NIR parameter images in Fig. 2 show the suppression of the artifacts in the images, particularly in water and scatter power, that is similar to the trend observed in the simulated data.

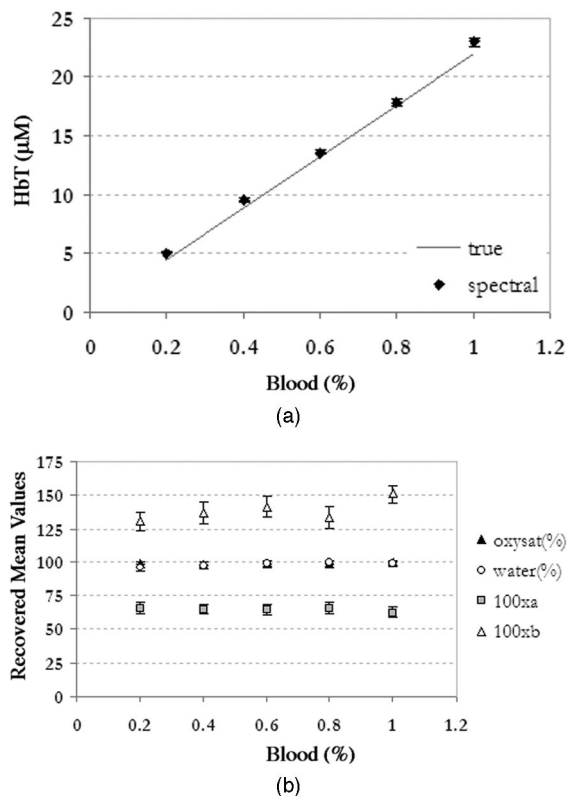


Fig. 5. Reconstructed mean and standard deviation values are shown from phantoms with varying concentrations of blood in which the total hemoglobin is graphed (a) alongside the theoretical value shown by a dotted line. The recovered values of oxygen saturation (%), water (%), scattering amplitude (a) and scattering power (b) are shown in (b), all of which are not expected to vary with changes in total blood (%). The scatter parameters are multiplied by 100 to allow them to be displayed on the same graph as the oxygen saturation and the water.

Water is an important measure of breast physiology; however, its quantitative accuracy from NIR tomography has yet to be validated. In the past several studies used a fixed water content in tissue (such as assuming 30%–31% fraction in tissue) to allow for spectral fitting of hemoglobin levels^{29,30} or used radiological data³¹ because sufficient wavelengths were unavailable and the cross talk between water and oxyhemoglobin prevented quantitatively accurate recovery of the water absorption. McBride *et al.*³² and Cerussi *et al.*³³ have shown that using sparse spectral image data from a subject with assumptions about the bulk concentration for water and lipids could have up to 15% influence on HbT and oxygen saturation estimates. In recent studies water has been shown to have significant variation with breast size in normal subject studies,²⁴ with values between subjects varying significantly from 10% to 70%. This large range was observed in a 30-subject population, as shown by Cerussi *et al.*,³³ and values of 21% to 82% were observed in a 26-subject population studied by Srinivasan *et al.*²⁴ These large numbers suggest that water is a measure of the extravascular space, since the vascular space is clearly less than 2% in most

breast tissues. Thus water yields different information about the physiology of the breast than does hemoglobin, and spatial changes are expected in water owing to different content in the fatty and glandular tissues, which varies with the composition of the breast. The change in water content during the course of the menstrual cycle has been followed by Cubeddu *et al.*, showing an increase in water in the second half of the cycle³⁴ for one patient. Shah *et al.*³⁵ have shown an increase of up to 28.1% in water in the luteal phase in a single volunteer, and Pogue *et al.*³⁶ have shown individual variations in seven subjects, with a mean value nearer to 2.5%. In a study following the effect of neoadjuvant chemotherapy³⁷ in a subject with a palpable adenocarcinoma, using optical white-light spectroscopy, water showed the most dramatic change, dropping 67% over the course of three treatment cycles. These studies have shown important trends in water content. However, to improve the clinical utility of the recovered values, it is important to show that they are quantitatively accurate estimates as well. The results shown here provide evidence of improvement in the quantification of water by use of the spectrally constrained approach compared with the conventional method of fitting for the chromophore and scattering parameters from optical property reconstructions. Water fraction values obtained by the new approach in data sets that follow variation in scattering, oxygen saturation, and total hemoglobin agree well with theoretical predictions and exhibit reduced noise and cross talk with oxyhemoglobin compared with the conventional technique.

Scattering is another area in which the constraints from Mie theory incorporated into the reconstruction significantly improve the quantification of the scatter amplitude and power. Recent studies have used scattering to study structural variations. For example, Poplack *et al.*³⁸ showed in a normal cohort of 23 women that there is a significant decrease in the reduced scattering coefficient (μ_s') at 785 nm with increasing body mass index and that adipose tissue was less scattering than glandular tissue, as expected. The same trend was observed by Durduran *et al.*²⁹ in a subject pool of 52 volunteers. Cerussi *et al.*³³ used the fit of μ_s' to the Mie theory approximation to show that scatter power decreases with increasing body mass index in a group of 30 healthy women. Pogue *et al.*³⁶ showed that scattering power and scatter amplitude could successfully separate categories of fatty and scattered breasts from extremely dense breasts ($p < 10^{-4}$) in a survey of 39 women with normal mammography. Since the risk of cancer is strongly correlated to the breast density,³⁹ this separation of breast densities in a noninvasive manner could prove very useful. Although these trends may prove to be promising in the future, their quantitative accuracy must be validated in phantom studies. Hence it is important to investigate the accuracy and standard deviation in these parameters to fully exploit the NIR information. Results in Subsection 3.A show the improved reconstruction of scatter power

images with robustness maintained at noise levels as high as 5% noise. In Fig. 2 the recovered mean for the scatter amplitude and scatter power agree well with predicted values from van Steveran *et al.*¹⁹ for homogeneous experimental data (containing 1% blood and 1% Intralipid in saline). A change in scattering, obtained by varying the Intralipid concentration in a homogeneous phantom solution, was successfully followed (Fig. 3), in which the scatter amplitude varied linearly and the scatter power showed a mean of 1.4 ± 0.1 during the changes in concentration. The cross talk between scatter parameters and chromophore concentrations is minimal, with total hemoglobin, oxygen saturation, and water content staying constant through this change [Figs. 3(c) and 3(d)], except at the highest scattering concentration of Intralipid (1.5%). The mean of μ_s' also exhibits a linear increase, and μ_s' at 785 nm doubles as the Intralipid concentration changes from 0.75% ($\mu_s' = 0.89 \text{ mm}^{-1}$) to 1.5% ($\mu_s' = 1.7 \text{ mm}^{-1}$), shown in Fig. 3(b).

The Hill curve relation between oxygen saturation (SO_2) and PO_2 of oxygen was followed by the spectral method in the graphs of Fig. 4, which showed that SO_2 was accurate, with a mean error of 7.7%. Total hemoglobin estimates remained constant through this change in PO_2 , producing a mean that is accurate to 97% of the expected value. Water content also showed this trend, with a mean of 94.2%, which compared well with the predicted value of 100%. Although some variation was found in the scatter amplitude and scatter power, μ_s' at 785 nm remained constant with change in oxygenation, with a mean of $1.3 \pm 0.03 \text{ mm}^{-1}$. The standard deviations in the oxygen saturation images remain low, even at lower oxygenation. This translates into a successful recovery of SO_2 in malignancies without significant noise or cross talk between scatter parameters and deoxy-hemoglobin. Total hemoglobin recovered by the spectral approach was separately validated by use of experimental data obtained by varying blood concentration from 0.2% to 1%. Quantitatively accurate results with a mean percent error of 6.2% were obtained. No cross talk between any of the parameters was observed during this variation, as shown in Fig. 5(b) in which oxygen saturation, water, scatter amplitude, and scatter power remained unchanged and close to predicted values.

The spectrally constrained approach is inherently robust owing to the addition of a *a priori* spectral behavior. It requires less spatial filtering, whereas the conventional technique benefits from a mean filter to prevent excessive noise in the images. This new approach also converges faster and is readily extendable to three-dimensional models as well. Use of data at additional wavelengths can easily be implemented without much computational burden in the inversion process. A partial volume-type reconstruction may be an efficient means of processing a large number of measurements. There is certainly some cross talk found at PO_2 values of oxygen lower than 11-mm Hg

or under extremely high scattering conditions, which can probably be resolved only by the addition of more wavelengths. Preliminary simulations have shown this to be true. The improved quantification of and robustness to noise of the reconstruction shown here for homogeneous measurements is currently also apparent in the heterogeneous data.

As the use of NIR tomography expands, spectrally constrained reconstruction should add considerable value to obtaining quantitatively accurate estimates of different parameters, particularly water and scatter power. The use of frequency-domain measurements allows a good separation of chromophore and scattering, and together with the spectral approach, we obtain reduced cross talk between the parameters, suppression of image artifacts, insensitivity to noise in the measurements, and, finally, accurate quantification of the NIR parameters.

This study was supported through National Institutes of Health grants PO1CA80139 and RO1CA69544 and through the Department of Defense grant DAMD17-03-01-0405.

References

1. B. W. Pogue, S. P. Poplack, T. O. McBride, W. A. Wells, O. K. S. Osterman, U. L. Osterberg, and K. D. Paulsen, "Quantitative hemoglobin tomography with diffuse near-infrared spectroscopy: pilot results in the breast," *Radiology* **218**, 261–266 (2001).
2. B. J. Tromberg, N. Shah, R. Lanning, A. Cerussi, J. Espinoza, T. Pham, L. Svaasand, and J. Butler, "Non-invasive *in vivo* characterization of breast tumors using photon migration spectroscopy," *Neoplasia* (New York) **2**, 26–40 (2000).
3. D. Grosenick, H. Wabnitz, K. T. Moesta, J. Mucke, M. Moller, C. Stroszczynski, J. Stossel, B. Wassermann, P. M. Schlag, and H. Rinneberg, "Concentration and oxygen saturation of hemoglobin of 50 breast tumors determined by time-domain optical mammography," *Phys. Med. Biol.* **49**, 1165–1181 (2004).
4. A. Corlu, T. Durduran, R. Choe, M. Schweiger, E. M. Hillman, S. R. Arridge, and A. G. Yodh, "Uniqueness and wavelength optimization in continuous-wave multispectral diffuse optical tomography," *Opt. Lett.* **28**, 2339–2341 (2003).
5. A. Li, Q. Zhang, J. P. Culver, E. L. Miller, and D. A. Boas, "Reconstructing chromophore concentration images directly by continuous-wave diffuse optical tomography," *Opt. Lett.* **29**, 256–258 (2004).
6. S. R. Arridge and M. Schweiger, "Image reconstruction in optical tomography," *Philos. Trans. R. Soc. London Ser. B* **352**, 717–726 (1997).
7. K. D. Paulsen and H. Jiang, "Spatially varying optical property reconstruction using a finite element diffusion equation approximation," *Med. Phys.* **22**, 691–701 (1995).
8. M. S. Patterson, B. C. Wilson, and D. R. Wyman, "The propagation of optical radiation in tissue I. Models of radiation transport and their application," *Lasers Med. Sci.* **6**, 155–168 (1990).
9. B. Brandstatter, K. Hollaus, H. Hutten, M. Mayer, R. Merwa, and H. Scharfetter, "Direct estimation of Cole parameters in multifrequency EIT using a regularized Gauss–Newton method," *Physiol. Meas.* **24**, 437–448 (2003).
10. Q. Fang, P. M. Meaney, S. D. Geimer, A. V. Streltsov, and K. D. Paulsen, "Microwave image reconstruction from 3-D fields coupled to 2-D parameter estimation," *IEEE Trans. Med. Imaging* **23**, 475–484 (2004).
11. T. O. McBride, B. W. Pogue, S. Jiang, U. L. Osterberg, and K. D. Paulsen, "A parallel-detection frequency-domain near-

- infrared tomography system for hemoglobin imaging of the breast *in vivo*," *Rev. Sci. Instrum.* **72**, 1817–1824 (2001).
12. T. O. McBride, B. W. Pogue, U. L. Osterberg, and K. D. Paulsen, "Strategies for absolute calibration of near infrared tomographic tissue imaging," in *Oxygen Transport to Tissue XXI*, J. F. Dunn and H. M. Swartz, eds., (Pabst, Lengerich, Germany, 2001).
13. A. Ishimaru, *Wave Propagation and Scattering in Random Media*, Vol. 1 (Academic, New York, 1978).
14. H. Jiang, K. D. Paulsen, U. L. Osterberg, B. W. Pogue, and M. S. Patterson, "Optical image reconstruction using frequency-domain data: simulations and experiments," *J. Opt. Soc. Am. A* **13**, 253–266 (1996).
15. H. Dehghani, B. W. Pogue, J. Shudong, B. Brooksby, and K. D. Paulsen, "Three-dimensional optical-tomography: resolution in small-object imaging," *Appl. Opt.* **42**, 3117–3128 (2003).
16. D. W. Marquardt, "An algorithm for least squares estimation of nonlinear parameters," *J. Soc. Ind. Appl. Math.* **11**, 431–441 (1963).
17. W. H. Press, S. A. Teukolsky, W. J. Vetterling, and B. P. Flannery, *Numerical Recipes in Fortran: the Art of Scientific Computing*, 2nd ed. (Cambridge U. Press, Cambridge, UK, 1986).
18. T. O. McBride, B. W. Pogue, E. Gerety, S. Poplack, U. L. Osterberg, and K. D. Paulsen, "Spectroscopic diffuse optical tomography for quantitatively assessing hemoglobin concentration and oxygenation in tissue," *Appl. Opt.* **38**, 5480–5490 (1999).
19. H. J. van Staveren, C. J. M. Moes, J. van Marle, S. A. Prahl, and J. C. van Gemert, "Light scattering in Intralipid-10% in the wavelength range of 400–1100 nm," *Appl. Opt.* **30**, 4507–4514 (1991).
20. J. R. Mourant, T. Fuselier, J. Boyer, T. M. Johnson, and I. J. Bigio, "Predictions and measurements of scattering and absorption over broad wavelength ranges in tissue phantoms," *Appl. Opt.* **36**, 949–957 (1997).
21. J. M. Steinke and A. P. Shepherd, "Comparison of Mie theory and the light scattering of red blood cells," *Appl. Opt.* **27**, 4027–4033 (1988).
22. B. Beauvoit, H. Liu, K. Kang, P. D. Kaplan, M. Miwa, and B. Chance, "Characterization of absorption and scattering properties for various yeast strains by time-resolved spectroscopy," *Cell Biophys.* **23**, 91–109 (1993).
23. K. D. Paulsen, P. M. Meaney, M. J. Moskowitz, and J. M. Sullivan, "A dual mesh scheme for finite element based reconstruction algorithms," *IEEE Trans. Med. Imaging* **14**, 504–514 (1995).
24. S. Srinivasan, B. W. Pogue, S. Jiang, H. Dehghani, C. Kogel, S. Soho, J. J. Gibson, T. D. Tosteson, S. P. Poplack, and K. D. Paulsen, "Interpreting hemoglobin and water concentration, oxygen saturation and scattering measured *in vivo* by near-infrared breast tomography," *Proc. Natl. Acad. Sci. USA* **100**, 12349–12354 (2003).
25. X. Song, B. W. Pogue, T. D. Tosteson, T. O. McBride, S. Jiang, and K. D. Paulsen, "Statistical analysis of nonlinearly reconstructed near-infrared tomographic images: Part II—Experimental interpretation," *IEEE Trans. Med. Imaging* **21**, 764–772 (2002).
26. P. Vaupel, F. Kallinowski, and P. Okunieff, "Blood flow, oxygen and nutrient supply, and metabolic microenvironment of human tumors: a review," *Cancer Res.* **49**, 6449–6465 (1989).
27. S. Srinivasan, B. W. Pogue, S. Jiang, H. Dehghani, and K. D. Paulsen, "Validation of hemoglobin and water molar absorption spectra in near-infrared diffuse optical tomography," in *Optical Tomography and Spectroscopy of Tissue V*, B. Chance, R. R. Alfano, B. J. Tromberg, M. Tamura, and E. M. Sevick-Muraca, eds., *Proc. SPIE* **4955**, 407–415 (2003).
28. N. Varjavand, "The interactive oxyhemoglobin dissociation curve," <http://www.ventworld.com/resources/oxydisso/dissohtml.2002>.
29. T. Durduran, R. Choe, J. P. Culver, L. Zubkov, M. J. Holboke, J. Giammarco, B. Chance, and A. G. Yodh, "Bulk optical properties of healthy female breast tissue," *Phys. Med. Biol.* **47**, 2847–2861 (2002).
30. D. Grosenick, K. T. Moesta, H. Wabnitz, J. Mucke, C. Stroszczynski, R. Macdonald, P. M. Schlag, and H. Rinneberg, "Time-domain optical mammography: initial clinical results on detection and characterization of breast tumors," *Appl. Opt.* **42**, 3170–3186 (2003).
31. D. R. White and H. Q. Woodard, "Average soft-tissue and bone models for use in radiation dosimetry," *Br. J. Radiol.* **60**, 907–913 (1987).
32. T. O. McBride, B. W. Pogue, S. Jiang, U. L. Osterberg, K. D. Paulsen, and S. P. Poplack, "Multi-spectral near-infrared tomography: a case study in compensating for water and lipid content in hemoglobin imaging of the breast," *J. Biomed. Opt.* **7**, 72–79 (2002).
33. A. Cerussi, D. Jakubowski, N. Shah, F. Bevilacqua, R. Lanning, A. J. Berger, D. Hsiang, J. Butler, R. F. Holcombe, and B. J. Tromberg, "Spectroscopy enhances the information content of optical mammography," *J. Biomed. Opt.* **7**, 60–71 (2002).
34. R. Cubeddu, C. D'Andrea, A. Pifferi, P. Taroni, A. Torricelli, and G. Valentini, "Effects of the menstrual cycle on the red and near-infrared optical properties of the human breast," *Photochem. Photobiol.* **72**, 383–391 (2000).
35. N. Shah, A. Cerussi, C. Eker, J. Espinoza, J. Butler, J. Fishkin, R. Hornung, and B. Tromberg, "Noninvasive functional optical spectroscopy of human breast tissue," *Proc. Natl. Acad. Sci. USA* **98**, 4420–4425 (2001).
36. B. W. Pogue, S. Jiang, H. Dehghani, C. Kogel, S. Soho, S. Srinivasan, X. Song, S. P. Poplack, and K. D. Paulsen, "Characterization of hemoglobin, water and NIR scattering in breast tissue: analysis of inter-subject variability and menstrual cycle changes relative to lesions," *J. Biomed. Opt.* **9**, 541–552 (2004).
37. D. B. Jakubowski, A. E. Cerussi, F. Bevilacqua, N. Shah, D. Hsiang, J. Butler, and B. J. Tromberg, "Monitoring neoadjuvant chemotherapy in breast cancer using quantitative diffuse optical spectroscopy: a case study," *J. Biomed. Opt.* **9**, 230–238 (2004).
38. S. P. Poplack, K. D. Paulsen, A. Hartov, P. M. Meaney, B. W. Pogue, T. D. Tosteson, M. R. Grove, S. K. Soho, and W. A. Wells, "Electromagnetic breast imaging: average tissue property values in women with negative clinical findings," *Radiology* **231**, 571–580 (2004).
39. M. T. Mandelson, N. Oestreicher, P. L. Porter, D. White, C. A. Finder, S. H. Taplin, and E. White, "Breast density as a predictor of mammographic detection: comparison of interval- and screen-detected cancers," *J. Natl. Cancer Inst.* **92**, 1081–1087 (2000).